

# **Investigation of the Influence of Initial Condition on the Spatial Development of Plane Jets Using Direct Numerical Simulation**

Nannan WU

Graduate School of Engineering

Nagoya University

Thesis for Doctor of Philosophy in Engineering

Supervisors: Professor Yasuhiko Sakai

Assoc. Professor Kouji Nagata





NAGOYA  
UNIVERSITY

INVESTIGATION OF THE INFLUENCE OF INITIAL  
CONDITION ON THE SPATIAL DEVELOPMENT OF  
PLANE JETS USING DIRECT NUMERICAL  
SIMULATION

BY

NANNAN WU

A THESIS SUBMITTED IN FULFILLMENT OF THE REQUIREMENTS FOR

THE DEGREE OF DOCTOR OF PHILOSOPHY

IN

ENGINEERING

AT

GRADUATE SCHOOL OF ENGINEERING

NAGOYA UNIVERSITY

FURO-CHO, CHIKUSA-KU, NAGOYA, 464-8603, JAPAN

JULY 2014





# Contents

<b>List of Figures</b> .....	i
<b>Acknowledgement</b> .....	v
<b>Chapter 1 Introduction</b> .....	1
1.1 Research Background .....	1
1.2 Characteristics of Plane Jet .....	4
1.2.1 Some Observations on Flow Evolution .....	4
1.2.2 Equations of Motion for Mean flow .....	6
1.3 Engineering Application (Air Curtain) .....	8
1.4 Definition of Initial Condition .....	9
1.4.1 Exit Reynolds Number .....	9
1.4.2 Exit Velocity Profile .....	11
1.5 Motivation for Present Study .....	12
1.6 Study Objectives .....	13
1.7 Thesis Outline .....	13
References .....	14
<b>Chapter 2 DNS of Plane Jet</b> .....	17
2.1 Introduction to Numerical Simulation of Plane Jet .....	17
2.2 Governing Equations and Non-dimensionalization .....	19
2.2.1 Non-dimensionalization of Governing Equations .....	19
2.2.2 Governing Equations .....	20
2.3 Discretization of Governing Equations .....	21
2.3.1 Temporal Discretization .....	21
2.3.2 Spatial Discretization .....	23
2.4 Finite difference schemes in staggered grid systems .....	25
2.4.1 Staggered Grid System .....	25
2.4.2 Fully Conservative Fourth Order Finite Difference Scheme in a Staggered Grid System .....	26
2.5 Solution of Poisson Equation .....	27

## Contents

---

2.6 Schematic of Computational Domain .....	29
2.7 Initial and Boundary Conditions .....	29
2.7.1 Initial Condition .....	29
2.7.2 Boundary Condition .....	31
References.....	32
<b>Chapter 3 Influence of Exit Reynolds Number .....</b>	<b>34</b>
3.1 Introduction .....	34
3.2 Instantaneous Results .....	35
3.2.1 Velocity and Pressure .....	35
3.2.2 Scalar and Its Gradient .....	37
3.3 Statistical Results.....	40
3.3.1 Statistics along Jet Centerline.....	40
3.3.2 Lateral Evolution of Plane Jet .....	42
3.4 Conclusion.....	52
References.....	52
<b>Chapter 4 Influence of Mean Exit Velocity Profile and Cross-impact between Different Initial Factors .....</b>	<b>54</b>
4.1 Introduction .....	54
4.2 Mean Exit Profiles at Jet Exit.....	56
4.3 Instantaneous Results .....	58
4.3.1 Velocity and Pressure .....	58
4.3.2 Scalar and Its Gradient .....	60
4.4 Statistical Results.....	62
4.4.1 Statistics along Jet Centerline.....	62
4.4.2 Lateral Evolution of Plane Jet .....	67
4.5 Conclusion.....	74
References.....	74
<b>Chapter 5 Visualization and Study on Coherent Structure and Turbulent/Non-turbulent Interface .....</b>	<b>77</b>
5.1 Introduction to Coherent Structure in Turbulence .....	77
5.2 Coherent Structure in Plane Jet .....	78
5.3 Influence of Initial Condition on Coherent Structure .....	82
5.4 Introduction to Turbulent/Non-turbulent Interface .....	84

## Contents

---

5.5 Turbulent/Non-turbulent Interface in Plane Jet.....	85
5.6 Influence of Initial Condition on Turbulent/Non-turbulent Interface .....	86
5.7 Conclusion .....	89
References .....	90
<b>Chapter 6 Invariants of Velocity-gradient, Rate-of-strain, and Rate-of-rotation</b>	
<b>Tensors.....</b>	<b>93</b>
6.1 Introduction.....	93
6.2 Definition and Physical Meaning.....	94
6.3 Results and Discussion.....	96
6.3.1 Joint Pdfs of the Velocity Gradient Tensor Invariants .....	96
6.3.2 Velocity Gradient Tensor Invariants along the Jet Centerline.....	105
6.4 Conclusion .....	108
References .....	108
<b>Chapter 7 Conclusions and Future Prospect .....</b>	<b>110</b>
7.1 Conclusions.....	110
7.2 Future Prospect .....	112



## List of Figures

Figure 1.1 Sketch of free turbulent plane jet-----	4
Figure 1.2 Self-similarity of turbulent plane jet. (a) Mean streamwise velocity profile; (b) dimensionless mean streamwise velocity profile.-----	6
Figure 1.3 Schematic of air curtain-----	9
Figure 2.1 Temporal discretization scheme in computation of instantaneous velocity-----	22
Figure 2.2 Staggered grid system and storage of variables-----	25
Figure 2.3 Schematic of computational domain-----	29
Figure 2.4 Mean streamwise velocity profiles at the jet exit-----	30
Figure 3.1 Instantaneous streamwise velocity (Left) and pressure (Right) fields-----	36
Figure 3.2 Instantaneous scalar field-----	38
Figure 3.3 Instantaneous scalar gradient magnitude field-----	39
Figure 3.4 Evolution of mean variables along the jet centerline. (Left) Mean streamwise velocity, where the experimental data is from Deo et al.[10]; (Right) mean scalar.----	41
Figure 3.5 Evolution of turbulent variables along the jet centerline. (a) Turbulent streamwise velocity, where the experimental data is from Deo et al. [10]; (b) turbulent lateral velocity; (c) turbulent spanwise velocity; (d) turbulent scalar.-----	42
Figure 3.6 Lateral profiles of mean and turbulent streamwise velocities. (Left) The case with $Re = 2,000$ ; (Right) the case with $Re = 3,000$ .-----	43
Figure 3.7 Lateral profiles of mean and turbulent scalars. (Left) The case with $Re = 2,000$ ; (Right) the case with $Re = 3,000$ .-----	44
Figure 3.8 Lateral profile of variables at $x/d = 15.0$ . (a) Mean streamwise velocity; (b) turbulent streamwise velocity; (c) mean scalar; (d) turbulent scalar.-----	45
Figure 3.9 Lateral profile of variables at $x/d = 35.0$ . (a) Mean streamwise velocity; (b) turbulent streamwise velocity; (c) mean scalar; (d) turbulent scalar.-----	46
Figure 3.10 Lateral profile of variables at $x/d = 15.0$ . (a) Reynolds stress; (b) streamwise turbulent scalar flux; (c) lateral turbulent scalar flux.-----	47
Figure 3.11 Lateral profile of variables at $x/d = 35.0$ . (a) Reynolds stress; (b) streamwise turbulent scalar flux; (c) lateral turbulent scalar flux.-----	48
Figure 3.12 Lateral profile of the mean streamwise momentum transport at $x/d = 15.0$ . (a) Streamwise convection term; (b) lateral convection term; (c) lateral	

turbulent transport term; (d) streamwise turbulent transport term.-----	49
Figure 3.13 Lateral profile of the mean streamwise momentum transport at $x/d = 35.0$ . (a) Streamwise convection term; (b) lateral convection term; (c) lateral turbulent transport term; (d) streamwise turbulent transport term.-----	50
Figure 3.14 Lateral profile of the mean scalar transport at $x/d = 15.0$ . (a) Streamwise convection term; (b) lateral convection term; (c) lateral turbulent transport term; (d) streamwise turbulent transport term.-----	51
Figure 4.1 Mean streamwise velocity profiles at the jet exit-----	56
Figure 4.2 Mean streamwise velocity gradient at the jet exit -----	56
Figure 4.3a Instantaneous streamwise velocity (Left) and pressure (Right) fields at $Re = 1,000$ -----	57
Figure 4.3b Instantaneous streamwise velocity (Left) and pressure (Right) fields at $Re = 3,000$ -----	58
Figure 4.4 Instantaneous scalar field-----	59
Figure 4.5a Instantaneous scalar gradient magnitude field at $Re = 1,000$ -----	60
Figure 4.5b Instantaneous scalar gradient magnitude field at $Re = 3,000$ -----	61
Figure 4.6 Mean streamwise velocity profiles along the jet centerline-----	62
Figure 4.7 Decay rate of mean streamwise velocity along the jet centerline-----	63
Figure 4.8 Turbulent streamwise velocity profiles along the jet centerline-----	63
Figure 4.9 Mean scalar profiles along the jet centerline-----	64
Figure 4.10 Decay rate of mean scalar along the jet centerline-----	64
Figure 4.11 Turbulent scalar profiles along the jet centerline-----	65
Figure 4.12 Evolution of local $Re$ along the jet centerline-----	65
Figure 4.13 Lateral profiles of mean and turbulent streamwise velocities with $Re = 2,000$ . (Left) The case with TH; (Right) the case with PA.-----	66
Figure 4.14 Lateral profiles of mean and turbulent streamwise velocities with $Re = 3,000$ . (Left) The case with TH; (Right) the case with PA.-----	67
Figure 4.15 Lateral profile of variables at $x/d = 15.0$ . (a) Mean streamwise velocity; (b) turbulent streamwise velocity; (c) mean scalar; (d) turbulent scalar.-----	68
Figure 4.16 Lateral profile of variables at $x/d = 35.0$ . (a) Mean streamwise velocity; (b) turbulent streamwise velocity; (c) mean scalar; (d) turbulent scalar.-----	69
Figure 4.17 Lateral profile of variables at $x/d = 15.0$ . (a) Reynolds stress; (b) streamwise turbulent scalar flux; (c) lateral turbulent scalar flux.-----	70
Figure 4.18 Lateral profile of variables at $x/d = 15.0$ in the case of $Re = 1,000$ (PA) based on 30,000 samples-----	71
Figure 4.19 Lateral profile of variables at $x/d = 35.0$ . (a) Reynolds stress; (b) streamwise turbulent scalar flux; (c) lateral turbulent scalar flux.-----	71

Figure 4.20 Lateral profile of the mean streamwise momentum transport at $x/d = 15.0$ . (a) Streamwise convection term; (b) lateral convection term; (c) lateral turbulent transport term; (d) streamwise turbulent transport term.-----	72
Figure 4.21 Lateral profile of the mean scalar transport at $x/d = 15.0$ . (a) Streamwise convection term; (b) lateral convection term; (c) lateral turbulent transport term; (d) streamwise turbulent transport term.-----	73
Figure 5.1 CS in the plane jet based on the isosurfaces of pressure-----	79
Figure 5.2 CS in the plane jet based on the isosurfaces of second invariant of velocity gradient tensor-----	80
Figure 5.3 CS in the plane jet. Green structures show the isosurfaces of $p'$ ; grey structures show the isosurfaces of $Q'$ -----	81
Figure 5.4 CS in plane jets with different exit Re-----	82
Figure 5.5 CS in plane jets with parabola exit mean velocity profile-----	83
Figure 5.6 T/NT interface with $Re = 2,000$ (TH). (Top) Top view; (Bottom) side view.-	85
Figure 5.7 Top view of T/NT interface-----	87
Figure 5.8 Side view of T/NT interface with different exit Re-----	88
Figure 5.9 Side view of T/NT interface with parabola exit mean velocity profile-----	89
Figure 6.1 Sketch of the invariant map of $(Q_w, -Q_s)$ -----	97
Figure 6.2 Joint pdfs of $(Q_w, -Q_s)$ -----	98
Figure 6.3 Sketch of the invariant map of $(R, Q)$ -----	99
Figure 6.4 Joint pdfs of $(R, Q)$ -----	101
Figure 6.5 Sketch of the invariant map of $(R_s, Q_s)$ -----	103
Figure 6.6 Joint pdfs of $(R_s, Q_s)$ - (1)-----	104
Figure 6.7 Joint pdfs of $(R_s, Q_s)$ - (2)-----	105
Figure 6.8 Joint pdfs of $(R_s, Q_s)$ - (3)-----	105
Figure 6.9 Profile of $\langle Q_w \rangle$ along the jet centerline-----	106
Figure 6.10 Profile of $\langle -Q_s \rangle$ along the jet centerline-----	106
Figure 6.11 Profile of $\langle R \rangle$ along the jet centerline-----	107
Figure 6.12 Profile of $\langle R_s \rangle$ along the jet centerline-----	107





## Acknowledgement

I owe my deepest gratitude to my supervisors, Professor Yasuhiko Sakai and Associate Professor Kouji Nagata for their invaluable support, sincere encouragement and masterly guidance over the past three and a half years. Without their supervision and insight into scientific research, it won't be possible for me to perform my doctoral program successfully.

I would like to particularly thank Professor Hiroshi Yamashita and Professor Norihiko Yoshikawa for their time and effort to give me the precious suggestions on the study and help me to modify the thesis.

It is such an honor for me to have the opportunity of being a student of Professor Sakai and studying in Nagoya University. Almost four years ago, the invitation from Professor Sakai gave me the precise chance to continue my aspiration to turbulence research and the wonderful Japan. For my past time spent in Japan, his permanent help and instruction make my life and study enjoyable and enlightening. Words cannot even come close to express my thanks to Professor Sakai enough.

I am very lucky to have another wonderful and honorable supervisor, Associate Professor Nagata. I won't forget every bit of his help and suggestion to my study plan, confusion about research ideas, publications and so on.

I truly want to become that kind of person like my two supervisors with such incredible kindness and wisdom at some day.

My Ph.D. was supported by the China Scholarship Council (CSC). Hence, I would like to express my thanks to my country for supplying me an opportunity to scale my intellectual height by studying in Nagoya University.

My study was carried out under the Collaborative Research Project of the Institute of Fluid Science, Tohoku University and supported by Grants-in-Aid (Nos.

25289030, 25289031) from the Ministry of Education, Culture, Sports, Science and Technology in Japan. I also want to show my thanks to them. Another special thank is expressed to Professor Toshiyuki Hayase from Tohoku University, whose support makes my simulation successful by using the super computer.

I would never forget the help I got from Associate Professor Yasumasa Ito. His masterly guidance on how to write and make the proper presentation on the international conferences will be cherished in my future research and work. The discussion with him always enlightens me.

I would like to give my thanks to Dr. Hiroki Suzuki, Dr. Tomoaki Watanabe and Mr. Daisuke Sugimoto. Because of their previous study, my study can be started and carried out smoothly. And I would never forget the helps I got from Mr. Daisuke Sugimoto and Dr. Tomoaki Watanabe when they were my tutor, which solved so many difficulties in my life.

Sincere thanks also go to Mr. Osamu Terashima, whose work and help makes the every second of my study in the laboratory be infiltrated by happiness. I am still thankful to his picking up on the first day I arrived in Japan.

I also want to thank Mr. Koichi Hoshino, Mr. Kazuhiro Onishi, Mr. Hiroki Yasuhara, Mr. Tomoyuki Watanabe and other members, with whom I am studying or ever studied together in the statistical fluid engineering laboratory, department of mechanical engineering, graduate school of engineering, Nagoya University. I will not forget the life and study shared with them. Wish all of them well in the future.

I owe a lot to my supervisor in China University of Mining and Technology, Prof. Chuwen Guo. The experience of studying under his guidance taught me how to become a qualified researcher. Thanks to his support and suggestion, because of which, I have become today's better me.

I would like to thank my parents and grandma. They are the important reasons for me to keep studying and living in order to capture a bright future and beautiful life. I also give some credits to my little brother for the life with his accompanying,

## Acknowledgement

---

and want to tell him “please keep happy, like the sunshine and remind me we will support each other forever.”

It is lucky for me to have the precious friendships with Defan Cheng, Fei Zhang, Mengnan Fu, and Nan Yao. The memories with them cheered me up when I felt blue. I can’t wait to go back and reunite with these great persons.

I enjoyed the past almost four years spent in Japan, which was marked by each wonderful person I met and acquainted. I want to thank the god for cherishing me this way.

Nannan WU

July, 2014

In Nagoya, Japan



# Chapter 1

## INTRODUCTION

Plane jet is one kind of symmetrical jet flow and a statistically two-dimensional flow possessing a relatively simple geometry and easily-simulated boundary conditions, which make it attractive for fundamental research into the turbulent flow. Even though the direct applications of truly plane jet are limited at present, it is technologically concerned because of the utilization of broadly plane jet with interest in a wide variety of engineering applications containing combustion, propulsion, environmental flows, and so on. The study on the kinematical and dynamical properties of plane jet is important and necessary in view of both the scientific and engineering practice.

### 1.1 Research Background

The research associated with plane jet may be traced back to the 1930's, which began with the Schlichting's theoretically numerical study[1] and the integration of the theoretical, experimental and computational research methodologies has become the research foundation of the study of plane jet up to now. Over the past 80 years, with the modification and optimization of flow measurement technology (mainly hot wire anemometry, laser Doppler velocimetry and particle image velocimetry) and the advancement of the calculation capacity of scientific computer, our insights into plane jet have been profoundly furthered, especially its turbulent characteristics, based on both experiments and numerical simulations.

The first experimental work on plane jet was carried out by Forthman[2], who checked the Tollmien's calculation equation of Prandtl's mixing length and measured the mean velocity of a plane air wall jet, called as the partially open jet in his paper, covering the axial range 0 to 25 slot widths downstream. Afterwards, Miller and Comings[3] provided one more comprehensive study about the free plane jet, in which

root-mean-square (*rms*) turbulent velocity and static pressure distribution were measured in a longer axial distance up to the 40 slot widths. In the work of Knystautas[4], the self-similarity of plane jets was firstly revealed based on the mean velocity profiles by the study on the merging of a long line of identical jets in a still ambient fluid. Afterwards, the more thorough investigation was provided by Bradbury[5] and Heskestad[6], in Heskestad's study the characteristics of the centerline development of turbulent intensity with different flow speed at the jet exit were assessed, which unveiled the effects of exit Reynolds number on plane jet, and was the first attempt to study the plane jet with different initial conditions at the jet exit independently.

Inspired by the work of Bradbury[5], Gutmark and Wygnanski[7] found that the self-similarity of plane jet was achieved beyond 40 slot widths in their experiments, and they provided the comprehensive measurement results including mean velocities, turbulence intensities and third- and fourth-order terms, as well as two-point correlations and intermittency factor. The effects of the initial conditions, exit Reynolds number and exit geometrical parameters, on the evolution of the turbulent velocity field as well as the jet spreading rate and centerline velocity decay were observed in which some evidence showed the self-similarity of plane jet may not be universal but depends on the initial conditions. And the similar comprehensive investigations was also performed in the work of Jenkins and Goldschmidt[8], and Thomas and Goldschmidt[9] with the different initial conditions. On the basis of these studies, it is revealed that the asymptotic behavior for the mean and turbulence statistics was captured at the different streamwise location. George[10] proposed that the varying initial conditions at jet exit lead to differences in the downstream development of jet flow.

The initial interest of plane jet research was mainly focused in the downstream (self-similar) region since all jets will eventually approach this state and the theoretical nature of the flow becomes simpler. In the recent 14 years, Gordeyev and Thomas[11] experimentally examined the topology of the large-scale structure, e.g. the coherent structure, in the self-similar region of the turbulent plane jet by application of the proper orthogonal decomposition (POD), which indicated the self-similar large-scale structure in the plane jet consists of a dominant plane component including two lines

of large-scale spanwise vortices arranged approximately asymmetrically with respect to the jet centerline, resembling the classic Kármán vortex street. Atassi and Lueptow[12] supplied a model of flapping motion in the transition region of the plane jet based on the linear inviscid analysis near the jet exit and the nonlinear finite-amplitude analysis in the further downstream region from the exit, the work validated that the flapping of the jet could be attributed to a traveling wave instability which leads to a sequence of coherent structures alternating in sign (asymmetric) on either side of the jet. In 2007 and 2008, Deo et al. published four papers about their experimental work on the effects of initial conditions on the plane jet, including the exit Reynolds number from 1,500 to 16,500[13], the sidewalls[14], the nozzle aspect ratio[15], and the nozzle-exit geometric profile[16], which are the most systematic and comprehensive work on this topic up to now; however, the cross-impact between these factors were not considered or discussed in their work. Suresh et al.[17] launched the work on the transitional characteristics of the plane jet at varying exit Reynolds number from 250 to 6250, which showed the flow development is Reynolds number dependent, in contrast to the fully developed turbulent jets which show flow features are independent of initial conditions, but this result was not observed in the similar work of Deo et al.[13], who emphasized the differences in other initial factors between the experiments may be responsible for the deviation. Terashima et al.[18] developed a new technique for the simultaneous measurement of velocity and pressure, and the utilization in the plane jet showed the fine results, but the measurement errors still occurred, especially for the pressure fluctuation. Following the work of Gordeyev and Thomas[11], Shim et al.[19] investigated the large-scale coherent structure in the near field of a plane jet using both two-dimensional particle image velocimetry (PIV) measurements and POD techniques, in which the presence of anti-symmetrical vortices was confirmed. Sakakibara[20] carried out a plane jet excited by disturbances with spanwise phase variations, which was a new attempt to trigger the secondary instability at the plane jet exit. In this condition, the vortex pairing did not occur downstream and the rate at which the jet widened was reduced. In 2013, Deo et al.[21] made another publication about the similarity analysis of the momentum field of the plane air jet with varying jet-exit and local Reynolds numbers, which enriched their previous work.

In the turbulence studies based on the experimental method, the measurement errors are usually inevitable and some flow conditions are difficultly manipulated or realized, which inspired the usage of the numerical simulation method. In 1972, Orszag and Patterson performed a  $32^3$  computation of the homogenous isotropic turbulence[22], since their work, the Direct Numerical Simulation (DNS) has become an important branch of the methodology for turbulence study. To simulate the plane jet based on DNS was launched by the work of Comte et al.[23], who performed the temporal simulation of the fully developed region of a two-dimensional Bickley jet, in which the streamwise velocity profile is proportional to  $\text{sech}^2(y)$  and  $y$  is the transverse coordinate, to study the influence of initial perturbations, including the white-noise perturbation and the sine perturbation, which is the first trial of numerical simulation. Afterwards, Stanley and Sarkar[24][25], Klein et al.[26], da Silva et al.[27], and others carried out the DNS of the plane jet separately. With the utilization of DNS, it is allowed to evaluate and compare different computational models; meanwhile, some subjects, which are difficult to study experimentally, were observed, such as the fine-scale dynamics and the examination of flows in some idealized conditions.

## 1.2 Characteristics of Plane Jet

### 1.2.1 Some Observations on Flow Evolution

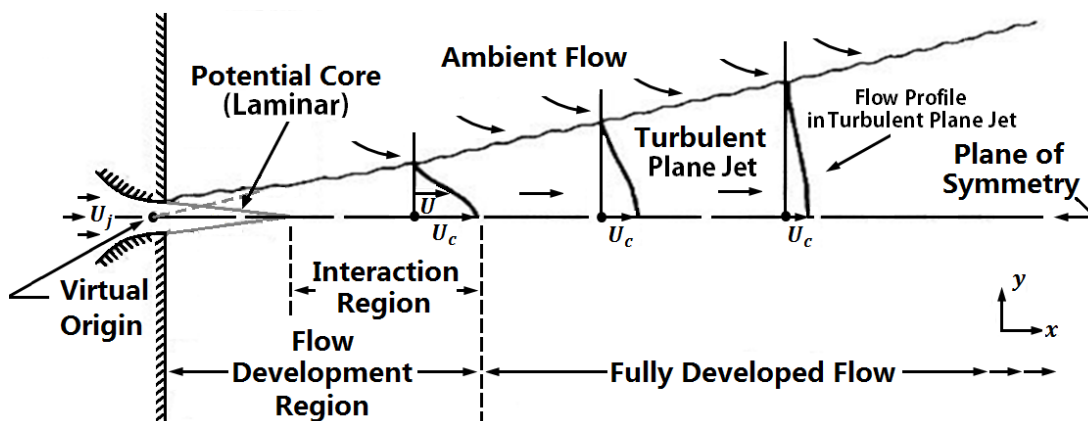


Figure 1.1 Sketch of free turbulent plane jet

Plane jet can be described as a statistically two-dimensional flow with a dominant mean motion in the streamwise direction ( $x$  direction), jet spread in the lateral



direction ( $y$  direction) and zero entrainment in the spanwise direction. Figure 1.1 is a schematic representation of the whole evolution process of free turbulent plane jet, which can be divided into two regions, the flow development (transition) region, also called the near field region, and the fully developed flow region, possessing the characteristics of the typical isotropic turbulent flow. In the flow development region, close to the jet exit, a wedge-like region, with undiminished mean streamwise velocity  $U_j$  and zero mean lateral velocity, is called the potential core, where flow is laminar, and it is surrounded by the mixing layer on top and bottom. The region between the potential core and the fully developed flow region is named the interaction region, in which the flow is characterized by the severe decay of mean flow and strong turbulence. In the fully developed flow region, plane jet is fully self-similar, which means that the flow is self-similar at all orders of the turbulence moments and at all scales of motion. The self-similarity in turbulence is the state characterized by the dissipation rate  $\epsilon \propto q^3/L$ , where  $q^2 \equiv u_i u_i$ ,  $u_i$  is the instantaneous velocity, and  $L$  is the integral length scale. In addition, it will be manifested in the approach of  $d\delta/dx$  to its asymptotic value, where  $\delta$  is the local width of flow. For turbulent plane jet, as the local turbulence Reynolds number is large enough, typically  $10^4$ , full self-similarity can be achieved.

The self-similarity of turbulent plane jet in the fully developed flow region is shown by Figure 1.2 based on the mean streamwise velocity profiles from the work of Förthmann[2], where  $x$  is the streamwise location apart from the jet exit,  $y$  is the lateral location apart from the jet centerline,  $U_c$  is the mean streamwise velocity ( $U$ ) on the jet centerline,  $b_u$  is the mean half jet width for velocity field. At every location,  $U$  decreases continuously from a maximum value  $U_c$  on the jet centerline to a zero value at some distance from the jet centerline and the mean velocity profile transits from a relatively flat profile to a curved profile, which is shown by Figure 1.2(a); After making  $U$  and  $y$  dimensionless by dividing them using  $U_c$  and  $b_u$  respectively, I plot  $U/U_c$  against  $y/b_u$  to get Figure 1.2(b), which shows the velocity distributions at different locations fall on one common curve when  $x$  is larger than some value. This manner is called as the flow self-similarity.

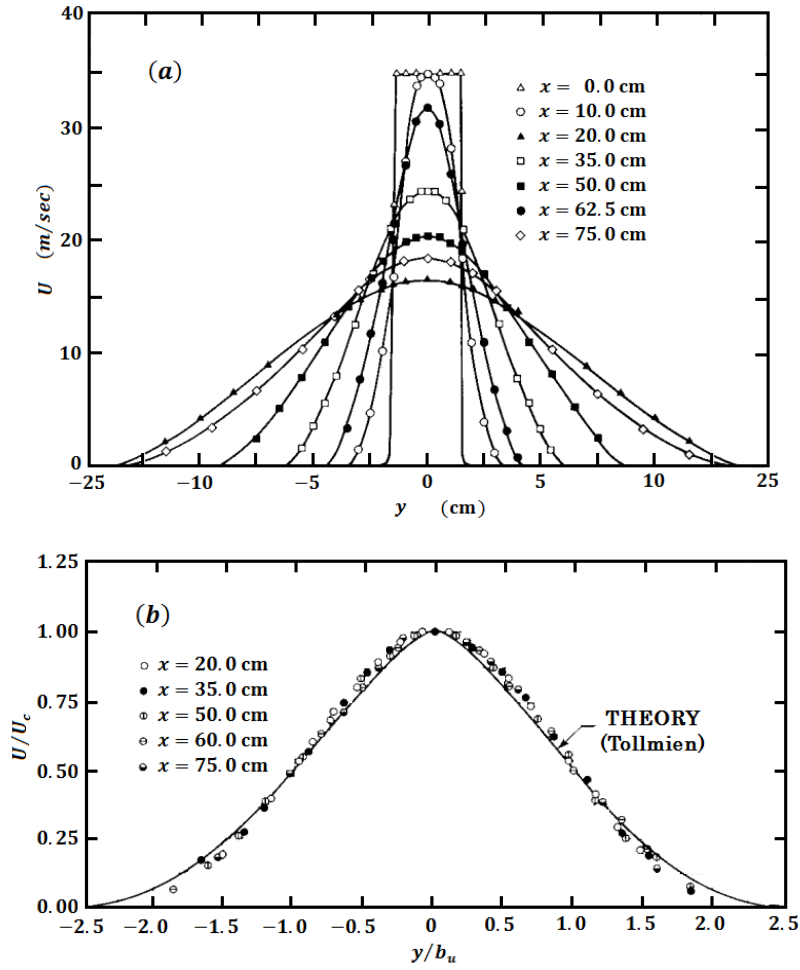


Figure 1.2 Self-similarity of turbulent plane jet[2]. (a) Mean streamwise velocity profile; (b) dimensionless mean streamwise velocity profile.

### 1.2.2 Equations of Motion for Mean flow[28]

The equations of motion for mean flow in free turbulent plane jet based on the Reynolds-averaged Navier–Stokes equations (or RANS equations) without the effects of body forces in the Cartesian system, which are written explicitly as:

$$\frac{\partial U}{\partial t} + U \frac{\partial U}{\partial x} + V \frac{\partial U}{\partial y} + W \frac{\partial U}{\partial z} = -\frac{1}{\rho} \frac{\partial P}{\partial x} + \nu \left( \frac{\partial^2 U}{\partial x^2} + \frac{\partial^2 U}{\partial y^2} + \frac{\partial^2 U}{\partial z^2} \right) - \left( \frac{\partial \langle u^2 \rangle}{\partial x} + \frac{\partial \langle uv \rangle}{\partial y} + \frac{\partial \langle uw \rangle}{\partial z} \right), \quad (1.1)$$

$$\frac{\partial V}{\partial t} + U \frac{\partial V}{\partial x} + V \frac{\partial V}{\partial y} + W \frac{\partial V}{\partial z} = -\frac{1}{\rho} \frac{\partial P}{\partial y} + \nu \left( \frac{\partial^2 V}{\partial x^2} + \frac{\partial^2 V}{\partial y^2} + \frac{\partial^2 V}{\partial z^2} \right)$$

$$-\left(\frac{\partial\langle uv\rangle}{\partial x} + \frac{\partial\langle v^2\rangle}{\partial y} + \frac{\partial\langle vw\rangle}{\partial z}\right), \quad (1.2)$$

$$\begin{aligned} \frac{\partial W}{\partial t} + U \frac{\partial W}{\partial x} + V \frac{\partial W}{\partial y} + W \frac{\partial W}{\partial z} = & -\frac{1}{\rho} \frac{\partial P}{\partial z} + \nu \left( \frac{\partial^2 W}{\partial x^2} + \frac{\partial^2 W}{\partial y^2} + \frac{\partial^2 W}{\partial z^2} \right) \\ & - \left( \frac{\partial\langle uw\rangle}{\partial x} + \frac{\partial\langle vw\rangle}{\partial y} + \frac{\partial\langle w^2\rangle}{\partial z} \right). \end{aligned} \quad (1.3)$$

And the continuity equation, which is written as:

$$\frac{\partial U}{\partial x} + \frac{\partial V}{\partial y} + \frac{\partial W}{\partial z} = 0, \quad (1.4)$$

where  $U$ ,  $V$  and  $W$  and  $u$ ,  $v$  and  $w$  are the mean and turbulent velocities in the  $x$ -,  $y$ - and  $z$ -coordinate directions,  $t$  is the time variable,  $\rho$  is the mass density of the fluid,  $P$  is the mean pressure and  $\nu$  is the kinematic viscosity.

Because the mean flow in free turbulent plane jet is two-dimensional, it manifests Equation (1.3) can be omitted and it is obvious that  $W = 0$ ,  $\partial/\partial z$  of any mean quantity is zero, and  $\langle uw\rangle$  and  $\langle vw\rangle$  are zero. The mean flow is steady, which leads to  $\partial U/\partial t = 0$  and  $\partial V/\partial t = 0$ . Moreover, based on some consideration for the physical features of this flow, which are that  $U$  is generally much larger than  $V$  in a large portion of the jet and the gradients of velocities and stress in the  $y$ -direction are much larger than the ones in the  $x$ -direction, the equations of motion for the mean flow can be modified to be

$$U \frac{\partial U}{\partial x} + V \frac{\partial U}{\partial y} = -\frac{1}{\rho} \frac{\partial P}{\partial x} + \nu \frac{\partial^2 U}{\partial y^2} - \frac{\partial\langle u^2\rangle}{\partial x} - \frac{\partial\langle uv\rangle}{\partial y}, \quad (1.5)$$

$$0 = -\frac{1}{\rho} \frac{\partial P}{\partial y} - \frac{\partial\langle v^2\rangle}{\partial y}, \quad (1.6)$$

$$\frac{\partial U}{\partial x} + \frac{\partial V}{\partial y} = 0. \quad (1.7)$$

Integrating Equation (1.6) with respect to  $y$  from  $y$  to the location outside the jet, it is obtained that

$$P = P_\infty - \rho\langle v^2\rangle, \quad (1.8)$$

where  $P_\infty$  is the mean pressure outside the jet.

Based on Equation (1.8), we can get  $\partial P/\partial x = dP_\infty/dx - \rho \partial \langle v^2 \rangle / \partial x$  and then substitute the  $\partial P/\partial x$  in Equation (1.5), the new equation is

$$U \frac{\partial U}{\partial x} + V \frac{\partial U}{\partial y} = -\frac{1}{\rho} \frac{dP_\infty}{dx} + \nu \frac{\partial^2 U}{\partial y^2} - \frac{\partial}{\partial x} (\langle u^2 \rangle - \langle v^2 \rangle) - \frac{\partial \langle uv \rangle}{\partial y}.$$

Considering the term  $\partial(\langle u^2 \rangle - \langle v^2 \rangle)/\partial x$  is smaller than the other terms especially in the fully developed flow region, the above equation can be gradually simplified to be

$$U \frac{\partial U}{\partial x} + V \frac{\partial U}{\partial y} = -\frac{1}{\rho} \frac{dP_\infty}{dx} + \nu \frac{\partial^2 U}{\partial y^2} - \frac{\partial \langle uv \rangle}{\partial y}.$$

The last two terms in the above equation can be rewritten as

$$\frac{1}{\rho} \frac{\partial}{\partial y} \left( \mu \frac{\partial U}{\partial y} \right) + \frac{1}{\rho} \frac{\partial}{\partial y} (-\rho \langle uv \rangle) = \frac{1}{\rho} \frac{\partial}{\partial y} (\tau_l + \tau_t),$$

where  $\tau_l$  and  $\tau_t$  are the laminar and turbulent shear stresses respectively and  $\mu$  is the dynamic viscosity. Moreover, in free turbulent flows, as the solid boundaries are absent, generally  $\tau_t$  is much larger than  $\tau_l$ , which allow us to further simplify the above equation to be

$$U \frac{\partial U}{\partial x} + V \frac{\partial U}{\partial y} = -\frac{1}{\rho} \frac{dP_\infty}{dx} + \frac{1}{\rho} \frac{\partial \tau_t}{\partial y}. \quad (1.9)$$

The basic equations of motion for the mean flow in free turbulent plane jet consists of Equations (1.7) and (1.9).

### 1.3 Engineering Application (Air Curtain)

The dynamic and kinetic features of plane jets are technologically important and concerned in a wide variety of engineering applications. In this section, we will have a look at the engineering application of the plane jet based on one device, i.e., air curtain, as shown in Figure 1.3.

Air curtain, also called air door, is a device used for separating two spaces from each other by a produced air flow, which is a plane jet. Air curtain can serve many purposes, some of which are to keep flying insects out by creating forceful turbulent jet (Flying insect control), to help keep outside air in order to reduce infiltration through the opening (Cold storage), and to avoid cold drafts by mixing in warm air

heated by the air curtain (Energy conservation). Considering these above roles that air curtain plays, the sufficient work of air curtain is obviously related to the characteristics of the produced plane jet in it and it is clear that the entrainment of ambient fluid, the momentum and scalar transport and mixing, and the flow structure in the process of the jet growth will decide the efficiency of air curtain.

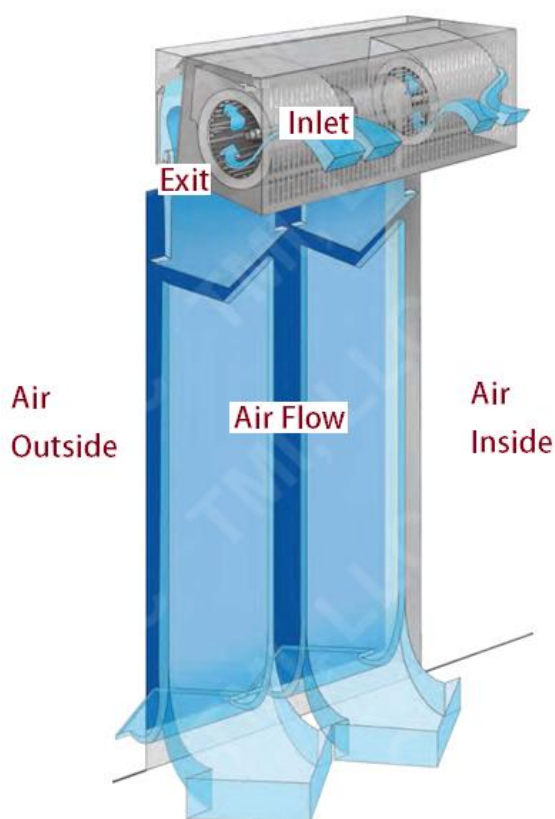


Figure 1.3 Schematic of air curtain[29]

#### 1.4 Definition of Initial Condition

The flow condition at the jet origin is often termed as the initial condition, which mainly consists of the exit Reynolds number and nature of exit velocity profile. In the present work, the attention will be mainly focused on two subjects, i.e., the exit Reynolds number and nature of mean exit velocity profile.

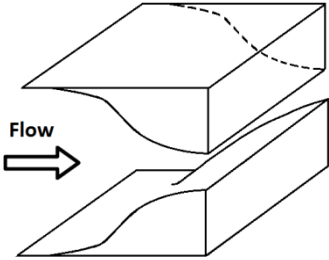
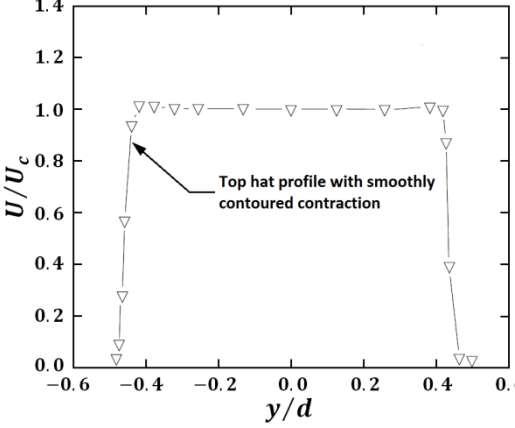
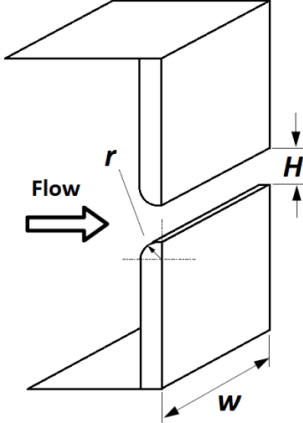
##### 1.4.1 Exit Reynolds Number

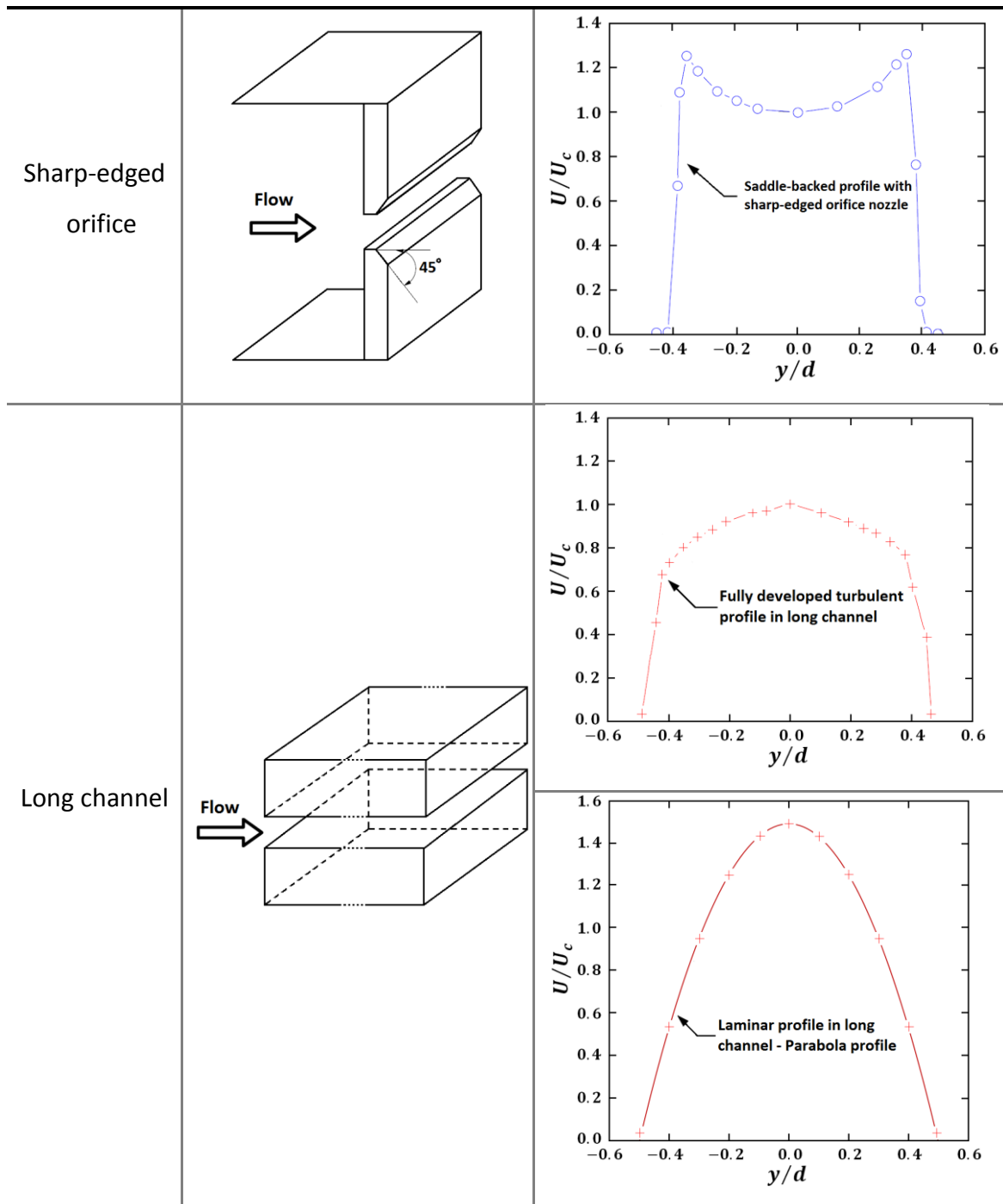
For plane jet, the exit Reynolds number is usually defined using the height of jet exit  $d$ , exit mean bulk velocity  $U_b$  and kinematic viscosity  $\nu$  of the fluid, which is

expressed as

$$Re = \frac{U_b d}{\nu}. \tag{1.10}$$

Table 1.1 Inner-wall nozzle exit contraction profile and exit mean velocity profile

Type	Schematic	Exit mean velocity profile
Smoothly contoured		
Radially contoured	 <p data-bbox="395 1464 783 1787">The nozzle contraction profile factor is defined by</p> $r^* = r/H$ <p data-bbox="395 1637 783 1787">where <math>r</math> is the inner-wall contraction radius and <math>H</math> is the nozzle opening width.</p>	<p data-bbox="807 1066 1326 1272">With a very small <math>r^*</math> (<math>&lt; 0.5</math>), the exit mean velocity profile is similar to the case with the sharp-edged orifice nozzle.</p> <hr/> <p data-bbox="807 1464 1326 1671">With a large <math>r^*</math> (<math>&lt; 2.0</math>), the exit mean velocity profile is similar to the case with the smoothly contoured contraction nozzle.</p>



### 1.4.2 Exit Velocity Profile

The nature of exit velocity profile is defined based on the features of the mean flow and the flow turbulent intensity at the jet exit, which are determined by some factors in real plane jet, including the nozzle aspect ratio, the inner-wall nozzle exit contraction profile and the effects of sidewalls.

The typical nozzle geometry for plane jet is rectangular, and the nozzle aspect ratio is the ratio of the long side length to the short side length of the rectangular

nozzle. It has been checked this parameter must be large enough to ensure the statistical two-dimension of flow and being free from the effects of sidewalls[15].

Another important factor to affect the exit velocity profile is the inner-wall nozzle exit contraction profile, which can be smoothly or radially contoured, sharp-edged or consists of a long channel. The relation between the inner-wall nozzle exit profiles and the exit mean velocity profiles is shown in Table 1.1, where the experimental data were extracted from the work of Deo et al.[16]. In the configuration of plane jet experiment, the sidewalls are necessary to force the flow to behave in a statistically two-dimensional manner. However, the installation of sidewalls will impose an additional boundary condition in x-y plane on plane jet, which indicates the effects of sidewalls on the exit velocity profile should be evaluated in the experimental study[14].

### **1.5 Motivation for Present Study**

On the basis of the past researches on the plane jet, it is clear that, even though both the experimental data and numerical results are required to study the features of the plane jet, the numerical simulation is quite promising accompanied by the improvement of calculation capacity of scientific computer, which can easily achieve the simultaneous parameters' acquirement and avoid the effects of external disturbances on the evolution of jet flows in the experiments.

In addition, the transport and mixing processes of passive scalar in turbulent shear flows are of great interests due to their importance to the diffusion of contaminants in environmental flows as well as the wide range of applications involving turbulent combustion. The evolution characteristics of velocity field and scalar field should be simultaneously studied.

Moreover, although some researches on the effects of initial conditions (mainly the Reynolds number and the initial velocity profile) on the evolution of plane jets have been done, only one kind of initial conditions is usually considered in one single work; the cross-impact or overlapping effects between these initial conditions have not been discussed.

Meanwhile, the most sufficient study on the plane jet in the past was obvious about the flow characteristics in the fully developed region with quite large exit



Reynolds number. The flow transition or development with moderate or small Reynolds number should be investigated more.

### **1.6 Study Objectives**

With a view to the above analysis, in the present study, the direct numerical simulations of plane jets are carried out. The flow characteristics of turbulent plane jets are mainly investigated in view of the velocity and scalar fields, meanwhile I focus on the effects of the flow initial conditions, i.e., exit Reynolds number and exit mean velocity profile, on the spatial development of the flow on the basis of the simulation results about the instantaneous and mean flow field.

In addition, the features and evolution of coherent structure and the interface between the plane jet and the ambient fluid are also observed in the plane jets with different initial conditions.

The kinematics, dynamics and local structure of the planar jet in the fine-scale are studied by analyzing the evolution of the invariants of the velocity gradient tensor. Meanwhile, the effects of the initial condition on the flow evolution are also assessed, particularly the characteristic features of the planar jet in the inhomogeneous transition zone.

### **1.7 Thesis Outline**

In chapter 1, the past study on the plane jet is reviewed first. Following the analysis of the basic characteristics and initial conditions of the plane jet, the motivation and study objectives are introduced.

In chapter 2, the history of the utilization of the numerical simulation in plane jet study will be recalled. And the important information about my DNS are introduced, including the governing equations, the non-dimensionalization and discretization of the governing equations, the grid system, the solution of Poisson equation and others. The computational domain and the definition of the initial and boundary conditions are also presented.

In chapter 3, the influence of exit Reynolds number on the plane jet will be studied. Based on the instantaneous and statistical results, the streamwise and lateral

evolution of mean and turbulent variables, and the transport of mean streamwise momentum and mean scalar are mainly investigated.

In chapter 4, both the characteristics of the plane jets with two kinds of exit mean velocity profiles and the cross impact between two initial factors, i.e., exit  $Re$  and mean velocity profile, are presented and discussed, based on the instantaneous and statistical results, including the streamwise and lateral evolution of mean and turbulent variables, and the transport of mean streamwise momentum and mean scalar.

In chapter 5, the influence of exit  $Re$  and mean velocity profile on turbulence structure in plane jet is studied on the basis of the characteristics and evolution of coherent structure and the interface between the jet and the ambient flow.

In chapter 6, by the computation of the invariants of the velocity-gradient, rate-of-strain, rate-of-rotation tensors, the investigation will provide the information on the dynamics, topology, and geometry of the plane jet in the fine scale.

In chapter 7, the overall conclusions of the present thesis are presented and some prospects about the future study are also introduced and discussed.

## References

- [1] SCHLICHTING V. H. Laminare strahlausbreitung[J]. Ztschr. f. angew. Math. und Mech., **1933**, 13: 260-263. (in German)
- [2] FORTHMAN E. Turbulent jet expansion[J]. Ingenieur-Archiv, **1934**, 5(1): 42-54. (in German)
- [3] MILLER D. R. and COMINGS E. W. Static pressure distribution in the free turbulent jet[J]. Journal of Fluid Mechanics, **1957**, 3: 1-16.
- [4] KNYSTAUTAS R. The turbulent jet from a series of holes in line[J]. Aeronaut. Q., **1964**, 15: 1-28.
- [5] BRADBURY L. J. S. The structure of a self-preserving turbulent plane jet[J]. Journal of Fluid Mechanics, **1965**, 23(1): 31-64.
- [6] HESKESTAD G. Hot-wire measurements in a plane turbulent jet[J]. Trans. Journal of Applied Mechanics, **1965**, 32(4): 721-734.
- [7] GUTMARK E. and WYGNANSKI I. The planar turbulent jet[J]. Journal of Fluid

- Mechanics, **1976**, 73(3): 465-495.
- [8] JENKINS P. E. and GOLDSCHMIDT V. W. Mean temperature and velocity in a plane turbulent jet[J]. Trans. ASME: J. Fluids Engineering, **1973**, 95: 581-584.
- [9] THOMAS F. O. and GOLDSCHMIDT V. W. Structure characteristics of a developing turbulent planar jet[J]. Journal of Fluid Mechanics, **1986**, 163: 227-256.
- [10] GEORGE W. K. Advances in Turbulence - The self-preservation of turbulent flows and its relation to initial conditions and coherent structures[M]. Berlin, Germany: Springer-Verlag, **1989**: 39-73.
- [11] GORDEYEV S. V. and THOMAS F. O. Coherent structure in the turbulent planar jet- Part 2. Structural topology via POD eigenmode projection[J]. Journal of Fluid Mechanics, **2002**, 460: 349-380.
- [12] ATASSI O. V. and LUEPTOW R. M. A model of flapping motion in a plane jet[J]. European Journal of Mechanics B/Fluids, **2002**, 21: 171-183.
- [13] DEO R. C., MI Jian-chun and NATHAN G. J. The influence of Reynolds number on a plane jet[J]. Physics of Fluids, **2008**, 20(7): 075108.
- [14] DEO R. C., NATHAN G. J. and MI Jian-chun Comparison of turbulent jets issuing from rectangular nozzles with and without sidewalls[J]. Experimental Thermal and Fluid Science, **2007**, 32: 596-606.
- [15] DEO R. C., MI Jian-chun and NATHAN G. J. The influence of nozzle aspect ratio on plane jets[J]. Experimental Thermal and Fluid Science, **2007**, 31(8): 825-838.
- [16] DEO R. C., MI Jian-chun and NATHAN G. J. The influence of nozzle-exit geometric profile on statistical properties of a turbulent plane jet[J]. Experimental Thermal and Fluid Science, **2007**, 32(2): 545-559.
- [17] SURESH P. R., SRINIVASAN K., SUNDARARAJAN T. and DAS S. K. Reynolds number dependence of plane jet development in the transitional regime[J]. Physics of Fluids, **2008**, 20(4): 044105.
- [18] TERASHIMA O., SAKAI Y. and NAGATA K. Simultaneous measurement of velocity and pressure in a plane jet[J]. Experiments in Fluids, **2012**, 53: 1149-1164.
- [19] SHIM Y. M., SHARMA R. N. and RICHARDS P. J. Proper orthogonal decomposition analysis of the flow field in a plane jet[J]. Experimental Thermal and Fluid Science, **2013**, 51: 37-55.
- [20] SAKAKIBARA J. Plane jet excited by disturbances with spanwise phase variations[J].

- Experiments in Fluids, **2013**, 54: 1620.
- [21] DEO R. C., NATHAN G. J. and MI Jian-chun Similarity analysis of the momentum field of a subsonic, plane air jet with varying jet-exit and local Reynolds numbers[J]. Physics of Fluids, **2013**, 25(1): 015115.
- [22] ORSZAG S. A. and PATTERSON G. S. Numerical simulation of three-dimensional homogenous isotropic turbulence[J]. Physical Review Letters, **1972**, 28(2): 76-79.
- [23] COMTE P., LESIEUR M., LAROCHE H. and NORMAND X. Numerical simulations of turbulent plane shear layers[J]. Turbulent Shear Flows, **1989**, 6: 360-380.
- [24] STANLEY S. A. and SARKAR S. Simulations of spatially developing two-dimensional shear layers and jets[J]. Theoretical and Computational Fluid Dynamics, **1997**, 9(2): 121-147.
- [25] STANLEY S. A., SARKAR S. and MELLADO J. P. A study of the flow-field evolution and mixing in a planar turbulent jet using direct numerical simulation[J]. Journal of Fluid Mechanics, **2002**, 450: 377-407.
- [26] KLEIN M., SADIKI A. and JANICKA J. Investigation of the influence of the Reynolds number on a plane jet using direct numerical simulation[J]. International Journal of Heat and Fluid Flow, **2003**, 24: 785-794.
- [27] Da SILVA C. B. and PEREIRE J. C. F. Invariants of the velocity-gradient, rate-of-strain, and rate-of-rotation tensors across the turbulent/nonturbulent interface in jets[J]. Physics of Fluids, **2008**, 20: 055101.
- [28] RAJARATNAM N. Turbulent jets[M]. Amsterdam, the Netherlands: Elsevier Scientific Publishing Company, **1976**:2-5.
- [29] How air curtains & air doors work. Air curtains & air doors from [www.tmi-pvc.com](http://www.tmi-pvc.com).

*[J]: Journal Article*

*[M]: Monograph*

*[C]: Conference Proceeding*

## Chapter 2

### DNS OF PLANE JET

The complex behavior of turbulence is the consequence of a fairly simple set of equations, i.e., the Navier–Stokes equations. A complete description of the turbulent flow, in which the flow variables (e.g. velocity and pressure) are known as the function of space and time, can therefore be obtained by numerically solving the Navier–Stokes equations. These numerical solutions are termed numerical simulation of turbulence. Generally, the numerical simulation of turbulence ranges from direct numerical simulation (DNS), in which the whole range of spatial and temporal scales of the turbulence is resolved without the use of any turbulence models, to Reynolds Averaged Navier–Stokes (RANS), in which only the mean flow is directly resolved while all turbulence scales are modeled. The simulation based on DNS can get the highest predictive accuracy but consumes the greatest computational cost; oppositely, the use of RANS in the turbulence simulation can help acquire the information of flow with quite high Reynolds number. Another method, named large eddy simulation (LES), lies between DNS and RANS, in which only the dynamics of larger energy-containing eddies are directly resolved meanwhile the effects of the smaller eddies are modeled based on some subgrid scale model. The validity of LES is strongly connected with the modeling of subgrid scales in different flow condition but a universal qualifying model in LES has not been established. For studying the characteristics of plane jet with different initial conditions, DNS should be the most proper choice in the numerical simulation.

#### 2.1 Introduction to Numerical Simulation of Plane Jet

The numerical simulation focusing on the plane jet began quite late, which was almost 50 years later than the first experimental investigation. In the latter 80s, Comte

et al.[1] performed the first direct temporal simulations of the fully developed region of a two-dimensional Bickley jet, in which two kinds of initial perturbations were set in his simulation, and the work showed the pairing of vortices only happened in the condition with the white-noise perturbation and cannot be detected in the condition with a sine perturbation at a discrete wavelength. Dai et al.[2] performed the first simulation on the spatially evolving plane jet, in which a large-eddy simulation (LES) using a Smagorinsky model was carried out. The important work on the DNS of the spatially evolving plane jet was performed by Stanley and Sarkar[3][4], in their work the coherency spectra, vorticity visualization and autospectra were obtained to identify inferred structure, furthermore, the large- and small-scale anisotropies and the mixing process in plane jet were discussed, which illustrated the mixing process is dominated by large-scale engulfing of fluid after the rollup of vertical structures in the shear layers, however, small-scale mixing dominates further downstream in the turbulent core of the self-similar region of the jet. Ribault et al.[5][6] evaluated the performance of different subgrid models in LES, including the standard Smagorinsky, the dynamic Smagorinsky, and the dynamic mixed models, and studied the evolution of a passive scalar based on the latter two models, which claimed that the dynamic mixed model provided a much better representation of the sub-grid stress tensor, but the main characteristics of the PDFs of the passive scalar were still found to be broader than in DNS and the peaks were smoother. Rembold et al.[7] carried out the DNS of a transitional rectangular jet with a small aspect ratio 5 and a moderate exit Reynolds number 2,000, the transition process was investigated, which showed how the initially two-dimensional disturbances in the inflow region of the jet rapidly grow three dimensional and then lead to a breakdown of the jet to small-scale turbulence. Klein et al.[8] performed the DNS of plane jet in a range of Reynolds number from 1,000 to 6000, the significant influence of exit Reynolds number on the jet development were evaluated in the studied conditions of their work. Liu et al.[9] contrasted the mixed-nonlinear Kosović, Leray and LANS- $\alpha$  subgrid scale models with linear Smagorinsky and Yoshizawa models by the LES of plane jet at  $Re = 4,000$ . The recent work on the DNS of plane jet was supplied by da Silva et al.[10], who analyzed the evolution of the invariants of the velocity gradient, rate-of-strain, and rate-of rotation tensors across the turbulent/non-turbulent interface in order to clarify the kinematics,

dynamics, and topology of the flow during the entrainment process in the fully developed flow region.

## 2.2 Governing Equations and Non-dimensionalization

### 2.2.1 Non-dimensionalization of Governing Equations

Non-dimensionalization of equations is the conversion of the original equations to the form which is easier to use and contain less free parameters in the problem to be studied. Here, I select the general form of Navier–Stokes equations as an example to show the process of non-dimensionalization of equations, which is written as

$$\rho \left( \frac{\partial \tilde{\mathbf{u}}}{\partial t} + \tilde{\mathbf{u}} \cdot \nabla \tilde{\mathbf{u}} \right) = -\nabla \tilde{p} + \mu \nabla^2 \tilde{\mathbf{u}} + \tilde{\mathbf{f}}, \quad (2.1)$$

where  $\tilde{\mathbf{u}}$  is the instantaneous velocity vector,  $\rho$  is the density of fluid,  $\tilde{p}$  is the instantaneous pressure,  $\mu$  is the dynamic viscosity, and  $\tilde{\mathbf{f}}$  is the instantaneous body force vector.

The non-dimensionalization of variables in the above equation follows the principle through selection of appropriate scales, which is as follows:

Table 2.1 Non-dimensionalization of variables

Scale	Dimensionless variable
Length $L$	$x' = x/L \quad y' = y/L \quad z' = z/L$
Velocity $U$	$\tilde{u}' = \tilde{u}/U$
Scalar $\Theta$	$\tilde{\theta}' = \tilde{\theta}/\Theta$
Time $L/U$	$t' = t/(L/U)$

$$\tilde{p}' = \tilde{p}/(\rho U^2)$$

Pressure (there is no natural selection for the pressure scale)

where dynamic effects are dominant, i.e., high velocity flows.

$$\tilde{p}' = \tilde{p}/(\mu U/L)$$

where viscous effects are dominant, i.e., creeping flows.

After substitute the dimensionless variables for the original variables in Equation (2.1), the non-dimensionalized Navier-Stokes equation obtained is

$$\frac{\partial \tilde{\mathbf{u}}'}{\partial t'} + \tilde{\mathbf{u}}' \cdot \nabla \tilde{\mathbf{u}}' = -\nabla \tilde{p}' + \frac{1}{\text{Re}} \nabla^2 \tilde{\mathbf{u}}' + \tilde{\mathbf{f}} \frac{L}{U^2}. \quad (2.2)$$

Following the same procedure, the continuity equation and scalar transport equation can also be non-dimensionalized.

### 2.2.2 Governing Equations

In DNS, the conservation equations of mass and momentum, i.e., the continuity equation and the Navier–Stokes equations, and the scalar transport equation in their instantaneous local dimensionless form for an incompressible flow are investigated and solved, shown by

$$\left\{ \begin{array}{l} \frac{\partial \tilde{u}'_i}{\partial x'_i} = 0 \\ \frac{\partial \tilde{u}'_i}{\partial t'} + \tilde{u}'_j \frac{\partial \tilde{u}'_i}{\partial x'_j} = \frac{1}{\text{Re}} \frac{\partial^2 \tilde{u}'_i}{\partial x'_j \partial x'_j} - \frac{\partial \tilde{p}'}{\partial x'_i}, \\ \frac{\partial \tilde{\theta}'}{\partial t'} + \tilde{u}'_j \frac{\partial \tilde{\theta}'}{\partial x'_j} = \frac{1}{\text{PrRe}} \frac{\partial^2 \tilde{\theta}'}{\partial x'_j \partial x'_j} \end{array} \right. \quad (2.3)$$

where  $d$  (the height of the jet exit),  $U_b$  (the exit mean bulk velocity),  $\theta_b$  (the flux-averaged exit mean scalar), and their combinations are used to non-dimensionalize the variables in the governing equations,  $\tilde{u}'_i$  is the dimensionless instantaneous velocity,  $\tilde{p}'$  is the dimensionless instantaneous pressure,  $\tilde{\theta}'$  is the dimensionless instantaneous scalar,  $\text{Pr} (= \nu/\alpha : \nu$  is the kinematic viscosity and  $\alpha$  is the scalar diffusivity) is the Prandtl number, and  $\text{Re} (=U_b d/\nu)$  is the exit Reynolds



number. The solutions of the Navier–Stokes equations and the scalar transport equation describe the velocity and scalar fields, respectively.

## 2.3 Discretization of Governing Equations

### 2.3.1 Temporal Discretization

The temporal discretization of governing equations is based on a hybrid implicit/explicit method, which is the combination of second-order Crank–Nicolson method and third-order Runge–Kutta method. The temporal discretization of governing equations is performed based on the numerical method, presented by Le and Moin, which is based on the fractional step method in conjunction with the predictor-corrector technique of Runge–Kutta genre[11][12]. Firstly, the famous fractional step, or time-split method, is in general a method of approximation of the equations based on decomposition of the operators they contain. In application of this method to the Navier–Stokes equations, the role of pressure can be interpreted in the momentum equations as a projection operator which projects an arbitrary vector field into a divergence-free vector field

Based on the above method, a three-step time advancement scheme for Equation Set (2.3) is written as

$$\delta \tilde{u}_i^k / \delta x_i = 0, \quad (2.4)$$

$$\begin{aligned} \frac{\tilde{u}_i^k - \tilde{u}_i^{k-1}}{\Delta t} = & \alpha_k L(\tilde{u}_i^{k-1}) + \beta_k L(\tilde{u}_i^k) - \gamma_k N(\tilde{u}_i^{k-1}) - \zeta_k N(\tilde{u}_i^{k-2}) \\ & - (\alpha_k + \beta_k) \frac{\delta \tilde{p}^k}{\delta x_i}, \end{aligned} \quad (2.5)$$

$$\frac{\tilde{\theta}_i^k - \tilde{\theta}_i^{k-1}}{\Delta t} = \alpha_k L(\tilde{\theta}_i^{k-1}) + \beta_k L(\tilde{\theta}_i^k) - \gamma_k N(\tilde{\theta}_i^{k-1}) - \zeta_k N(\tilde{\theta}_i^{k-2}), \quad (2.6)$$

$$i = 1, 2, 3 \text{ and } k = 1, 2, 3$$

where  $k$  denotes the sub-step number,  $\alpha_k$ ,  $\beta_k$ ,  $\gamma_k$  and  $\zeta_k$  are the coefficients corresponding to certain algorithm,  $\delta/\delta x_i$  is the finite difference operator, and  $L(\tilde{u}_i)$  and  $L(\tilde{\theta}_i)$  represent the finite difference approximations to the viscous terms, meanwhile  $N(\tilde{u}_i)$  and  $N(\tilde{\theta}_i)$  represent the finite difference approximations to the convective terms.

The coefficients are selected to ensure that the total time advancement between  $t^n$  and  $t^{n+1}$  is third-order accurate for the convective term and second-order for viscous term (implicit Crank-Nicolson method), which are:

$$\begin{aligned}\alpha_1 &= \beta_1 = 4/15, & \alpha_2 &= \beta_2 = 1/15, & \alpha_3 &= \beta_3 = 1/6, \\ \gamma_1 &= 8/15, & \gamma_2 &= 5/12, & \gamma_3 &= 3/4, \\ \zeta_1 &= 0, & \zeta_2 &= -17/60, & \zeta_3 &= -5/12,\end{aligned}$$

and  $\sum_{k=1}^3(\alpha_k + \beta_k) = \sum_{k=1}^3(\gamma_k + \zeta_k) = 1$ , it shows that the effective time step for one sub-step is  $(\alpha_k + \beta_k)\Delta t$ , i.e.,  $8/15 \Delta t$  for the first sub-step,  $2/15 \Delta t$  for the second sub-step and  $1/3 \Delta t$  for the third sub-step.

Then, the fractional step method is applied to Equations (2.4) and (2.5), the result is

$$\frac{\hat{u}_i^k - \tilde{u}_i^{k-1}}{\Delta t} = (\alpha_k + \beta_k)L(\tilde{u}_i^{k-1}) + \beta_k L(\hat{u}_i^k - \tilde{u}_i^{k-1}) - \gamma_k N(\tilde{u}_i^{k-1}) - \zeta_k N(\tilde{u}_i^{k-2}) \quad (2.7)$$

and

$$\frac{\tilde{u}_i^k - \hat{u}_i^k}{\Delta t} = -\frac{\delta \tilde{\phi}^k}{\delta x_i}, \quad (2.8)$$

where  $\tilde{\phi}^k$  and  $\tilde{p}^k$  are related by

$$\frac{\delta \tilde{\phi}^k}{\delta x_i} = (\alpha_k + \beta_k) \frac{\delta \tilde{p}^k}{\delta x_i} - \beta_k L(\tilde{u}_i^k - \hat{u}_i^k). \quad (2.9)$$

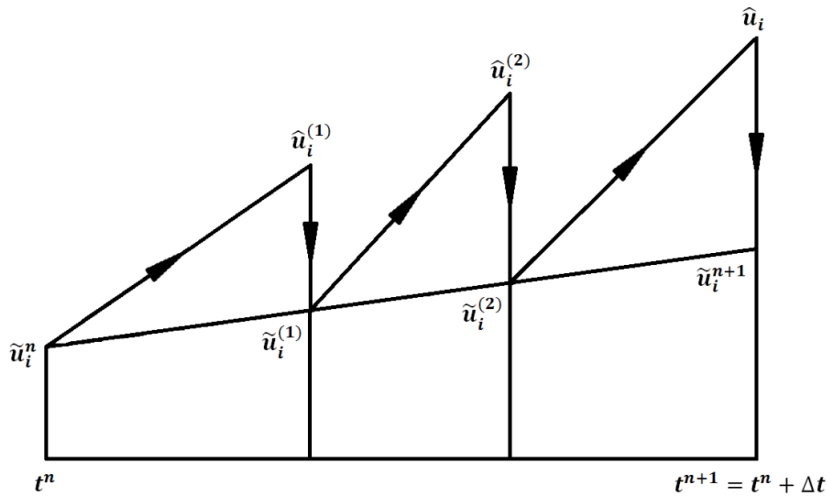


Figure 2.1 Temporal discretization scheme in computation of instantaneous velocity

Combining Equation (2.8) with the divergence free constraint, i.e., Equation (2.4), we will confront the discrete Poisson equation, which is

$$\frac{\delta^2 \tilde{\phi}^k}{\delta x_i \delta x_i} = \frac{1}{\Delta t} \frac{\delta \hat{u}_i^k}{\delta x_i}. \quad (2.10)$$

At each sub-step, Equations (2.7) and (2.10) are solved to compute the velocity field and Equation (2.6) is solved to compute the scalar field. Here, Figure 2.1 shows the schematic diagram of above scheme for the computation of instantaneous velocity, where the vertical arrows represent the enforcement of the continuity equation, i.e., the solution of Poisson equation, at each sub-step.

### 2.3.2 Spatial Discretization

The central difference scheme is used for the spatial discretization of each spatial derivative term in the governing equations, except the viscous terms along the lateral direction, which is discretized by the second-order Crank–Nicolson method, herein the implicit treatment of the viscous terms will eliminate the numerical viscous stability restriction, particularly for low-Reynolds-number flow. Considering the choices about the exit Reynolds number, this scheme will be proper.

Finite difference formulas are derived from Taylor series expansions. The Taylor series is:

$$f(x_{j+1}) = f(x_j) + (x_{j+1} - x_j)f'(x_j) + \frac{(x_{j+1} - x_j)^2}{2}f''(x_j) + \dots \quad (2.11)$$

Taking a rearrangement, it leads to

$$f'(x_j) = \frac{f(x_{j+1}) - f(x_j)}{\Delta x_j} - \frac{\Delta x_j}{2}f''(x_j) + \dots, \quad (2.12)$$

where  $\Delta x_j = x_{j+1} - x_j$  is the mesh size, the first term on the right-hand side of Equation (2.12) is a finite difference approximation to the first derivative, the next term is the leading error term. When the grid points are uniformly spaced, Equation (2.12) can be written as

$$f'_j = \frac{f_{j+1} - f_j}{h} + O(h^1), \quad (2.13)$$

which is referred to as the first-order forward difference. The exponent of  $h$  in

$O(h^\alpha)$  is the order of accuracy of the method, and the first-order forward difference is first-order accuracy.

By expanding  $f_{j-1}$  about  $x_j$ , we can get the first-order backward difference formula

$$f'_j = \frac{f_j - f_{j-1}}{h} + O(h^1). \quad (2.14)$$

Higher order schemes can be derived by Taylor series of the function  $f$  at different points about the point  $x_j$ . In present study, the fourth order central difference for the first derivative and the second order central difference for the second derivative were used, which are respectively:

$$f'_j = \frac{f_{j-2} - 8f_{j-1} + 8f_{j+1} - f_{j+2}}{12h} + O(h^4) \quad (2.15)$$

and

$$f''_j = \frac{f_{j+1} - 2f_j + f_{j-1}}{h^2} + O(h^2). \quad (2.16)$$

Furthermore, it is known non-uniform grids are often used when the function  $f$  varies rapidly in a part of the domain, but has a mild variation elsewhere. In plane jet, the lateral evolution of flow near the jet centerline is more notable than the one elsewhere. That will be logical that the non-uniform grids should be used in the lateral direction for the construction of grid system, and the finer grids are used near the jet centerline. Here, the typical finite difference formulas for first and second derivatives are shown as

$$f'_j = \frac{f_{j+1} - f_{j-1}}{x_{j+1} - x_{j-1}} + O(h^1), \quad (2.17)$$

and

$$f''_j = 2 \left[ \frac{f_{j-1}}{h_j(h_j + h_{j+1})} - \frac{f_j}{h_j h_{j+1}} + \frac{f_{j+1}}{h_{j+1}(h_j + h_{j+1})} \right] + O(h^1), \quad (2.18)$$

where  $h_j = x_j - x_{j-1}$ . Moreover, finite difference formulas for non-uniform meshes generally have a lower order of accuracy than their counterparts with the same stencil but defined for uniform meshes.

## 2.4 Finite difference schemes in staggered grid systems

Generally, the conventional numerical algorithms based on a structured computational grid fall into three classes: regular, staggered, and collocated grid systems, where it is known[13] that the discretization of the partial differential flow equations on a mesh with collocated variables, e.g. in the regular or collocated grid systems, can give rise to a spurious mode (a  $\pi$ -wave) for the pressure, when the cell-face velocities are linearly interpolated between the neighboring nodes without pressure stabilization and when the pressure term in the momentum equations is approximated by central differencing, which will result in a solution without physical meaning. However, by using a staggered grid, the odd-even decoupling between the pressure and velocity can be avoided; meanwhile the staggered grid system is mainly used on structured grids for both compressible and incompressible flow simulations.

### 2.4.1 Staggered Grid System

In the staggered grid system, the velocity or momentum variables are located on the cell face, and the scalar and pressure variables are stored in the cell center of the control volume, which is shown by Figure 2.2.

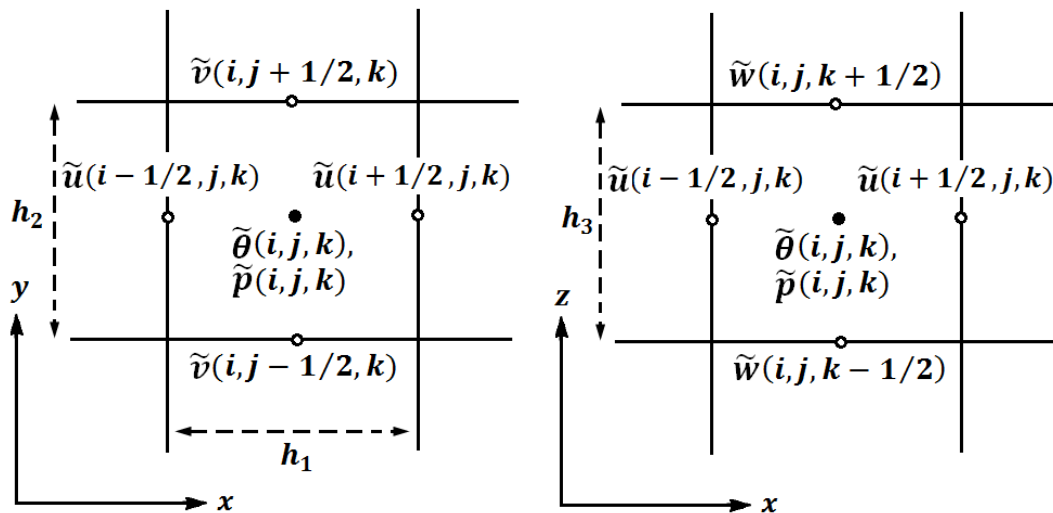


Figure 2.2 Staggered grid system and storage of variables

The second order discretization schemes for the mass and momentum conservation equations in the staggered grid system are[14]

$$\frac{\tilde{u}_{i+1/2,j,k}^{n+1} - \tilde{u}_{i-1/2,j,k}^{n+1}}{\Delta x} + \frac{\tilde{v}_{i,j+1/2,k}^{n+1} - \tilde{v}_{i,j-1/2,k}^{n+1}}{\Delta y} + \frac{\tilde{w}_{i,j,k+1/2}^{n+1} - \tilde{w}_{i,j,k-1/2}^{n+1}}{\Delta z} = 0 \quad (2.19)$$

and

$$\begin{aligned} & \frac{\tilde{u}_{i+1/2,j,k}^{n+1} - \tilde{u}_{i+1/2,j,k}^n}{\Delta t} + C_h(\tilde{u}_h, \tilde{v}_h, \tilde{w}_h) + \frac{\tilde{p}_{i+1,j,k}^{n+1} - \tilde{p}_{i,j,k}^{n+1}}{\Delta x} = \\ & \frac{\tilde{\tau}_{i+1,j,k}^{(11)} - \tilde{\tau}_{i,j,k}^{(11)}}{\Delta x} + \frac{\tilde{\tau}_{i+1/2,j+1/2,k}^{(12)} - \tilde{\tau}_{i+1/2,j-1/2,k}^{(12)}}{\Delta y} + \frac{\tilde{\tau}_{i+1/2,j,k+1/2}^{(13)} - \tilde{\tau}_{i+1/2,j,k-1/2}^{(13)}}{\Delta z}, \end{aligned} \quad (2.20)$$

where the superscripts  $n + 1$  represent these formulas have to be satisfied at the next time step, and in Equation (2.20),  $\tilde{\tau}^{(11)}$ ,  $\tilde{\tau}^{(12)}$  and  $\tilde{\tau}^{(13)}$  are the stress tensors,  $C_h(\tilde{u}_h, \tilde{v}_h, \tilde{w}_h)$  contains the convective terms which don't possess a natural discretization, where the interpolations are required.

#### 2.4.2 Fully Conservative Fourth Order Finite Difference Scheme in a Staggered Grid System[14]

By taking the convective term in Navier–Stokes equations as an example, the fully conservative fourth order finite difference scheme used in the present study is introduced.

Firstly, three forms of the convective term are defined as

$$(\text{Div.})_i \equiv \frac{\partial u_j u_i}{\partial x_j}, \quad (2.21)$$

$$(\text{Adv.})_i \equiv u_j \frac{\partial u_i}{\partial x_j}, \quad (2.22)$$

and

$$(\text{Skew.})_i \equiv \frac{1}{2} \frac{\partial u_j u_i}{\partial x_j} + \frac{1}{2} u_j \frac{\partial u_i}{\partial x_j}, \quad (2.23)$$

where  $(\text{Div.})_i$ ,  $(\text{Adv.})_i$ , and  $(\text{Skew.})_i$  are referred to the divergence, advective and skew-symmetric forms, respectively. The fourth order accurate schemes for the discretization of Equations (2.21), (2.22) and (2.23) are

$$(\text{Div.})_i \equiv \frac{9}{8} \frac{\delta_1}{\delta_1 x_j} \left[ \left( \frac{9}{8} \bar{u}_j^{1x_i} - \frac{1}{8} \bar{u}_j^{3x_i} \right) \bar{u}_i^{1x_i} \right] - \frac{1}{8} \frac{\delta_3}{\delta_3 x_j} \left[ \left( \frac{9}{8} \bar{u}_j^{1x_i} - \frac{1}{8} \bar{u}_j^{3x_i} \right) \bar{u}_j^{3x_j} \right], \quad (2.24)$$

$$(\text{Adv.})_i \equiv \frac{9}{8} \left( \frac{9}{8} \bar{u}_j^{1x_i} - \frac{1}{8} \bar{u}_j^{3x_i} \right) \frac{\delta_1 u_i}{\delta_1 x_j} - \frac{1}{8} \left( \frac{9}{8} \bar{u}_j^{1x_i} - \frac{1}{8} \bar{u}_j^{3x_i} \right) \frac{\delta_3 u_i}{\delta_3 x_j}, \quad (2.25)$$

and

$$(\text{Skew.})_i \equiv \frac{1}{2} (\text{Div.})_i + \frac{1}{2} (\text{Adv.})_i, \quad (2.26)$$

where the finite difference operator with stencil  $n$  acting on  $\psi$  with respect to  $x_1$  is defined as

$$\frac{\delta_n \psi}{\delta_n x_1} \Big|_{x_1, x_2, x_3} \equiv \frac{\psi(x_1 + n h_1/2, x_2, x_3) + \psi(x_1 - n h_1/2, x_2, x_3)}{n h_1},$$

and an interpolation operator with stencil  $n$  acting on  $\psi$  in the  $x_1$  direction is defined by

$$\bar{\psi}^{n x_1} \Big|_{x_1, x_2, x_3} \equiv \frac{\psi(x_1 + n h_1/2, x_2, x_3) + \psi(x_1 - n h_1/2, x_2, x_3)}{2},$$

and  $\psi$  represents the variable or the term.

The fourth order fully conservative finite difference scheme for the convective term in the skew-symmetric form is used in the present simulation, which was proved to be conservative in the transport equation of momentum if the discrete continuity relation is satisfied.

## 2.5 Solution of Poisson Equation

In the simulation, the conjugate gradient method (CGM) is used to solve the Poisson equation of pressure. CGM is an algorithm for the numerical solution of particular systems of linear equations, namely those whose matrix is symmetric and positive-definite, and often implemented as an iterative algorithm, applicable to sparse systems, which often arise when numerically solving partial differential equations, as in my case.

Here, the algorithm, CGM as an iterative method, is detailed below for solving the following system of linear equations for the vector  $\mathbf{x}$ ,

$$\mathbf{Ax} = \mathbf{b}$$

where the known  $n \times n$  matrix  $\mathbf{A}$  is symmetric, i.e.,  $\mathbf{A}^T = \mathbf{A}$ , positive definite,

$\mathbf{x}^T \mathbf{A} \mathbf{x} > 0$  for all non-zero vectors  $\mathbf{x}$  in  $\mathbf{R}^n$ , and real;  $\mathbf{b}$  is also known.

Firstly, we define the input vector  $\mathbf{x}_0$  as an approximate initial solution or  $\mathbf{0}$ , and then the initial residual is:

$$\mathbf{r}_0 = \mathbf{b} - \mathbf{A} \mathbf{x}_0,$$

then set  $\mathbf{p}_0 = \mathbf{r}_0$ , the iterative step is zero,  $k = 0$ , further the following process is repeated,

$$\alpha_k = \frac{\mathbf{r}_k^T \mathbf{r}_k}{\mathbf{p}_k^T \mathbf{A} \mathbf{p}_k}$$

$$\mathbf{x}_{k+1} = \mathbf{x}_k + \alpha_k \mathbf{p}_k$$

$$\mathbf{r}_{k+1} = \mathbf{r}_k - \alpha_k \mathbf{A} \mathbf{p}_k$$

$$\beta_k = \frac{\mathbf{r}_{k+1}^T \mathbf{r}_{k+1}}{\mathbf{r}_k^T \mathbf{r}_k}$$

$$\mathbf{p}_{k+1} = \mathbf{r}_{k+1} + \beta_k \mathbf{p}_k$$

$$k = k + 1$$

where, the exit of the loop is marked by a sufficiently small value of  $\mathbf{r}_{k+1}$  or the defined largest iterative step. After the loop is finished, we can get the result for  $\mathbf{x}$ , which is  $\mathbf{x}_{k+1}$ . [15]

Here, we take the one-dimensional Poisson equation,  $d^2\phi/dx^2 = f(x)$ , for example to show the solution based on CGM in the present simulation, the initial setting is

$$r_0 = f(x) - \frac{d^2\phi_0}{dx^2},$$

$$p_0 = r_0.$$

Then the loop is repeated as

$$\alpha_k = \frac{r_k^2}{p_k \frac{d^2\phi}{dx^2}}$$

$$f_{k+1} = u_k + \alpha_k p_k$$

$$r_{k+1} = r_k - \alpha_k \frac{d^2\phi}{dx^2}$$



$$\beta_k = \frac{r_{k+1}^2}{r_k^2}$$

$$p_{k+1} = r_{k+1} + \beta_k p_k$$

$$k = k + 1$$

The solution of  $d^2\phi/dx^2$  is  $f_{k+1}$  after the loop is conditionally ended.

## 2.6 Schematic of Computational Domain

The DNS of the spatially developing plane jet is performed in a 3-D computational region, which is constructed in the coordinate system nondimensionalized by the height of the jet exit ( $d$ ), as shown by Figure 2.3, where  $x'$  is the dimensionless streamwise coordinate along the jet centerline,  $y'$  is the dimensionless lateral coordinate, and  $z'$  is the dimensionless spanwise coordinate. Jet exit is set in the middle of the inlet plane, e.g. the  $x' = 0$  plane. The extension of the dimensionless computational domain is  $L_{x'} \times L_{y'} \times L_{z'} = 14\pi \times 14\pi \times 3\pi$ .

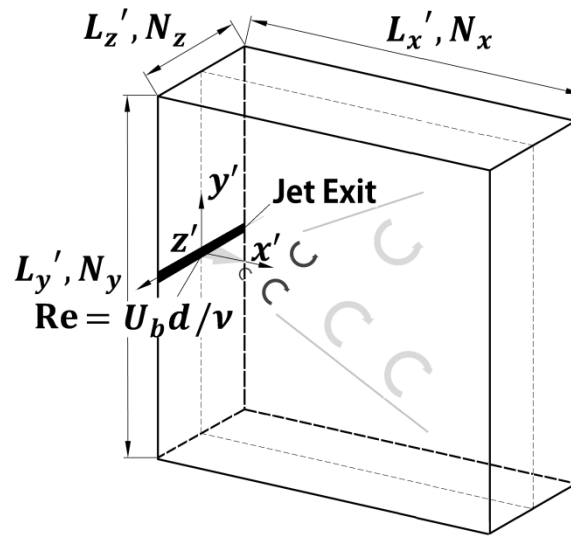


Figure 2.3 Schematic of computational domain

## 2.7 Initial and Boundary Conditions

### 2.7.1 Initial Condition

In the present research, the attention will be focused on two initial factors, the Reynolds number and mean velocity profile at the jet exit.

It is well-known that  $Re = 2,000$  appears to be about the lowest value for the flow transition to turbulence at a rough entrance[16]. I set three values for the exit Reynolds number, 1,000, 2,000 and 3,000, to capture the complete transition process to the fully-developed turbulence for the plane jet.

In order to resolve the flow motion in the smallest spatial scale (Kolmogorov microscale), theoretically, the grid scale at each location should be smaller than the corresponding Kolmogorov microscale. Based on the empirical equation proposed by Friehe et al.[17],

$$\eta = (48Re^3)^{-1/4} x, \quad (2.27)$$

where  $\eta$  is the Kolmogorov microscale,  $Re$  is the exit Reynolds number, and  $x$  is the streamwise coordinate, the  $\eta$  will be  $0.047d$  for  $Re = 1,000$ ,  $0.028d$  for  $Re = 2,000$ , and  $0.021d$  for  $Re = 3,000$  at the location of  $(L_x'/2, 0, 0)$ . In consideration of the capacity of the scientific computer, the grids numbers are set to be  $356(x) \times 356(y) \times 80(z)$  for  $Re = 1,000$ ,  $556(x) \times 556(y) \times 120(z)$  for  $Re = 2,000$ , and  $756(x) \times 756(y) \times 160(z)$  for  $Re = 3,000$  in the simulation.

In the streamwise ( $x$ -) and spanwise ( $z$ -)direction, uniform grids are set; however, the arrangement of grids in the lateral ( $y$ -) direction follows a hyperbolic tangent function, in which the finer grids are set near the jet center, that will allow for an accurate calculation near the jet center without excessive use of grids for the far field in the lateral direction.

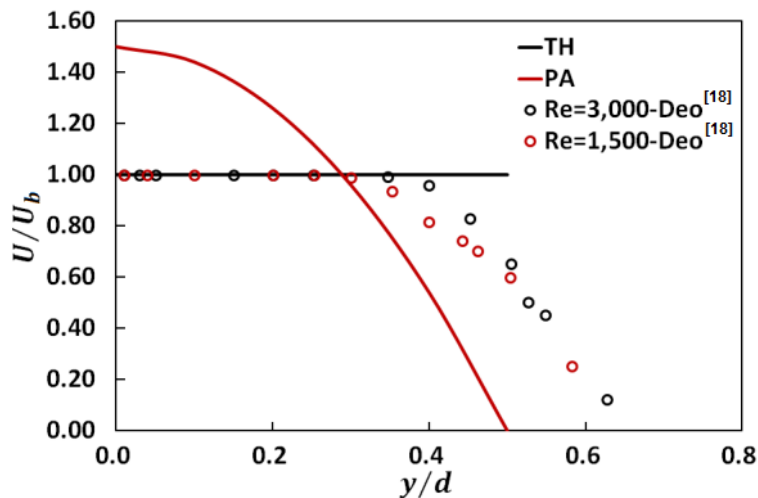


Figure 2.4 Mean streamwise velocity profiles at the jet exit

In the plane jet, mean velocity only contains the streamwise component at the jet exit. The exit profile of mean velocity is associated with the jet nozzle type and features of inflow, which will be a sort of the combinations of top hat profile and parabola profile. In addition, the mean streamwise velocity profile of the fully-developed laminar channel flow along the direction of channel height is parabolic shape. Following the above statement, in the present DNS, two ideal and typical mean velocity profiles, e.g. top hat profile (TH) and parabola profile (PA), are set at the jet exit and follow the same mass flux, which are shown in Figure 2.4. Meanwhile, the experimental profiles from the work of Deo et al. [18] were also pictured in Figure 2.4, which were captured at the streamwise location of  $x/d = 0.5$  from the jet exit.

The exit turbulence intensity is one percentile of the mean flow for velocity field, which is randomly distributed. For all cases, the exit mean scalar profiles possess the top hat shape and same scalar flux, and the exit turbulent scalar is zero.

In the simulation,  $Pr$  is set to be 0.7, which is the typical value for air. A low co-flow has been considered, where the ratio of the velocity between the low- and high- speed streams is 0.0599 for all cases.

### 2.7.2 Boundary Conditions

The computational domain is a region truncated from the fully physical domain, the boundary conditions should be appropriately chosen to close the difference between the flow in the numerical simulation and the real flow.

Following the characteristics of the plane jet in an infinite or large physical domain, for the velocity variables, the lateral boundary condition is set as the Neumann boundary condition, which is shown as  $\partial u'_i / \partial y' = 0$ ; for the pressure and scalar variables, the Dirichlet boundary condition is used at the lateral boundary, which are  $p' = 0$  and  $\theta' = 0$ .

One convective outflow condition, presented by Dai et al. [19], is applied at the downstream exit for velocity and scalar, which was verified to introduce little error into the interior of the computation domain, shown as

$$\begin{cases} \frac{\partial \tilde{u}'_i}{\partial t'} + U'(y') \frac{\partial \tilde{u}'_i}{\partial x'} = 0 \\ \frac{\partial \tilde{\theta}'}{\partial t'} + U'(y') \frac{\partial \tilde{\theta}'}{\partial x'} = 0 \end{cases}, \quad (2.28)$$

where  $U'(y')$  is the dimensionless convective velocity obtained by averaging the streamwise velocity over the spanwise direction at the downstream exit.

Moreover, for all the quantities the periodic boundary condition is imposed in the spanwise direction, where the plane jet is homogenous.

## References

- [1] COMTE P., LESIEUR M., LAROCHE H. and NORMAND X. Numerical simulations of turbulent plane shear layers[J]. *Turbulent Shear Flows*, **1989**, 6: 360-380.
- [2] DAI Y., KOBAYASHI T. and TANIGUCHI N. Large eddy simulation of plane turbulent jet flow using a new outflow velocity boundary condition[J]. *JSME International Journal. Series B, Fluids and Thermal Engineering*, **1994**, 37(2): 242-253.
- [3] STANLEY S. A. and SARKAR S. Simulations of spatially developing two-dimensional shear layers and jets[J]. *Theoretical and Computational Fluid Dynamics*, **1997**, 9(2): 121-147.
- [4] STANLEY S. A., SARKAR S. and MELLADO J. P. A study of the flow-field evolution and mixing in a planar turbulent jet using direct numerical simulation[J]. *Journal of Fluid Mechanics*, **2002**, 450: 377-407.
- [5] RIBAUT C. L., SARKAR S. and STANLEY S. A. Large eddy simulation of a plane jet[J]. *Physics of Fluids*, **1999**, 11(10): 3069-3083.
- [6] RIBAUT C. L., SARKAR S. and STANLEY S. A. Large eddy simulation of evolution of a passive scalar in plane jet[J]. *AIAA Journal*, **2001**, 39(8): 1509-1516.
- [7] REMBOLD B., ADAMS N. A. and KLEISER L. Direct numerical simulation of a transitional rectangular jet[J]. *International Journal of Heat and Fluid Flow*, **2002**, 23: 547-553.
- [8] KLEIN M., SADIKI A. and JANICKA J. Investigation of the influence of the Reynolds number on a plane jet using direct numerical simulation[J]. *International Journal of Heat and Fluid Flow*, **2003**, 24: 785-794.
- [9] LIU Y., TUCKER P. G. and KERR R. M. Linear and nonlinear model large-eddy simulations of a plane jet[J]. *Computers & Fluids*, **2008**, 37: 439-449.

- [10] Da SILVA C. B. and PEREIRE J. C. F. Invariants of the velocity-gradient, rate-of-strain, and rate-of-rotation tensors across the turbulent/nonturbulent interface in jets[J]. *Physics of Fluids*, **2008**, 20(5): 055101.
- [11] KIM J. and MOIN P. Application of a fractional-step method to incompressible Navier–Stokes equations[J]. *Journal of Computational Physics*, **1985**, 59: 308-323.
- [12] LE H. and MOIN P. An improvement of fractional step methods for the incompressible Navier–Stokes equations[J]. *Journal of Computational Physics*, **1991**, 92: 369-379.
- [13] RAUWOENS P., VIERENDEELS J. and MERCI B. A solution for the odd-even decoupling problem in pressure-correction algorithms for variable density flows[J]. *Journal of Computational Physics*, **2007**, 227: 79-99.
- [14] MORINISHI Y., LUND T. S., VASILYEV O. V. and MOIN P. Fully conservative higher order finite difference schemes for incompressible flow[J]. *Journal of Computational Physics*, **1998**, 143: 90-124.
- [15] NOCEDAL J. and WRIGHT S. J. *Numerical Optimization*[M]. New York, the USA: Springer, **2006**: 101-134.
- [16] FUNG Y. C. *Biomechanics – Motion, flow, stress and growth*[M]. New York, the USA: Springer, **1990**: 569-570.
- [17] FRIEHE C. A., VANATTA C. W. and GIBSON C. H. Jet turbulence: Dissipation rate measurements and correlations[C]. ANARD Conference Proceedings No.93 on Turbulent Shear Flows. London, U.K., **1971**: 18(1-7).
- [18] DEO R. C., MI Jian-chun and NATHAN G. J. The influence of Reynolds number on a plane jet[J]. *Physics of Fluids*, **2008**, 20(7): 075108.
- [19] DAI Y., KOBAYASHI T. and TANIGUCHI N. Large eddy simulation of plane turbulent jet flow using a new outflow velocity boundary condition[J]. *JSME International Journal. Series B, Fluids and Thermal Engineering*, **1994**, 37(2): 242-253.

[J]: *Journal Article*

[M]: *Monograph*

[C]: *Conference Proceeding*

## Chapter 3

### INFLUENCE OF EXIT REYNOLDS NUMBER[1][2]

In plane jet, inertial force and viscous force are the most important two forces to govern the flow evolution and mechanical characteristics, which makes it quite clear that the value of Reynolds number ( $Re$ ), defined as the ratio of inertial force to viscous force, will remarkably affect the behavior of plane jet. In this chapter, after the review of past studies, I will mainly explore the effects of exit  $Re$  on the development of plane jet in terms of the instantaneous and statistical information of the velocity and scalar fields, obtained by the DNS.

#### 3.1 Introduction

Studies on the effects of  $Re$  on plane jet, i.e., the  $Re$ -dependency of plane jet, were triggered by the study of Heskestad[3], in which he measured the centerline development of turbulent intensity with varying exit  $Re$  from 4,700 to 36,900. However, in this study the provided data and analysis were mainly focused on the flow characteristics in the far field region. In the work of Gutmark and Wygnanski[4], based on the combination of the experimental data from Bradbury[5], Heskestad[3], Knystautas[6], Van der Hegge Zijnen[7] and their own work, the  $Re$ -dependency of plane jet was assessed in view of mean velocities, turbulence intensities and third- and fourth-order terms, as well as two-point correlations and intermittency factor. However, all of the exit  $Re$  used in these experiments were larger than 10,000, in this case, the information was clearly not enough to capture the significant effects of the exit  $Re$  on the plane jet especially with moderate  $Re$ ; meanwhile, the experimental conditions were different between these experiments, which made the conclusions in the work of Gutmark and Wygnanski doubtful, because the exit  $Re$  needs to be the only varying factor when the  $Re$ -dependency of plane jet is assessed. Namar and

Ötügen[8] performed the study on the effect of moderate  $Re$ , varying from 1,000 to 7,000, on flow structure in both the near and far fields, but the nozzle used in their experiments had no face plates which made the jet entrains ambient fluid freely both axially and laterally, different from a strictly free plane jet. In 2003, Klein et al.[9] published their DNS work on the  $Re$ -dependency of plane jet, in the mean and turbulent properties of plane jet were analyzed with the exit  $Re$  possessing the value from 1,000 to 6,000. This work illustrated the advantages of DNS on the study of plane jets with moderate  $Re$ , but the data was only provided up to an axial distance  $x/d \leq 20$  because of the constraint of computing resource. A systematical study on  $Re$ -dependency of plane jet was carried out by Deo et al.[10], in their work the effect of exit  $Re$  on the mean and turbulent fields of plane jet were investigated with  $1,500 \leq Re \leq 16,500$ , it showed that the  $Re$ -dependency is substantial for the plane jet with  $Re \leq 10,000$  and becomes weak accompanying the increase of  $Re$ .

Up to now, substantial experimental works have been done to investigate the influence of exit  $Re$  on the evolution of plane jet, but the numerical work was still quite insufficient, which is quite suitable for the study on the influence of exit  $Re$  on the plane jet especially in the near field or with moderate  $Re$ . In order to further clarify the characteristics of the plane jet with different exit  $Re$ , in this chapter, the  $Re$ -dependency of plane jet in the whole flow development region is investigated based on the data from the DNSs.

### 3.2 Instantaneous Results

The characteristics of the instantaneous flow field in the plane jet with different exit  $Re$  are analyzed in this section. In the present simulation one time step is equal to  $0.02 d/U_b$ , where  $d$  is the height of jet exit and  $U_b$  is the exit mean bulk velocity, and the instantaneous parameters were captured at the 20,000<sup>th</sup> time step.

#### 3.2.1 Velocity and Pressure

Figures 3.1 (Left) and 3.1 (Right) show the contours of the instantaneous dimensionless streamwise velocity and pressure in the  $x$ - $y$  plane at the location  $z = 0$ , respectively.

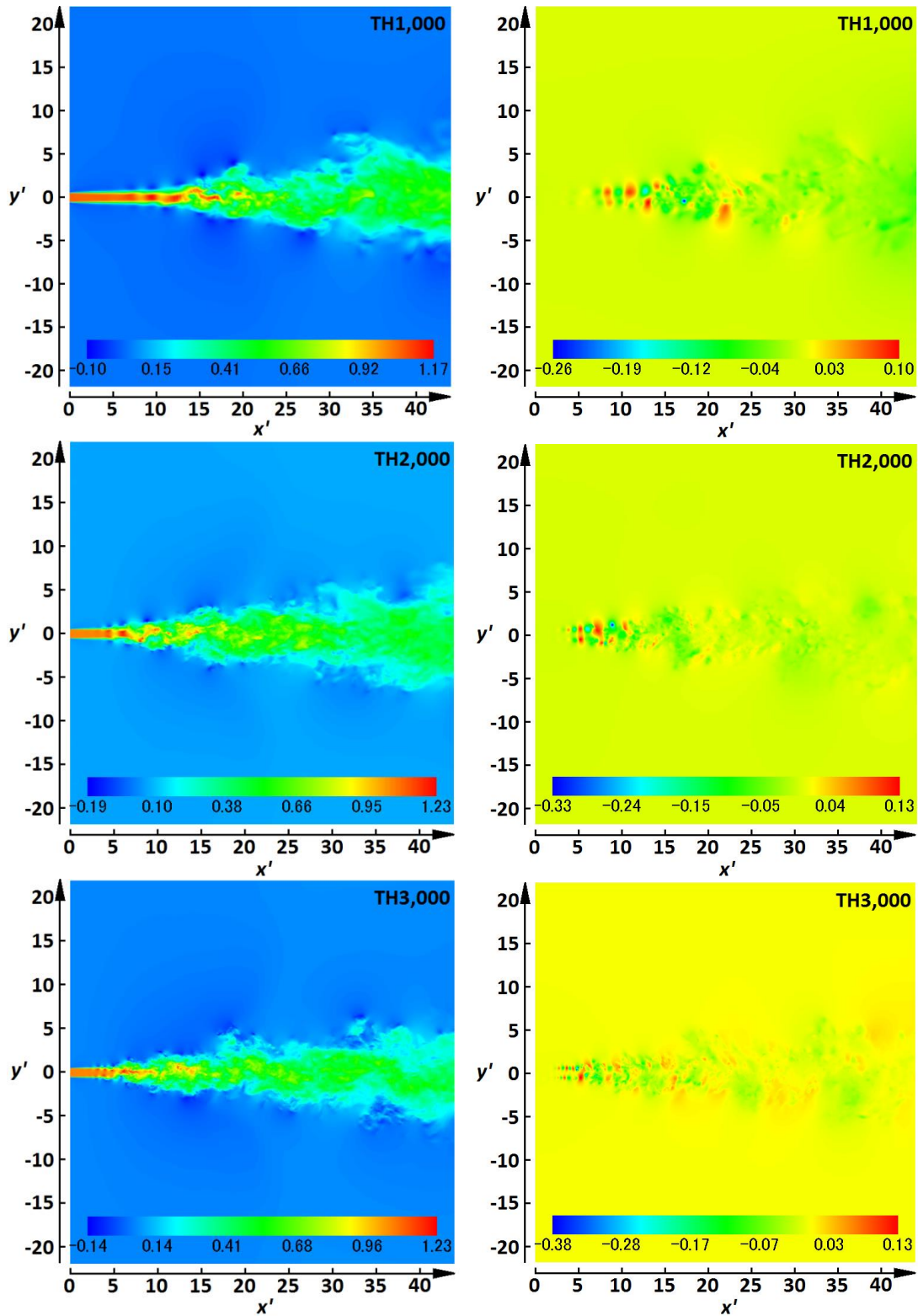


Figure 3.1 Instantaneous streamwise velocity (Left) and pressure (Right) fields. TH1,000, TH2,000, and TH3,000 represent the cases with top hat profile at  $Re = 1,000$ , top hat profile at  $Re = 2,000$ , and top hat profile at  $Re = 3,000$ , respectively.



In Figure 3.1 (left), the zone with a undiminished streamwise velocity behind the jet exit, equal to  $1.0U_b$ , marks the existence of the potential core, in which the jet develops in the laminar state. Due to the velocity difference across the interface between the ambient fluid and the jet, the Kelvin–Helmholtz instability occurs just behind the jet exit, which triggers the jet transition. Following the end of the potential core, I can capture the occurrence of the decay of the streamwise velocity at the jet centerline, and these figures show that the initial part of this decay is quite severe while the downstream decay is much more moderate. Meanwhile, the jet grows in the lateral direction with the entrainment of the ambient fluid and the effects of small-scale mixing in the downstream region reduce the presence of patches of the main flow and ambient flow. In Figure 3.1 (right), near the jet exit there is no pressure difference in the jet or between the ambient fluid and the jet; afterwards, along the jet centerline some symmetric pressure cores can be observed, which are followed by some anti-symmetric pressure cores, where only those anti-symmetric pressure cores will produce the acceleration of the jet and boost the convection in the lateral direction. Meanwhile, the positive and negative pressure core alternately occurs, that causes the acceleration of the jet and advances the convection in the streamwise direction. The pressure cores near the interface between the ambient fluid and the jet are positive for the entrainment. In the downstream region, the pressure differences in the jet or between the ambient fluid and the jet still exist but the values are obviously smaller than those in the upstream region.

The most obvious influence of exit  $Re$  on the instantaneous velocity field is that the increase of  $Re$  advances the transition of the plane jet; meanwhile, the influence on the instantaneous pressure field is shown by the smaller size of the pressure cores with larger  $Re$  in the upstream region.

### 3.2.2 Scalar and Its Gradient

Figure 3.2 shows the contours of instantaneous dimensionless scalar. The evolution of the scalar field presents some similar features to that of the streamwise velocity. A region, similar to the potential core in the velocity field, exists behind the jet exit, in which the scalar possesses a constant value, which is 1.0. It shows the scalar mixing and transport are remarkable in the flow development region and the jet

seems homogenous in the fully developed region. Moreover, the increase of the exit Re also advances the development of the scalar field.

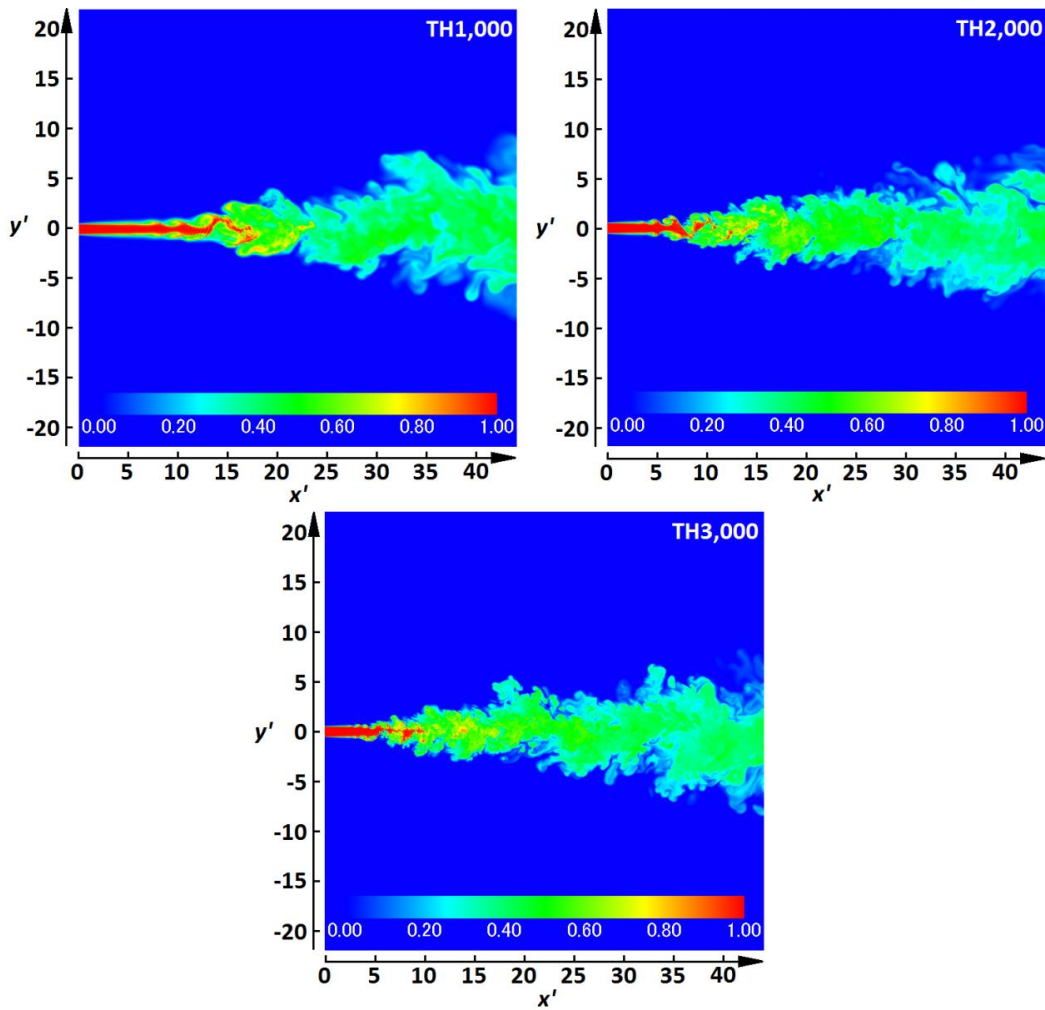


Figure 3.2 Instantaneous scalar field. TH1,000, TH2,000, and TH3,000 represent the cases with top hat profile at  $Re = 1,000$ , top hat profile at  $Re = 2,000$ , and top hat profile at  $Re = 3,000$ , respectively.

The performance of scalar gradient is important to the scalar transport, which is a vector in a three dimensional flow field. The scalar transport equation shown in Section 2.2, which is

$$\frac{\partial \tilde{\theta}'}{\partial t'} + \tilde{u}'_j \frac{\partial \tilde{\theta}'}{\partial x'_j} = \frac{1}{PrRe} \frac{\partial^2 \tilde{\theta}'}{\partial x'_j \partial x'_j}, \quad (3.1)$$

where from left to right the terms are the temporal derivative, representing the inertia of the system, the convection term, representing the convective transport by the velocity field, and the diffusion term, representing the gradient transport. This

equation shows the scalar gradient plays an important factor in the scalar transport.

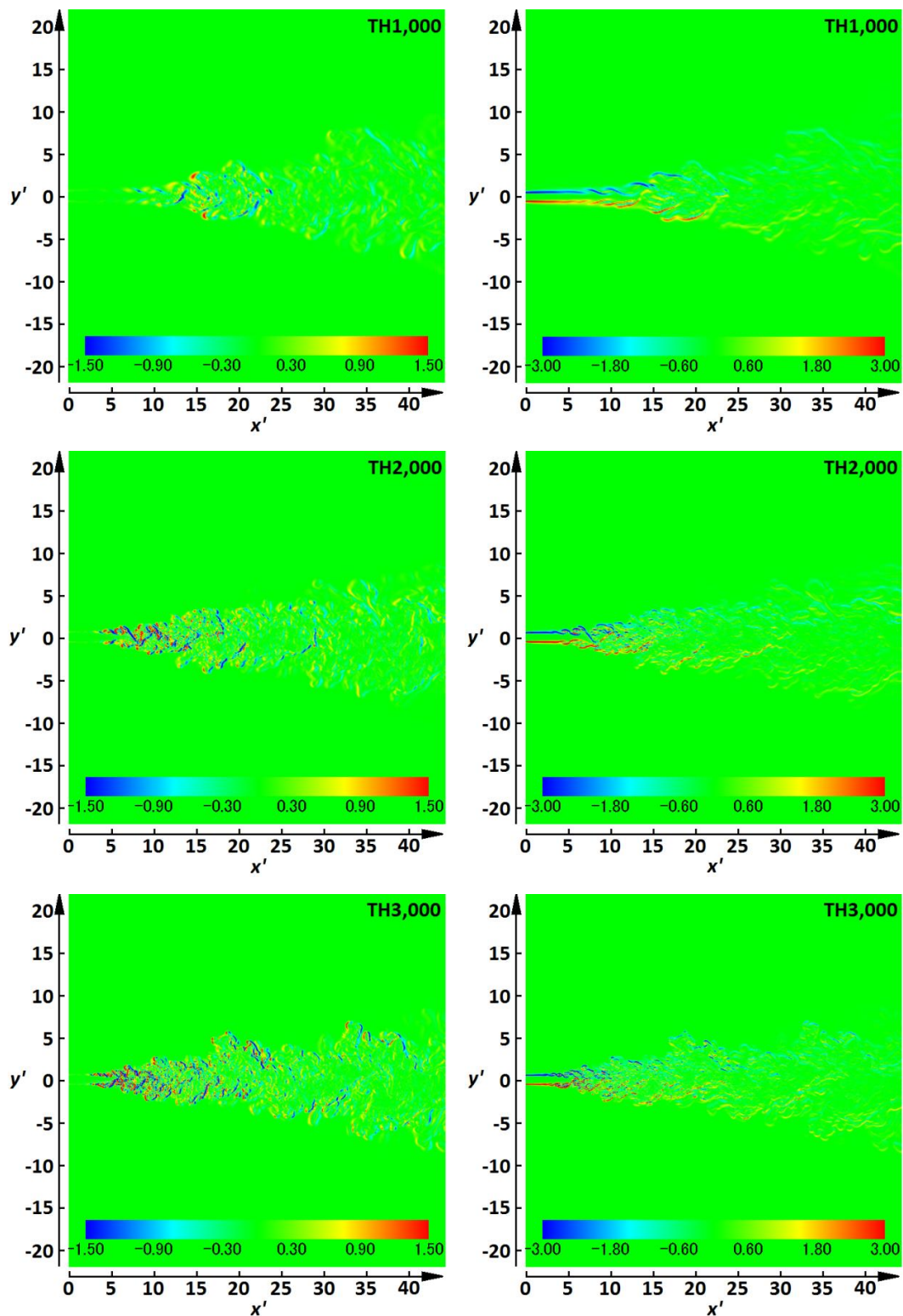


Figure 3.3 Instantaneous scalar gradient magnitude field. TH1,000, TH2,000, and TH3,000 represent the cases with top hat profile at  $Re = 1,000$ , top hat profile at  $Re = 2,000$ , and top hat profile at  $Re = 3,000$ , respectively.

In the plane jet, I focus on the scalar gradient magnitudes in the streamwise and lateral directions, and the contours of them are shown by the Figures 3.3 (left) and 3.3 (right), respectively.

Based on the contours of the scalar gradient shown by Figure 3.3, it is observed that in the potential core, both the streamwise and lateral scalar gradients are zero; the largest scalar gradients are in the interaction region; when the plane jet is fully developed, the scalar gradient will possess much smaller value. It is obvious that the larger scalar gradients in each region are located near the interface between the ambient fluid and the jet, which implies the importance of the flow dynamics near the interface to the development of plane jet.

When the plane jets are with different exit  $Re$ , it shows the scalar gradient possesses more large values and is more chaotic as the exit  $Re$  is increased.

### 3.3 Statistical Results

In this section, the statistical results about the velocity and scalar fields are presented and analyzed, which were calculated by averaging in time, based on the data from 20,000 time steps, as well as across the homogenous spanwise direction.

#### 3.3.1 Statistics along Jet Centerline

In this section, I investigate the evolution of the velocity and scalar along the jet centerline. First, the evolution of the mean streamwise velocity and mean scalar along the jet centerline is shown by Figure 3.4, where  $U_c$ ,  $\Theta_c$ ,  $U_j$ , and  $\Theta_j$  denote the mean streamwise velocity, mean scalar, mean exit streamwise velocity, and mean exit scalar at the jet centerline, respectively. In addition, the evolution of the turbulence intensity along the jet centerline is presented by Figure 3.5, where the subscript “*rmsc*” denotes the root-mean-square value of the variable at the jet centerline.

Figures 3.4 and 3.5 show that, the decay of the mean velocity with high  $Re$  occurs earlier than that with low  $Re$ , which can be attributed to the fast lateral development of two initial shear layers corresponding to high  $Re$ , consequently, the length of the potential core is shorter in the case with high  $Re$ . Based on the mean scalar profile, the length of the potential core is defined as the distance from the jet exit to the location at which  $\Theta_c = 0.99\Theta_j$ . Following the above definition, the potential core lengths for

these three  $Re$  are:  $5.1d$  for  $Re = 3,000$ ,  $6.1d$  for  $Re = 2,000$ ,  $10.1d$  for  $Re = 1,000$ , as shown in Figure 3.4 (Right).

Behind the potential core, the results show that the decay of the mean streamwise velocity and mean scalar is faster in the case with low  $Re$ . Moreover, the increase of the turbulence intensity is relatively sharper with low  $Re$ , where the higher  $Re$  no longer corresponds to the higher turbulence intensity.

Moreover, these above differences in the evolution of the mean and turbulent statistics become quite small further downstream, which imply that the  $Re$  dependency of the plane jet is weak in the far field region compared to that in the near field region.

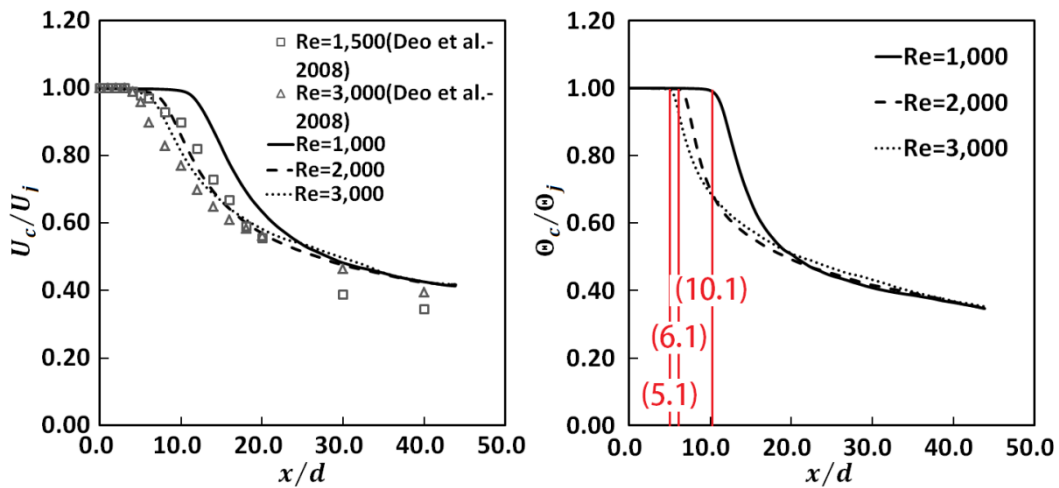


Figure 3.4 Evolution of mean variables along the jet centerline. (Left) Mean streamwise velocity, where the experimental data is from Deo et al.[10]; (Right) mean scalar.

The experimental data from Deo et al.[10] were used to verify the present simulation results. In their experiments, the jet developed in a stagnant environment, the profile of the mean streamwise velocity at the jet exit was a top-hat, and the fluctuation intensity at the jet exit was measured to be 1% of the mean flow. These same parameters were used in the present simulations. The results of Figures 3.4 and 3.5 show that for the flow evolution behind the potential core, there is good agreement between the experimental data of Deo et al. and the present simulations. However, a longer potential core and a smaller turbulent streamwise velocity can be observed in the present simulations. This can be attributed to the existence of a weak

co-flow around the jet in the simulation, because it has been illustrated that the presence of a co-flow can slow the development of the jet to a self-similar state in Everitt and Robins[11] and LaRue et al.[12].

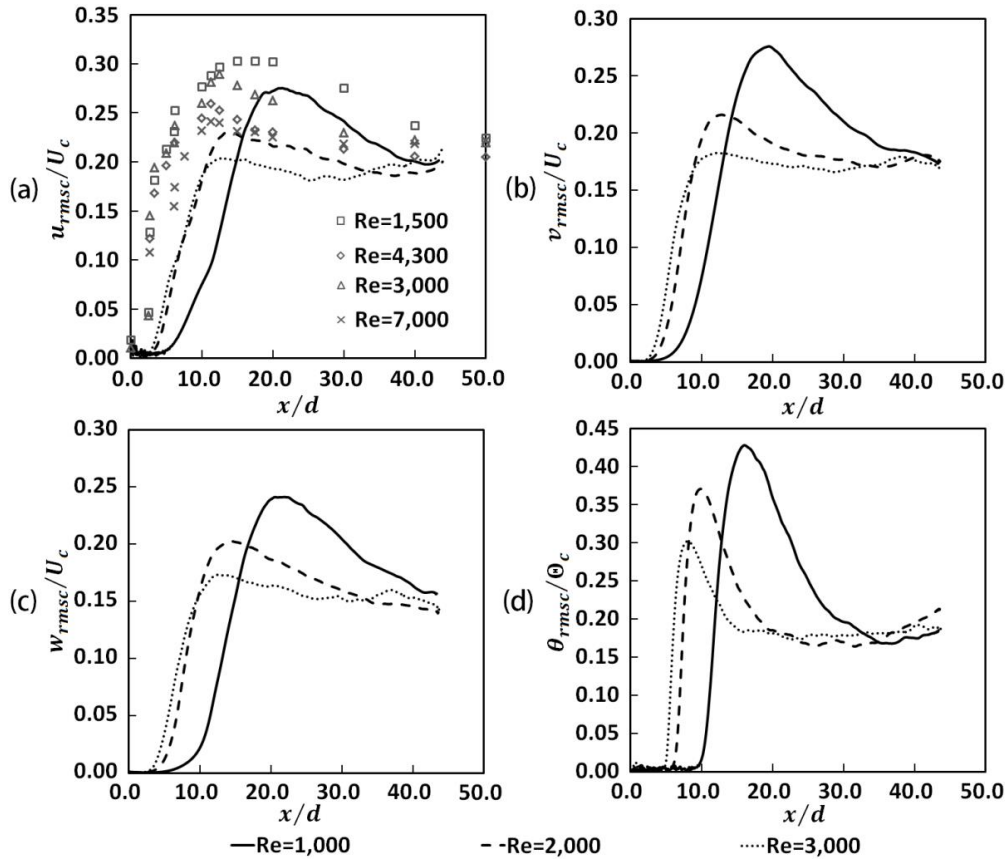


Figure 3.5 Evolution of turbulent variables along the jet centerline. (a) Turbulent streamwise velocity, where the experimental data is from Deo et al.[10]; (b) turbulent lateral velocity; (c) turbulent spanwise velocity; (d) turbulent scalar.

For all conditions in the present study, only in the condition with  $Re = 3,000$ , the plane jet achieved a fine self-similarity in the downstream region of the flow, which is characterized by the constant turbulence intensity at the jet centerline.

Moreover, based on the results in Figures 3.4 and 3.5, the mean and turbulent scalar at the jet centerline present a similar value for these three conditions sooner than the counterparts in the velocity field, which implies the transition of the scalar field is faster than the velocity field.

### 3.3.2 Lateral Evolution of Plane Jet

#### 3.3.2.1 Self-similarity

In this section, the lateral profiles of velocity and scalar are presented to investigate the influence of the exit  $Re$  on the characteristics of the self-similarity of plane jets. Considering that the case with  $Re = 1,000$  has not attained the self-similarity, as shown in Figure 3.5, only the data from the cases with  $Re = 2,000$  and  $Re = 3,000$  are used to discuss this topic.

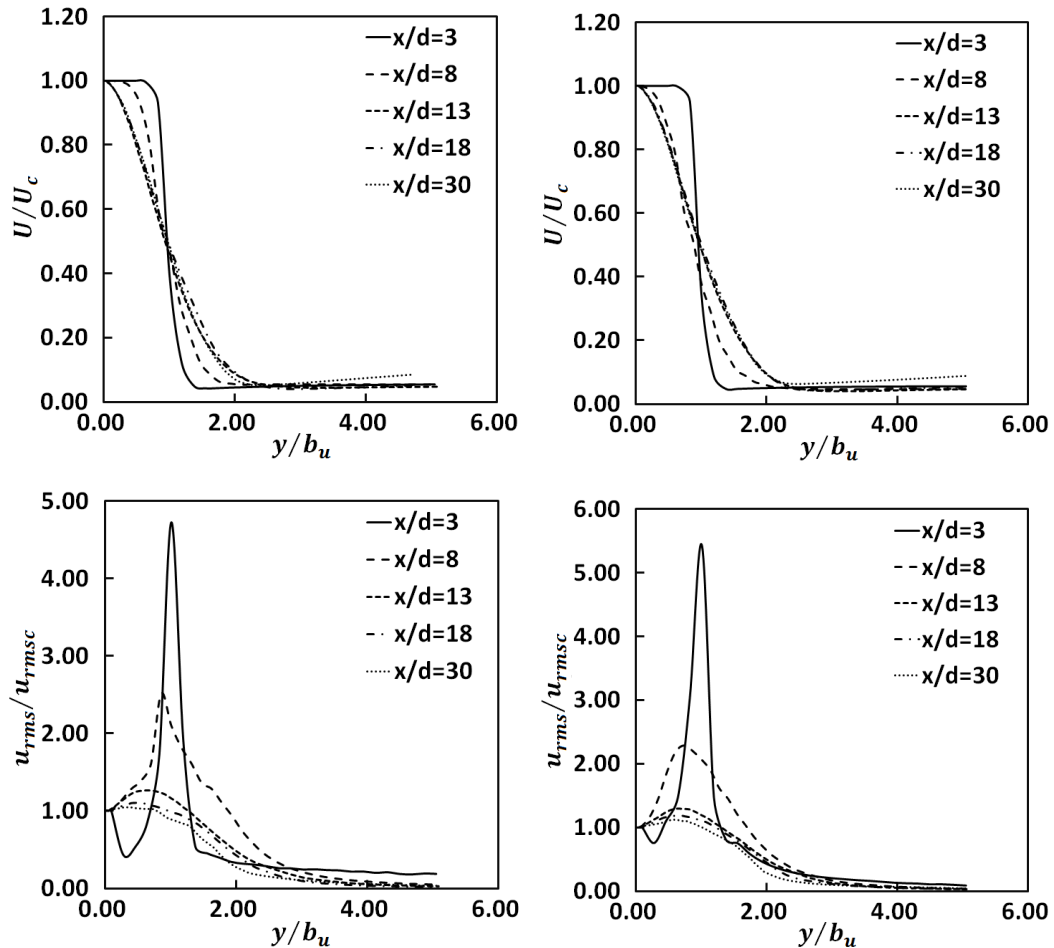


Figure 3.6 Lateral profiles of mean and turbulent streamwise velocities. (Left) The case with  $Re = 2,000$ ; (Right) the case with  $Re = 3,000$ .

The lateral profiles of the mean and turbulent streamwise velocities are plotted in Figure 3.6, respectively, at five different locations in order to study the self-similar behavior of the related parameters, and they are as usual normalized with the local centerline mean streamwise velocity ( $U_c$ ), the local centerline turbulent streamwise velocity ( $u_{rmsc}$ ), and the half-width of the mean velocity profile ( $b_u$ ).

Based on the results shown in Figure 3.6, it is observed that the increase of Reynolds number will be helpful for the attainment of self-similarity. And the

self-similarity of mean velocity is achieved at the nearer upstream location than that of the turbulent velocity especially for the case with low Re. This can be attributed to the slower approach toward isotropic turbulent state for low Re jet flows, which verifies the self-similarity is one kind of feature related to the fully developed flows.

In addition, in Figure 3.6 the slight increase of mean velocity at the location  $x/d = 30$  outside the jet can be attributed to the effects of lateral boundary, which can't be ignored as the jet laterally grows somewhat along the streamwise direction. The artificial fluctuation profile at the jet exit, described in Section 2.7.1, cause a local minimum peak occurs inside the jet but not at the jet centerline, which is not one natural result. But it should be mentioned here the artificial fluctuation profile will be necessary for boosting the turbulence development of the flow in the simulation.

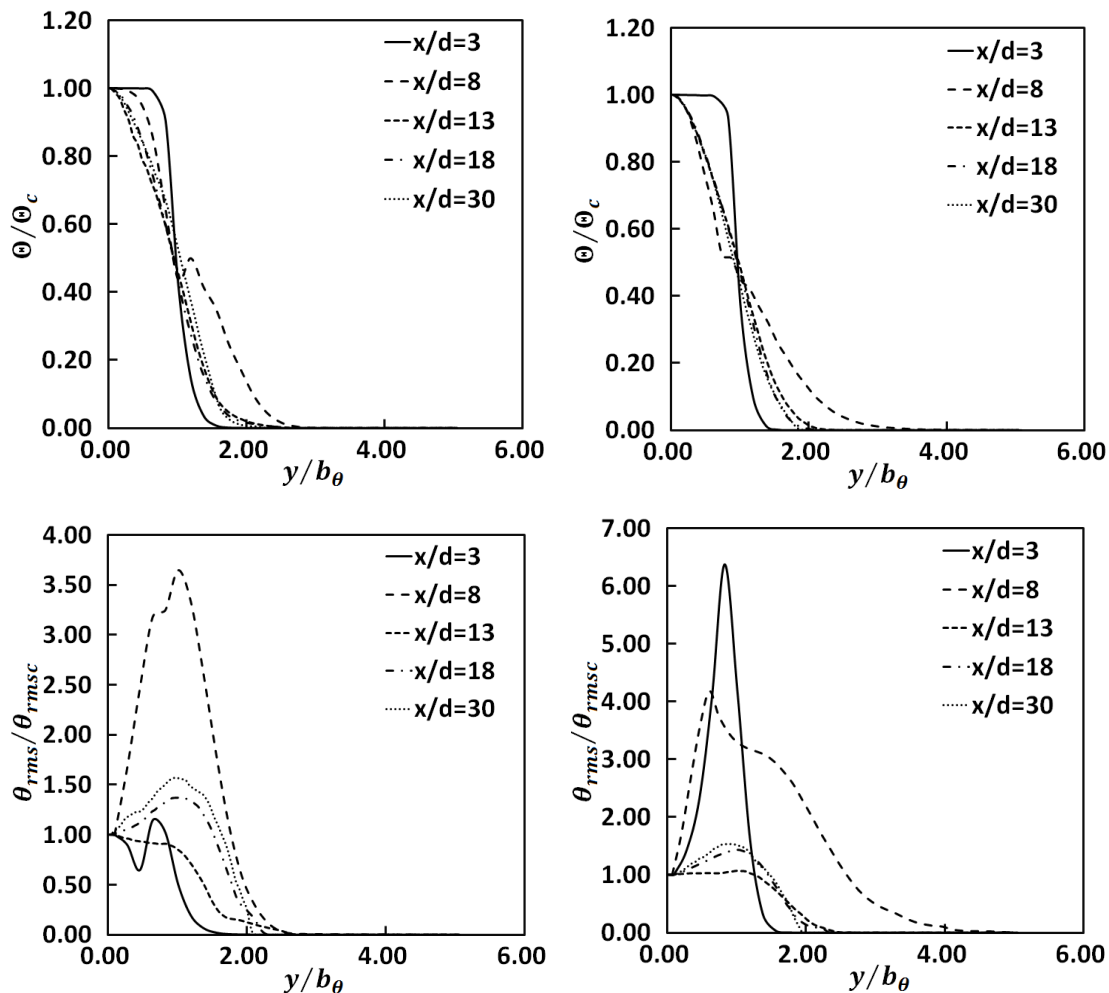


Figure 3.7 Lateral profiles of mean and turbulent scalars. (Left) The case with  $Re = 2,000$ ; (Right) the case with  $Re = 3,000$ .



Figure 3.7 is used to show the lateral evolution of the mean and turbulent scalars at those same five locations as in Figure 3.6. The local centerline mean scalar ( $\theta_c$ ), the local centerline turbulent scalar ( $\theta_{rmsc}$ ), and the half-width of the mean scalar profile ( $b_\theta$ ) are used to normalize the parameters. Likewise, the high Reynolds number will help the plane jet to achieve the self-similarity, which is similar to the results about the velocity field.

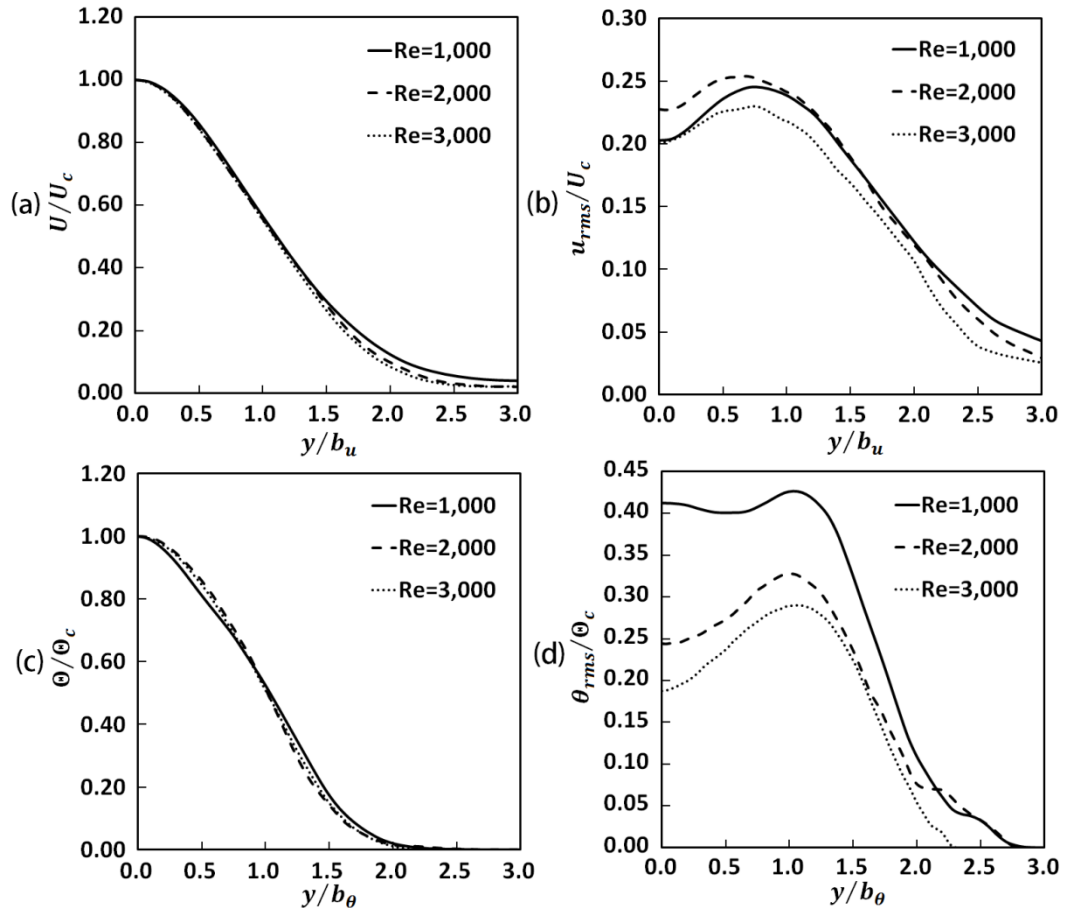


Figure 3.8 Lateral profile of variables at  $x/d = 15.0$ . (a) Mean streamwise velocity; (b) turbulent streamwise velocity; (c) mean scalar; (d) turbulent scalar.

In Figures 3.6 and 3.7, the results of turbulent profiles show that at the positions of  $x/d = 3$  and  $x/d = 8$ , which are close to the jet exit, remarkable fluctuation can be observed. The dramatic turbulent fluctuation in the scalar field even cause the unusual varying at the location  $x/d = 8$  for the lateral evolution of the mean scalar in the case with  $Re = 2,000$ . The largest peak of turbulent scalar for  $Re = 2,000$  is obtained at  $x/d = 8$  not  $x/d = 3$ , because the turbulence development in these

cases is slower than the case with lower  $Re$ , meanwhile, it can be seen that for  $Re = 3,000$  the largest peak occurs at  $x/d = 3$ .

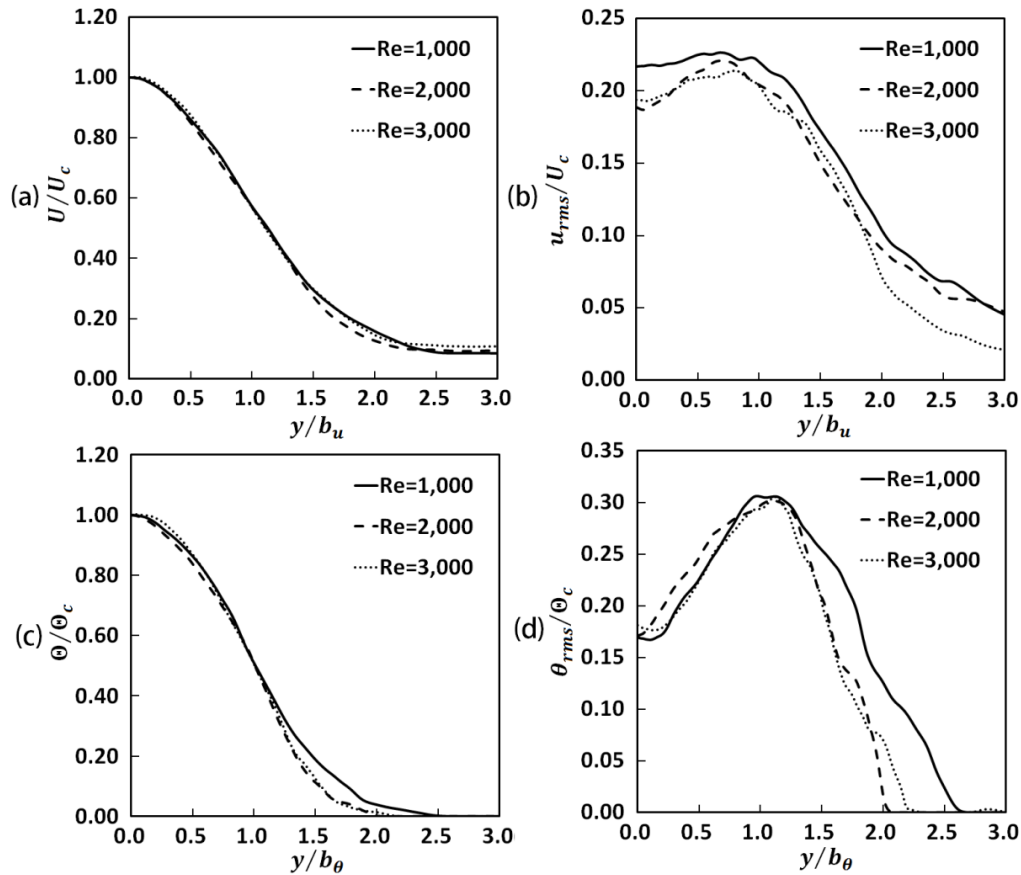


Figure 3.9 Lateral profile of variables at  $x/d = 35.0$ . (a) Mean streamwise velocity; (b) turbulent streamwise velocity; (c) mean scalar; (d) turbulent scalar.

### 3.3.2.2 Evaluation of Lateral Profiles

In this section, two streamwise locations,  $x/d = 15.0$  and  $x/d = 35.0$ , are selected to evaluate the lateral evolution of the plane jet and compare the characteristics of the plane jet with different exit  $Re$ . The lateral coordinate  $y$  is normalized by  $b_u$  (the half jet width for the mean velocity field), and  $b_\theta$  (the half jet width for the mean scalar field).

Figures 3.8 and 3.9 show the lateral profiles of the streamwise velocity and scalar. At  $x/d = 15.0$ , the mean profiles with these three  $Re$  are almost coincident, however the turbulent profiles do not coincide properly, even at  $x/d = 35.0$ . The above observation shows that the influence of the Reynolds number on the turbulent flow field is more obvious again. The lateral evolutions of the variables at  $x/d = 35.0$  are

more similar, which also verifies the weak Reynolds number dependency of the plane jet in the downstream flow region.

Figures 3.10(a) and 3.11(a) show the lateral profiles of Reynolds stress, and the lateral profiles of turbulent scalar fluxes are shown in Figures 3.10(b), 3.10(c), 3.11(b), and 3.11(c), in which the symbol  $\langle \quad \rangle$  denotes the statistics calculated by averaging in time, based on the data from 20,000 time steps, as well as across the homogenous spanwise direction. The results show that, with the decrease of Reynolds number, the value of these statistics increase especially at  $x/d = 15.0$ , which is located in the interaction region of the plane jet. Further, the Re-dependency observed at  $x/d = 35.0$  is weaker than that at  $x/d = 15.0$ , which confirms the weak Re-dependency in the downstream region of the plane jet again.

Furthermore, the peak values of all three variables occur at the location near the half width of the plane jet, which suggests that the net transport of momentum and scalar are stronger at this location[13].

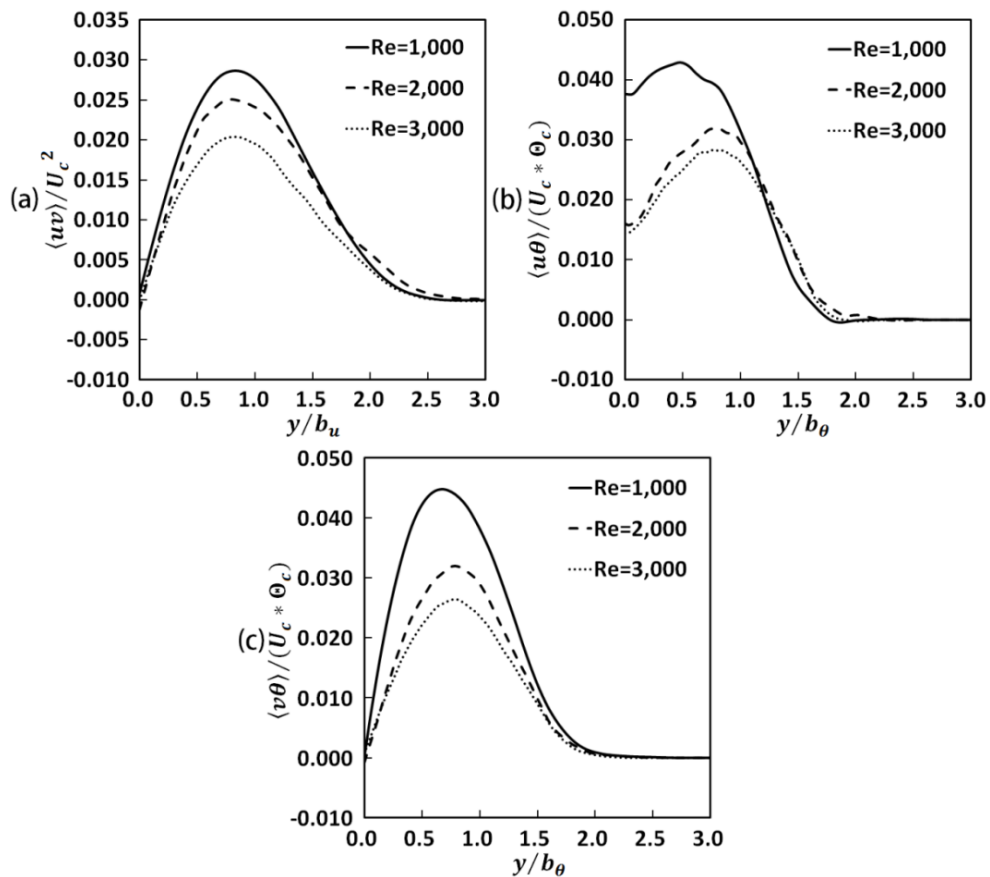


Figure 3.10 Lateral profile of variables at  $x/d = 15.0$ . (a) Reynolds stress; (b) streamwise turbulent scalar flux; (c) lateral turbulent scalar flux.

Figures 3.12 and 3.13 present the lateral evolution of convection terms, i.e., the streamwise convection term,  $\Gamma_{u1} = U(\partial U/\partial x)$ , and the lateral convection term,  $\Gamma_{u2} = V(\partial U/\partial y)$ , and the turbulent transport terms, i.e., the lateral turbulent transport term,  $\Gamma_{u3} = \partial\langle uv\rangle/\partial y$ , and the streamwise turbulent transport term,  $\Gamma_{u4} = \partial\langle u^2\rangle/\partial x$ , embodied in the mean streamwise momentum transport equation, which are non-dimensionalized by  $U_c^2/d$ .

The mean streamwise momentum transport equation for the plane jet in two dimensions is as follows,

$$U \frac{\partial U}{\partial x} + V \frac{\partial U}{\partial y} + \frac{\partial\langle u^2\rangle}{\partial x} + \frac{\partial\langle uv\rangle}{\partial y} = -\frac{1}{\rho} \frac{\partial P}{\partial x} + 2\nu \left( \frac{\partial S_{xx}}{\partial x} + \frac{\partial S_{xy}}{\partial y} \right) \quad (3.2)$$

where  $x$  is the streamwise coordinate,  $y$  is the lateral coordinate,  $U$  is the mean streamwise velocity,  $V$  is the mean lateral velocity,  $u$  is the turbulent streamwise velocity,  $v$  is the turbulent lateral velocity,  $P$  is the mean pressure,  $S_{xx}$  and  $S_{xy}$  are the streamwise components of the mean strain rate, and  $\rho$  is the fluid density.

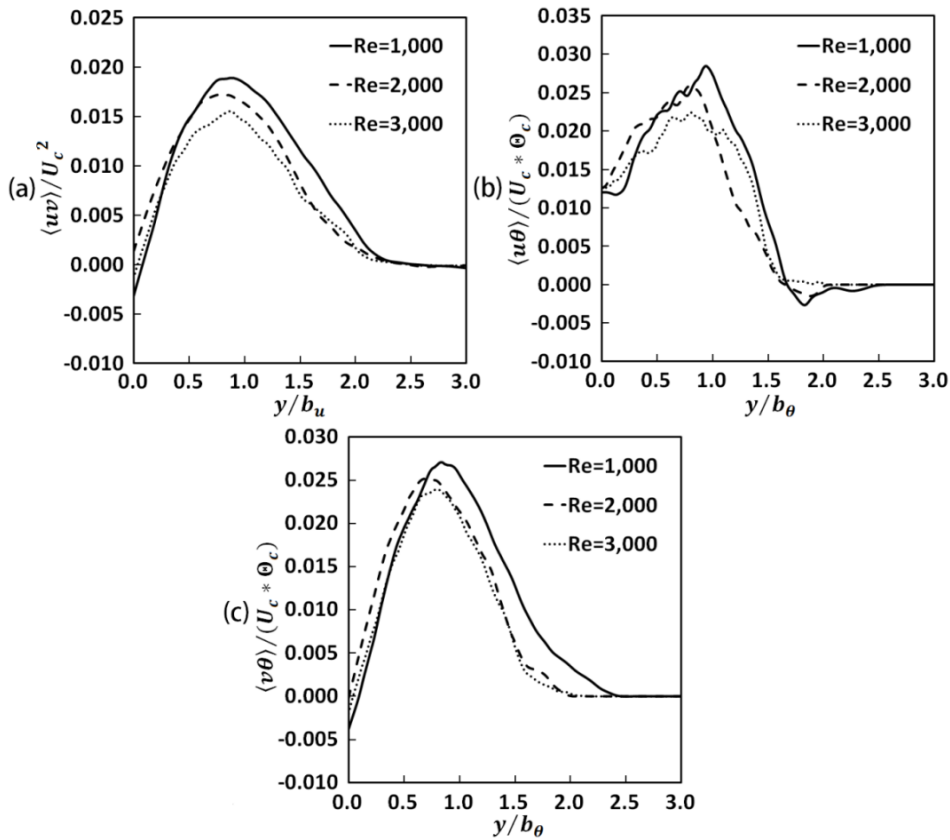


Figure 3.11 Lateral profile of variables at  $x/d = 35.0$ . (a) Reynolds stress; (b) streamwise turbulent scalar flux; (c) lateral turbulent scalar flux.

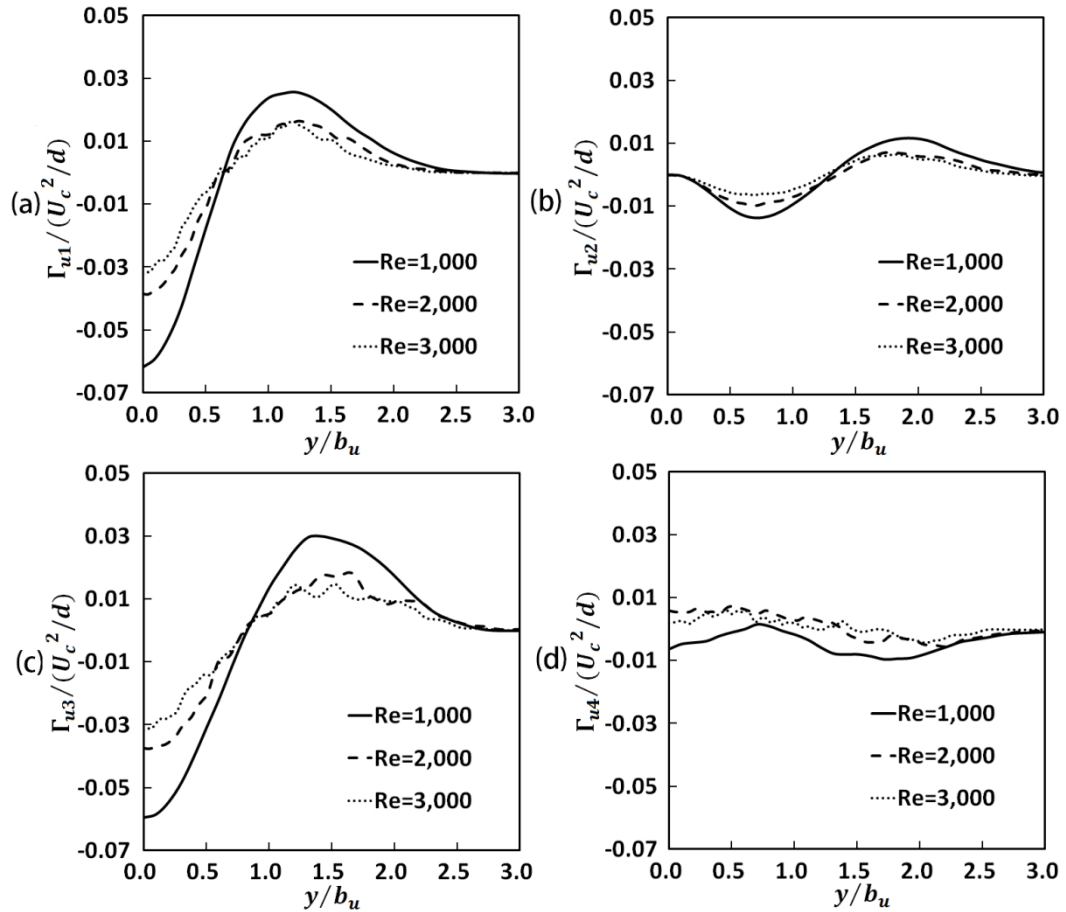


Figure 3.12 Lateral profile of the mean streamwise momentum transport at  $x/d = 15.0$ . (a) Streamwise convection term; (b) lateral convection term; (c) lateral turbulent transport term; (d) streamwise turbulent transport term.

The results show that streamwise convection and lateral turbulent transport dominate in the mean streamwise momentum transport. Additionally, these two terms have negative peak values at the jet centerline, which corresponds to the largest loss of momentum. On the other hand, positive peaks appear at the location near the half width of the plane jet, which corresponds to the largest gain of momentum. The lateral convection presents the antisymmetric feature between the jet zone and the ambient flow zone, which is consistent with the antisymmetric feature of the mean lateral velocity[14], i.e., the fluid in the ambient flow zone is entrained into the jet, while the fluid near the jet centerline is brought into the zone near the interface between the jet and the ambient flow.

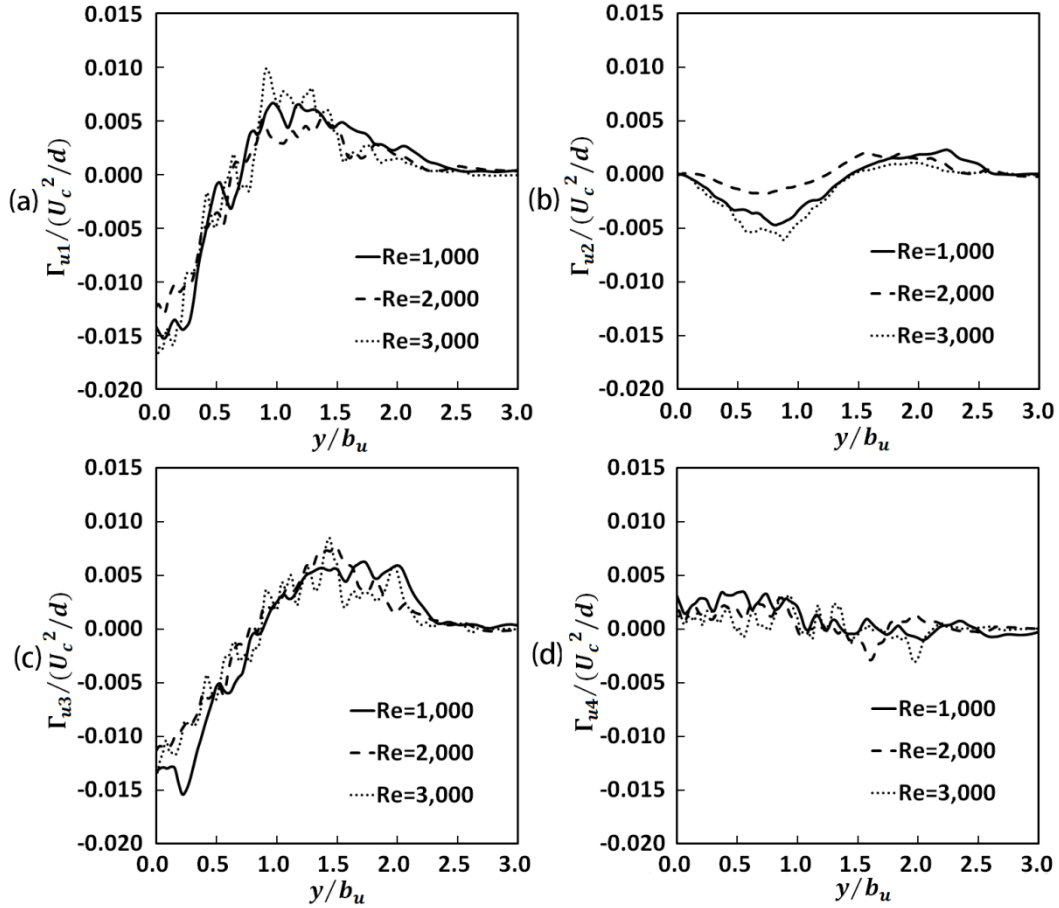


Figure 3.13 Lateral profile of the mean streamwise momentum transport at  $x/d = 35.0$ . (a) Streamwise convection term; (b) lateral convection term; (c) lateral turbulent transport term; (d) streamwise turbulent transport term.

At  $x/d = 15.0$ , when the Reynolds number decreases, the momentum transport is strengthened, due to the convection and turbulent transport. This increase in strength should be connected with the behavior of the larger scale coherent structure, which will be discussed in Chapter 5. Unsurprisingly, the Reynolds number dependency of the momentum transport also becomes weaker at  $x/d = 35.0$

I also calculated the lateral evolution of four terms in the mean scalar transport at the location  $x/d = 15.0$ , shown by Figure 3.14, which are the streamwise convection term,  $\Gamma_{\theta 1} = U(\partial\theta/\partial x)$ , the lateral convection term,  $\Gamma_{\theta 2} = V(\partial\theta/\partial y)$ , the lateral turbulent transport term,  $\Gamma_{\theta 3} = \partial\langle u\theta\rangle/\partial x$ , and the streamwise turbulent transport term,  $\Gamma_{\theta 4} = \partial\langle v\theta\rangle/\partial y$ , normalized by  $U_c\theta_c/d$ . The mean scalar transport equation for the plane jet in two dimensions is given as

$$U \frac{\partial \Theta}{\partial x} + V \frac{\partial \Theta}{\partial y} + \frac{\partial \langle u\theta \rangle}{\partial x} + \frac{\partial \langle v\theta \rangle}{\partial y} = \alpha \left( \frac{\partial^2 \Theta}{\partial x^2} + \frac{\partial^2 \Theta}{\partial y^2} \right) + S_{\Theta}, \quad (3.3)$$

where  $\Theta$  is the mean scalar,  $\theta$  is the turbulent scalar, and  $S_{\Theta}$  is the mean value of the source term. Compared with the momentum transport, similar features of the mean scalar transport can be observed.

Furthermore, it should be mentioned that the change from  $Re = 1,000$  to  $Re = 2,000$  produces more obvious effects on the flow lateral evolution, which means that the Reynolds number dependency of the plane jet is stronger for the conditions with a low Reynolds number. A similar conclusion was determined in the study of Deo et al.[10].

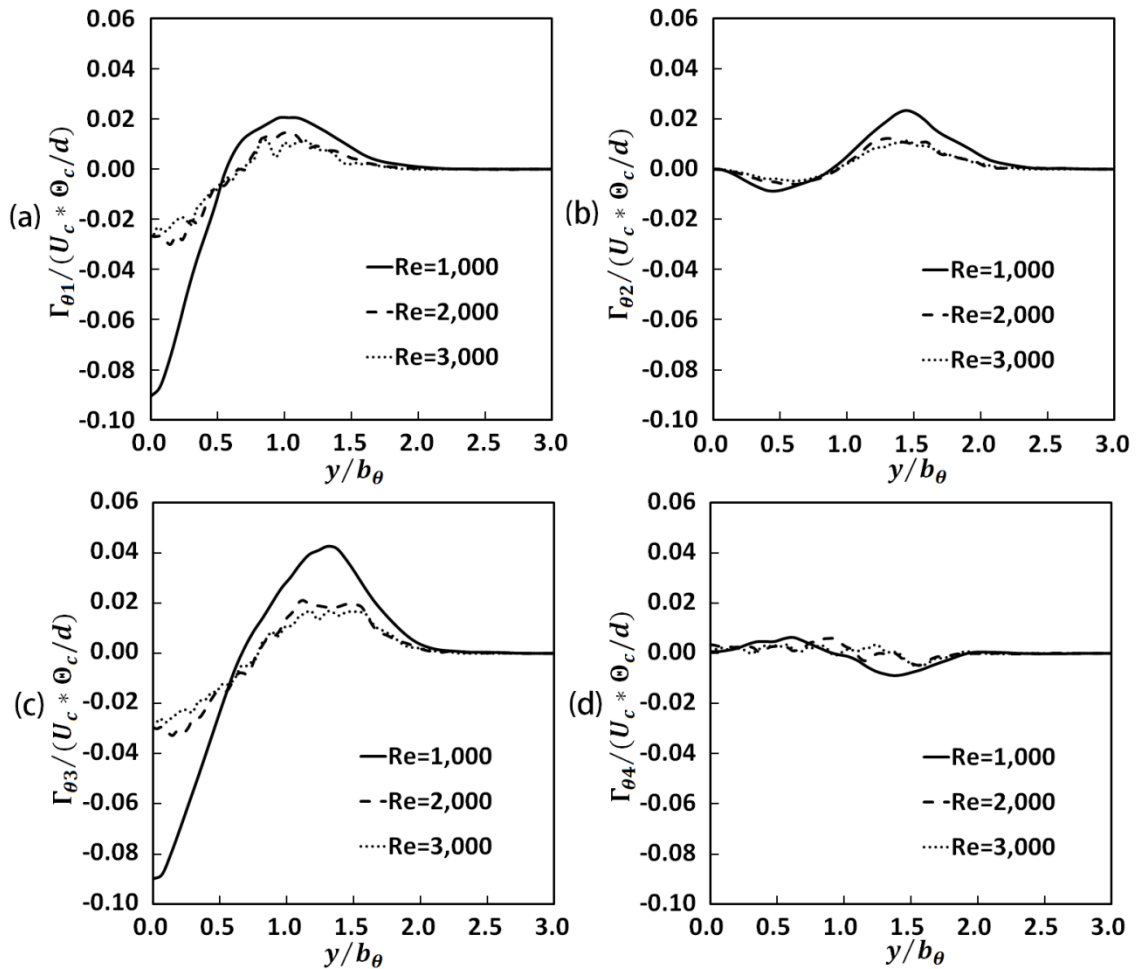


Figure 3.14 Lateral profile of the mean scalar transport at  $x/d = 15.0$ . (a) Streamwise convection term; (b) lateral convection term; (c) lateral turbulent transport term; (d) streamwise turbulent transport term.

### 3.4 Conclusion

In this chapter, the influence of exit  $Re$  on the plane jet was investigated based on the instantaneous and statistical results. The streamwise and lateral profile of mean and turbulent variables about the velocity and scalar were presented. The convection and turbulent transport in the transport process of the mean streamwise momentum and mean scalar were also studied.

Main results are summarized as follows:

1. The plane jet is the exit  $Re$ -dependent, which is especially obvious in the near field, but this dependency becomes weaker in the downstream region of the flow. As the exit  $Re$  increases, the length of the jet potential core becomes shorter and the flow transition is promoted; however, the larger turbulent variables are observed at the small exit  $Re$  in the flow development process.

2. The transition of the plane jet from the laminar state to the turbulent state is advanced by a large exit  $Re$ ; however, in the near field region behind the potential core, the mean streamwise momentum and mean scalar transport are strengthened by a small exit  $Re$ .

3. The streamwise convection and the lateral turbulent transport are dominant in the transport of the mean streamwise momentum and mean scalar.

4. The plane jet shows the stronger  $Re$  dependency in the condition with a small  $Re$ .

### References

- [1] WU N., SAKAI Y., NAGATA K., SUZUKI H., TERASHIMA O. and HAYASE T. Analysis of flow characteristics of turbulent plane jets based on velocity and scalar fields using DNS[J]. *Journal of Fluid Science and Technology*, **2013**, 8(3): 247-261.
- [2] WU N., SAKAI Y., NAGATA K., ITO Y., TERASHIMA O. and HAYASE T. Influence of Reynolds number on coherent structure, flow transition, and evolution of the plane jet[J]. *Journal of Fluid Science and Technology*, **2014**, 9(2): 14pages.
- [3] Heskestad G. Hot-wire measurements in a plane turbulent jet[J]. *Trans. Journal of Applied Mechanics*, **1965**, 32(4): 721-734.



- [4] Gutmark E. and Wygnanski I. The planar turbulent jet[J]. Journal of Fluid Mechanics, **1976**, 73(3): 465-495.
- [5] Bradbury L. J. S. The structure of a self-preserving turbulent plane jet[J]. Journal of Fluid Mechanics, **1965**, 23(1): 31-64.
- [6] Knystautas R. The turbulent jet from a series of holes in line[J]. Aeronaut. Q., **1964**, 15: 1-28.
- [7] Van Der Hegge Zijnen B. G. Measurements of the distribution of heat and matter in a plane turbulent jet of air[J]. Applied Scientific Research, Section A, **1958**, 7(4): 277-292.
- [8] Namer I. and Ötügen M. V. Velocity measurements in a plane turbulent air jet at moderate Reynolds numbers[J]. Experiments in Fluids, **1988**, 6(6): 387-399.
- [9] KLEIN M., SADIKI A. and JANICKA J. Investigation of the influence of the Reynolds number on a plane jet using direct numerical simulation[J]. International Journal of Heat and Fluid Flow, **2003**, 24(6): 785-794.
- [10] DEO R. C., MI Jian-chun and NATHAN G. J. The influence of Reynolds number on a plane jet[J]. Physics of Fluids, **2008**, 20(7): 075108.
- [11] EVERITT K. W. and ROBINS A. G. The development and structure of turbulent plane jets[J]. Journal of Fluid Mechanics, **1978**, 88(3): 563-583.
- [12] LARUE J. C., LY T., RAHAI H. and JAN P. Y. On similarity of a plane turbulent jet in a co-flowing stream[C]. Proceeding of the Eleventh Symposium on Turbulent Shear Flows, Grenoble, France, **1997**, 3: 25.11-25.16.
- [13] PRANDTL L. Uber die ausgebildete turbulenz[J]. Ztschr. f. angew. Math. und Mech., **1925**, 5: 136-138. (in German)
- [14] SUZUKI H., SAKAI Y., NAGATA K. and SUGIMOTO D. Direct numerical simulation on turbulence structures in a transition process of a spatially developing turbulent plane jet[C]. The 3<sup>rd</sup> International Conference on Jets, Wakes and Separated Flows, Cincinnati, USA, **2010**: 1-6.

[J]: Journal Article

[M]: Monograph

[C]: Conference Proceeding

## Chapter 4

### INFLUENCE OF MEAN EXIT VELOCITY PROFILE AND CROSS-IMPACT BETWEEN DIFFERENT INITIAL FACTORS[1][2][3]

The exit velocity profile of plane jet consists of the mean and turbulent components, which is the manifestation of the inflow and the structure design of the jet nozzle in the flow experiments or engineering applications. It is known that the exit velocity profile remarkably influences the evolution of plane jet in the near field region [4] and the far field region[5], i.e., the mean and turbulent flow fields in plane jet will present some varying features because of the differences of velocity distribution at the jet exit. In this chapter, I focus on the effects of mean exit velocity profile on the development of plane jet; meanwhile the cross-impact between two initial factors, i.e., the exit Reynolds number and the mean exit velocity profile, will be also noted.

#### 4.1 Introduction

Recalling the definition of the exit velocity profile in Chapter 1, the characteristics of the mean exit velocity profile in plane jet correspond to the different combinations of the inner-wall nozzle exit contraction profile and the aspect ratio of the rectangular nozzle in the experiments.

The previous studies on the influence of the inner-wall nozzle exit contraction profile on plane jet were unsealed by the work of Hussian and Clark[4], who experimentally investigated the characteristics of the velocity field with different initial boundary conditions in the near field of a plane jet, using a smoothly contoured quasi-plane nozzle. The results showed a laminar boundary layer induces a larger mass flux and an earlier development of turbulence intensity, and combined with their similar work on the axisymmetric free shear layer[6], they declared the strong

dependence on the initial boundary layer of the downstream mean and turbulent quantities in the plane jet. Goldschmidt and Bradshaw[7] studied the effects of nozzle exit turbulence intensity on the spreading rate of the free plane jets with a contoured plane nozzle, which showed the larger spreading rate is closely related to the higher exit turbulence intensity. In the study of Chambers et al.[8], two different sets of initial conditions at the beginning of the interaction region were experimented. One was a nearly top-hat velocity profile with laminar boundary layers generated by a smooth contraction nozzle, and the other was a nearly fully developed velocity profile generated by a smooth contraction nozzle followed by a long channel. In the case with the laminar boundary layer, it showed the mixing layer structures were highly organized and symmetric about the jet centerline, and large mixing rates occurred in the near field; meanwhile, in the case with the turbulent boundary layer, the structures were highly three-dimensional and asymmetric about the jet centerline. Deo et al.[9] conducted the experiments of the plane jets with the radially contoured nozzle, in which the exit radii of the nozzles varied, the results showed both the initial flow and the downstream flow are dependent upon the exit radii of the nozzle and the effect on the mean and turbulent field decreases as the exit radius increases.

On the other hand, the influence of the nozzle aspect ratio on plane jet was first studied by Van Der Hegge Zijnen[10], in his work the nozzle aspect ratio possessed two values (20 and 25). The results showed the jet attains a higher decay and its virtual origin moves upstream as the aspect ratio is increased. However, considering the difference between these two aspect ratios was small, the results were not persuasive enough. In the experiments of Bashir and Uberoi[11], the heated plane jets with three nozzle aspect ratios, 20, 40, and 144, were studied. The findings in their work were similar to the work of Van Der Hegge Zijnen[10]. Afterwards, by reviewing the previous experimental studies on plane jet, Gouldin et al.[12] suggested the nozzle aspect ratio has an impact on the self-similarity of the true plane jet. All of the above three references only focused on the self-similarity region of the plane jet. In the further study, Deo et al.[13] reported a more systematic study of the influence of the nozzle aspect ratio on plane jet, in which the characteristics of the plane jet in the near field were also investigated. One important conclusion in their work was that the plane jet can be independent on the nozzle aspect ratio even in the near field when the nozzle

aspect ratio is a quite large value.

The previous study on the influence of exit velocity profile were only conducted based on the experimental method, and most of the studied plane jets possessed a large exit Reynolds number, which motivated us to study the dependency on the exit velocity profile of the plane jet with moderate exit Reynolds number by means of direct numerical simulation (DNS). In addition, the periodic boundary condition, which is often chosen for approximating a large or infinite system by using a small part called a unit cell, is set at the spanwise boundary in DNS in order to omit the effects of the nozzle aspect ratio.

#### 4.2 Mean Exit Profiles at Jet Exit

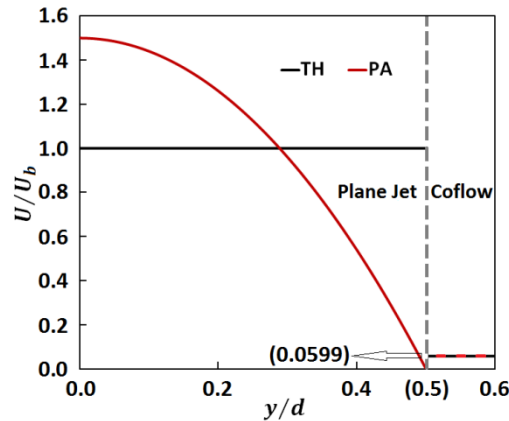


Figure 4.1 Mean streamwise velocity profiles at the jet exit

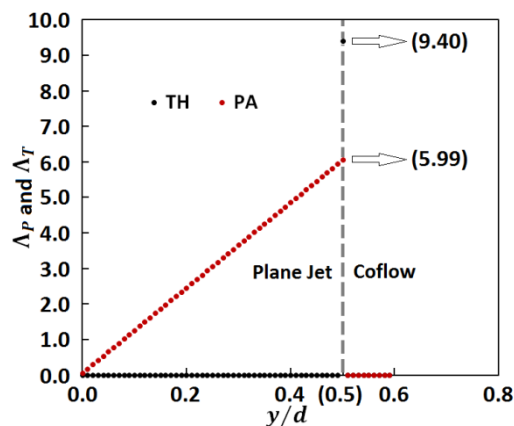


Figure 4.2 Mean streamwise velocity gradient at the jet exit

The plane jets with two kinds of mean exit velocity profiles, i.e., top hat profile (TH) and parabola profile (PA), were simulated, which have been introduced in

Chapter 2, as shown by Figure 4.1. And the mean exit scalar possesses the top hat profile in all cases. In Figure 4.1, it shows, at the jet exit with TH, a large velocity difference exists between the jet and the ambient fluid (co-flow), which will result in the highly unstable shear layers, but in the case with PA, the changes in velocity along the lateral direction are much more moderate. Figure 4.2 shows the mean streamwise velocity gradient at the jet exit, i.e.  $\Lambda_T$  for TH and  $\Lambda_P$  for PA, where  $d$  is the height of the jet exit and the peak value of  $\Lambda_T$  is divided by 10 for the convenient comparison. In both cases, the largest velocity change occurs in the interface between the jet and the co-flow, but this value is obviously larger with TH. In addition, the velocity gradient exists in the jet with PA but is absent with TH.

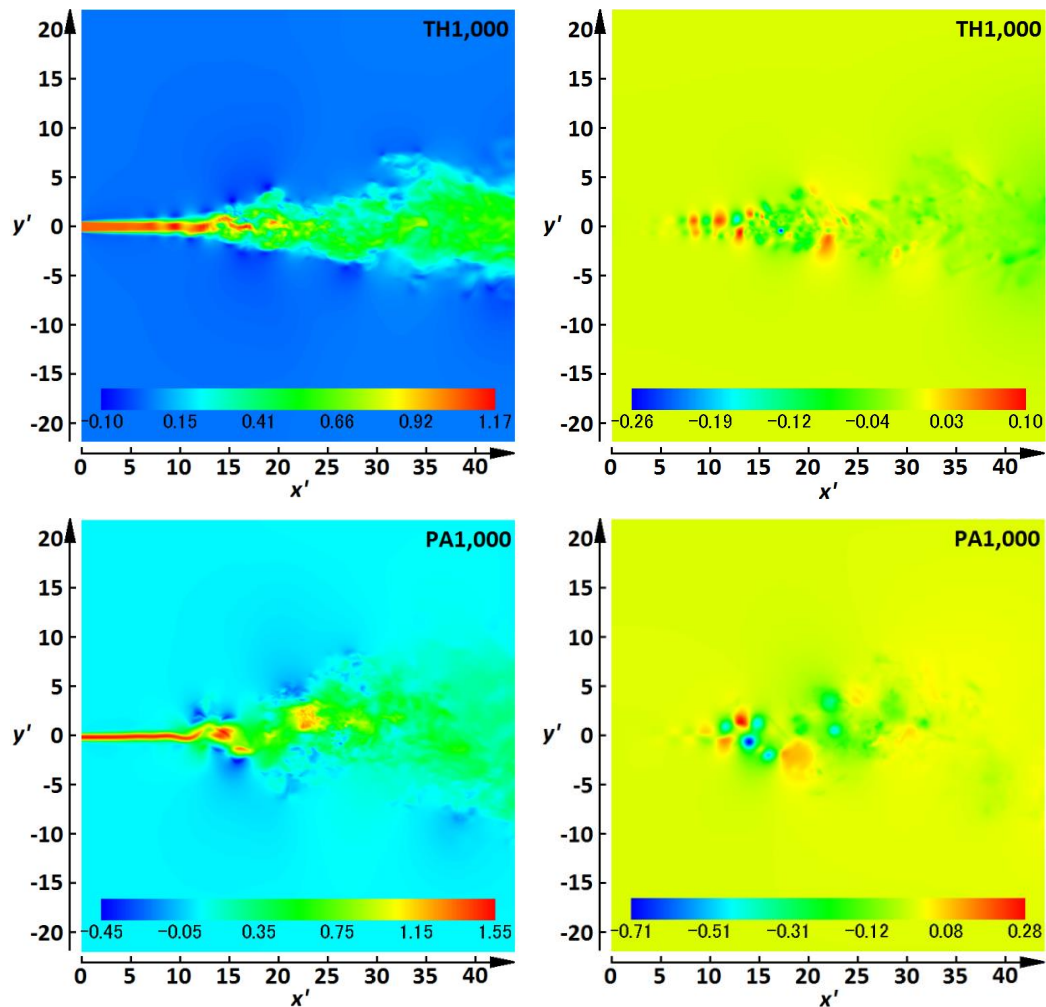


Figure 4.3a Instantaneous streamwise velocity (Left) and pressure (Right) fields at  $Re = 1,000$ . TH1,000 and PA1,000 represent the cases with top hat profile at  $Re = 1,000$  and parabola profile at  $Re = 1,000$ , respectively.

### 4.3 Instantaneous Results

In this section, the characteristics of the instantaneous flow field in the plane jet with different mean exit velocity profiles are investigated. The instantaneous data are captured at the 20,000<sup>th</sup> time step, and one time step is equal to  $0.02 d/U_b$ . In addition, in order to find the changes of the influence of mean exit velocity profile on the plane jet with different exit Re, the jets with  $Re = 1,000$  and  $Re = 3,000$  are both studied.

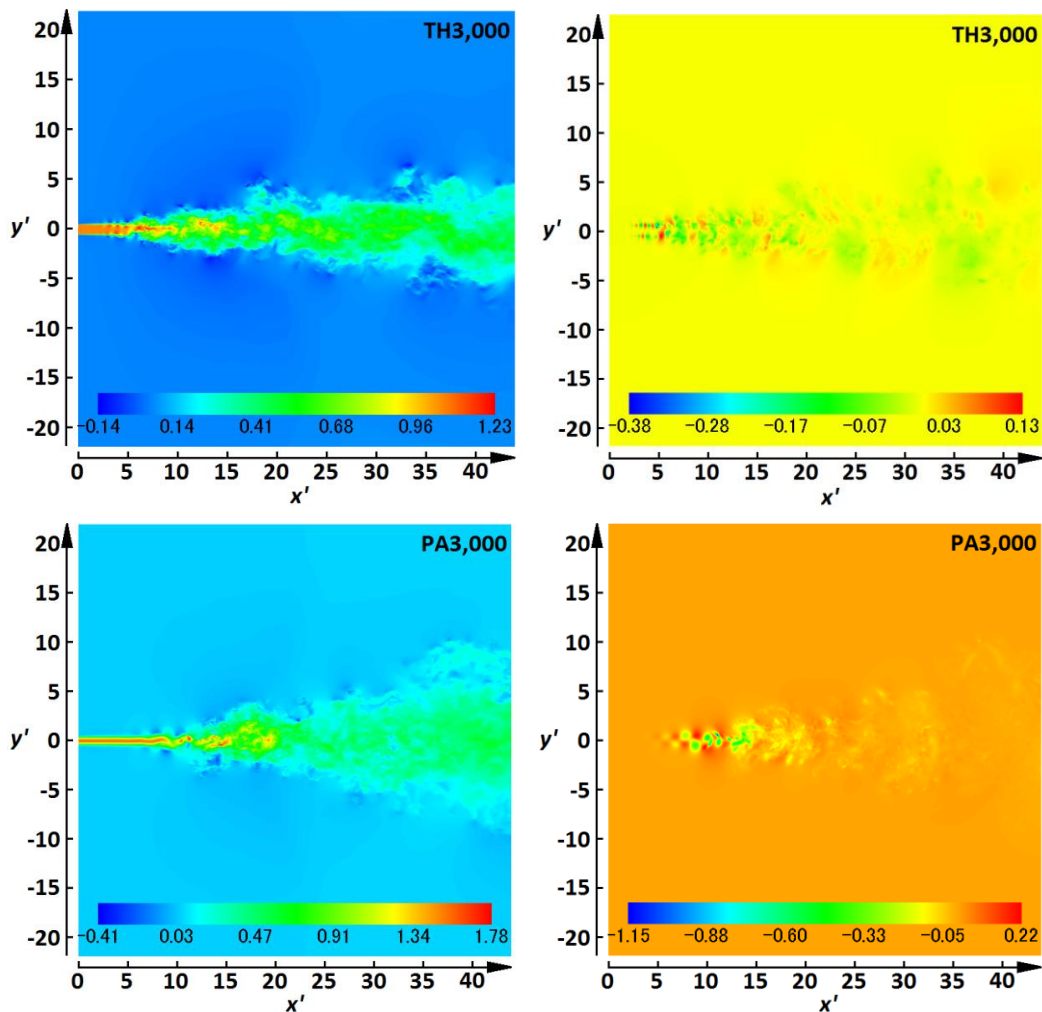


Figure 4.3b Instantaneous streamwise velocity (Left) and pressure (Right) fields at  $Re = 3,000$ . TH3,000 and PA3,000 represent the cases with top hat profile at  $Re = 3,000$  and parabola profile at  $Re = 3,000$ , respectively.

#### 4.3.1 Velocity and Pressure

Figures 4.3a (left) and 4.3b (left) show the contours of instantaneous

dimensionless streamwise velocity, and Figures 4.3a (right) and 4.3b (right) show the contours of instantaneous dimensionless pressure, in the  $x$ - $y$  plane at the location  $z = 0$ . The results show that, although no proper potential core exists for the cases with PA considering the definition of the potential core in plane jets, one zone with stable flow and quite small decay of the centerline streamwise velocity can still be observed, as shown in Figure 4.6, and the streamwise length of this zone is similar to the length of the potential core with TH at the same exit  $Re$ . In the downstream region the values of instantaneous streamwise velocity are similar between two cases with different mean exit velocity profiles.

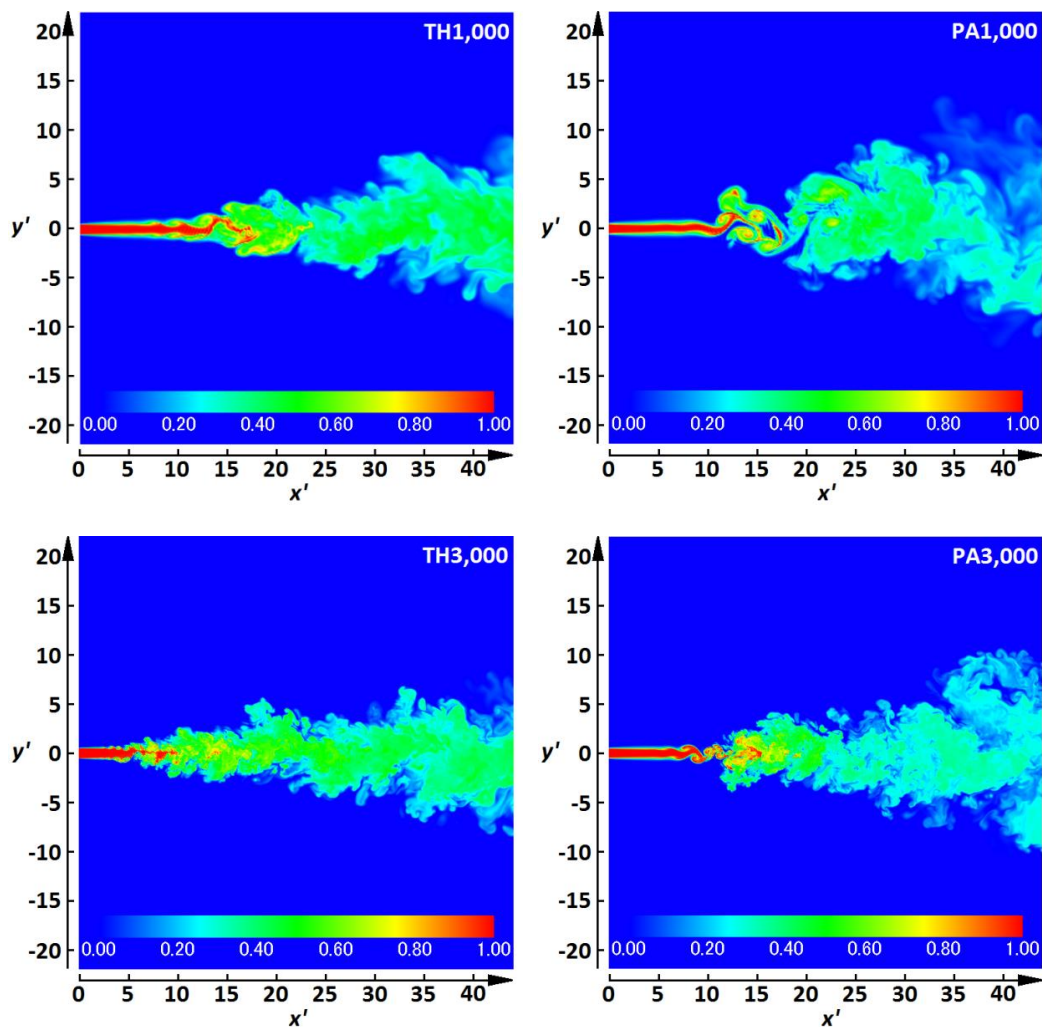


Figure 4.4 Instantaneous scalar field. TH1,000, TH3,000, PA1,000 and PA3,000 represent the cases with top hat profile at  $Re = 1,000$ , top hat profile at  $Re = 3,000$ , parabola profile at  $Re = 1,000$  and parabola profile at  $Re = 3,000$ , respectively.

One important difference between two cases with TH and PA is the arrangement of pressure cores following the end of the potential core, as shown in Figures 4.3a (right) and 4.3b (right). First, the positive and negative pressure core alternately occurs in the streamwise direction for both the case with TH and the case with PA; then, in the case with TH, the pressure cores are first symmetric and then anti-symmetric along the jet centerline, but in the case with PA, the pressure cores are only anti-symmetric, which means the lateral acceleration in the jet exists in the whole interaction region of the plane jet with PA.

#### 4.3.2 Scalar and Its Gradient

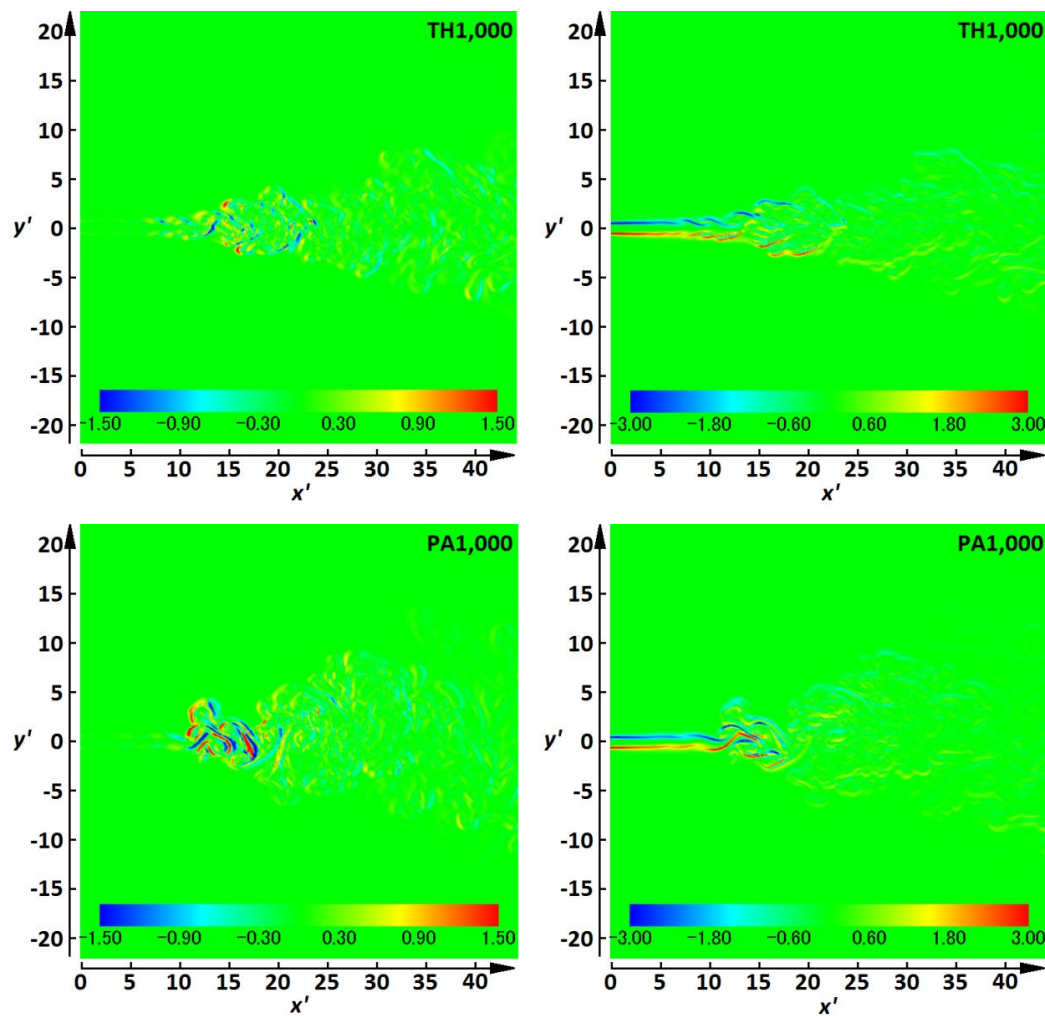


Figure 4.5a Instantaneous scalar gradient magnitude field at  $Re = 1,000$ . TH1,000 and PA1,000 represent the cases with top hat profile at  $Re = 1,000$  and parabola profile at  $Re = 1,000$ , respectively.



Figure 4.4 shows the contours of instantaneous dimensionless scalar. The results show that the performance of the instantaneous scalar behind the end of the potential core is different between the cases with TH and the cases with PA. The interaction between the ambient fluid and the jet is quite severe in the cases with PA compared to that in the cases with TH, which advances the lateral growth of the jet and the mixing between the ambient fluid and the jet.

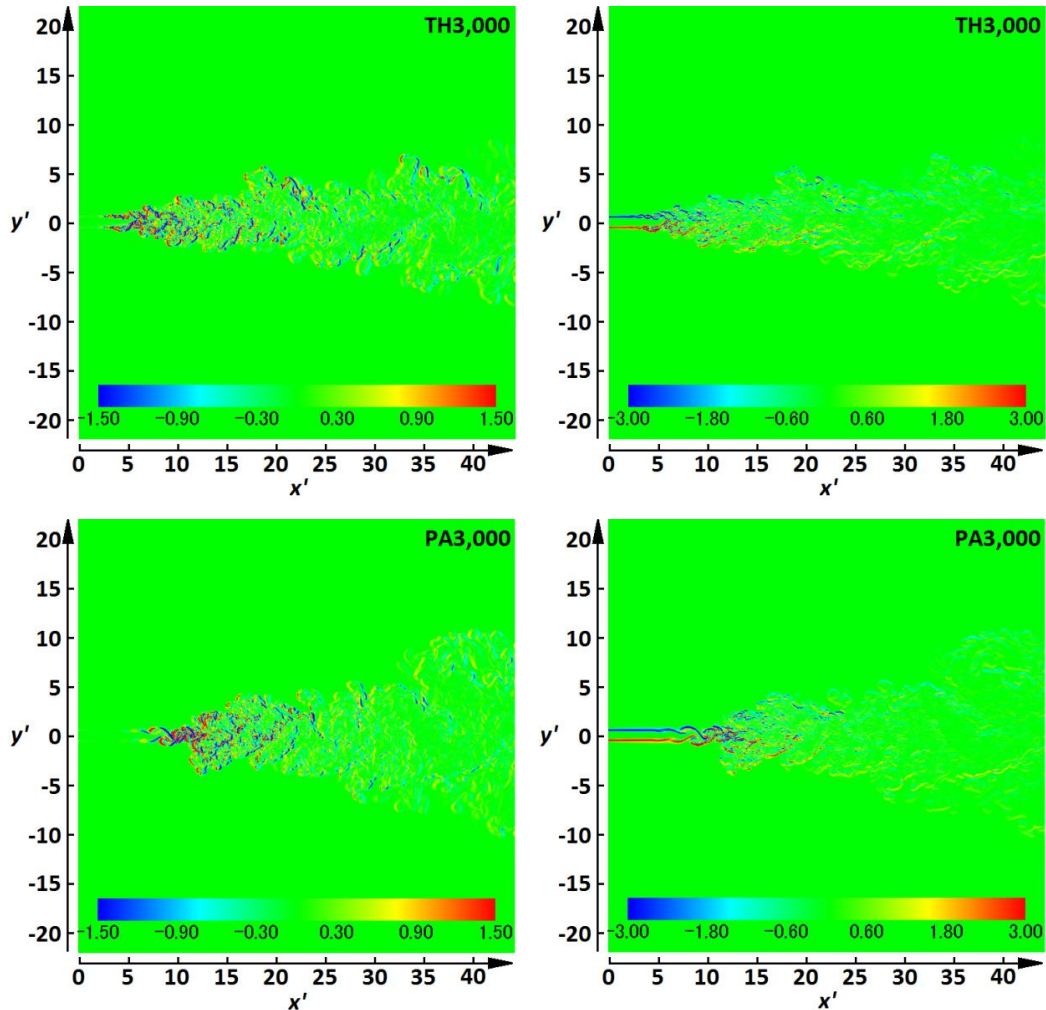


Figure 4.5b Instantaneous scalar gradient magnitude field at  $Re = 3,000$ . TH3,000 and PA3,000 represent the cases with top hat profile at  $Re = 3,000$  and parabola profile at  $Re = 3,000$ , respectively.

Here, the contours of scalar gradient magnitudes in the streamwise and lateral directions with two different exit  $Re$  are also presented, as shown by Figures 4.5a (left) and 4.5b(left), and Figures 4.5a (right) and 4.5b(right), respectively. For two cases with

$Re = 1,000$ , the scalar gradient magnitudes possess more large value with PA behind the end of the potential core, but this phenomenon is not obvious for two cases with  $Re = 3,000$ .

#### 4.4 Statistical Results

In this section, the statistical results are presented and analyzed, which are calculated by averaging in time and space, based on the data from 20,000 time steps and the data at the location of each grid across the homogenous spanwise direction, respectively, in DNS.

##### 4.4.1 Statistics along Jet Centerline

In this section, the evolution of the plane jet along the jet centerline is analyzed in view of the streamwise profiles on velocity and scalar. Some results in the work of Deo et al.[14] are also compared with the present results.

Figure 4.6 shows the mean streamwise velocity profiles, where  $U_c$  denotes the mean streamwise velocity at the jet centerline, normalized by the value of  $U_c$  at the jet exit ( $U_j$ ); meanwhile, the decay rate of  $U_c$  ( $|dU_c/dx|$ ) is presented in Figure 4.7, normalized by  $U_j/d$ ; in addition, the turbulent streamwise velocity profiles are shown by Figure 4.8, where  $u_{rmsc}$  denotes the root-mean-square (*rms*) streamwise velocity at the jet centerline, normalized by  $U_c$ .

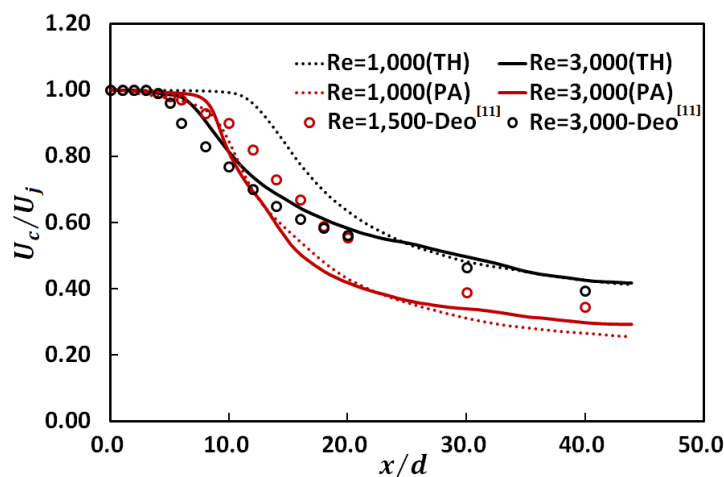


Figure 4.6 Mean streamwise velocity profiles along the jet centerline

The results show that the change on the mean exit velocity profile brings some

effects on the evolution of the streamwise velocity. One quite obvious point is the decay rate of mean velocity and the values of local maxima of the turbulent velocity are larger in the transition process of the plane jet with PA, which is related to severer interaction between the ambient fluid and the jet and larger pressure differences in this region, shown by the instantaneous figures. In the case with  $Re = 1,000$  and PA, the potential core cannot be detected based on the velocity, but behind the jet exit I can observe one region where the decay rate of  $U_c$  is almost constant. The decay of the mean flow in this case is presented by the velocity gradient in the jet, but the velocity gradient in the jet with PA is absent in the case with high  $Re$ , i.e.,  $Re = 3,000$ .

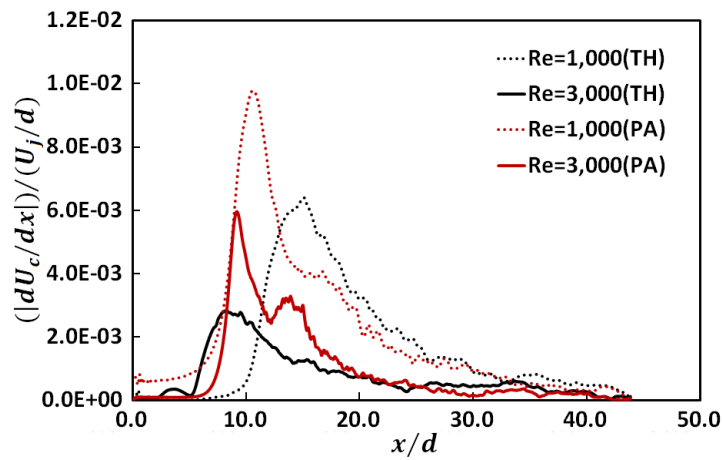


Figure 4.7 Decay rate of mean streamwise velocity along the jet centerline

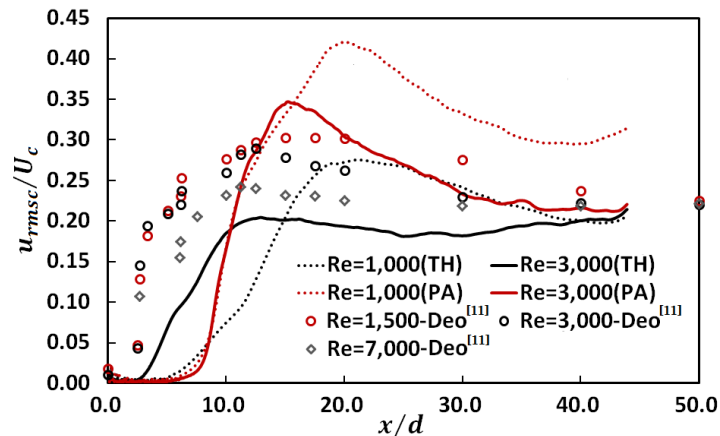


Figure 4.8 Turbulent streamwise velocity profiles along the jet centerline

In the following part, an insight into the scalar field of the plane jet will be provided. In analogy to the velocity field, Figure 4.9 shows the mean scalar profiles,

where  $\Theta_c$  denotes the mean scalar at the jet centerline, normalized by the value of  $\Theta_c$  at the jet exit ( $\Theta_j$ ); Figure 4.10 presents the decay rate of the mean scalar ( $|d\Theta_c/dx|$ ), normalized by  $\Theta_j/d$ ; Figure 4.11 shows the turbulent scalar profiles, where  $\theta_{rmsc}$  denotes the turbulent scalar at the jet centerline, normalized by  $\Theta_c$ .

The effects of mean velocity profile at the jet exit on the scalar field are similar to that on the velocity field, likewise the decay rate of mean scalar and the values of local maxima of the turbulent scalar present larger in the transition process of the plane jet with PA.

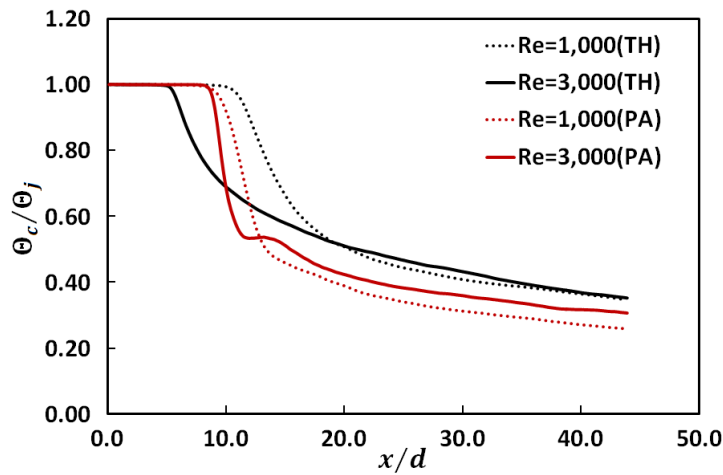


Figure 4.9 Mean scalar profiles along the jet centerline

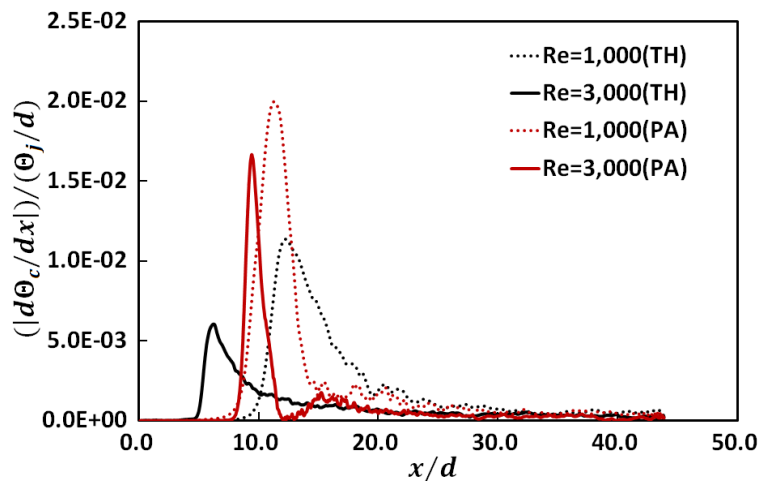


Figure 4.10 Decay rate of mean scalar along the jet centerline

Furthermore, in comparison with the velocity field, the scalar field attains the fully-developed state faster, which means that the decay of mean scalar becomes

linear, and the turbulent scalar becomes constant at a closer streamwise location to the jet exit. Meanwhile, it is found that the overall magnitude and local maxima of the turbulent scalar and the decay rate of mean scalar are larger. These results may be attributed to the choice of  $Pr(= 0.7)$ , the higher scalar diffusion rate, compared to the viscous diffusion rate, is beneficial to the transition to the fully-developed state and lead to stronger turbulent level.

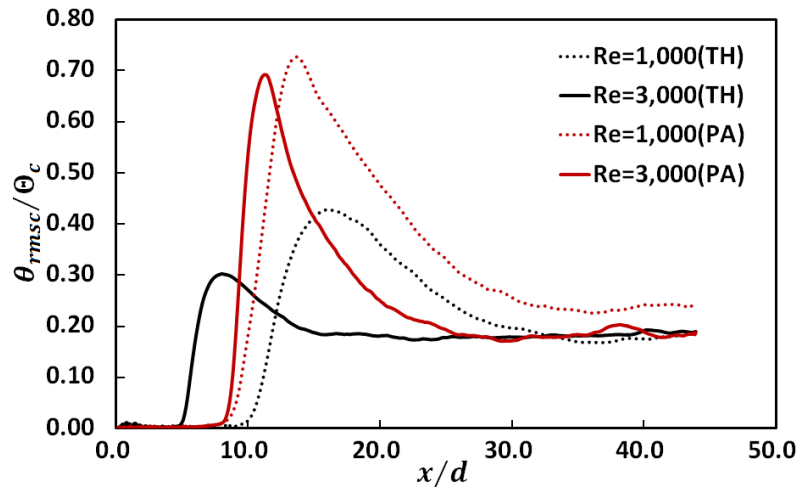


Figure 4.11 Turbulent scalar profiles along the jet centerline

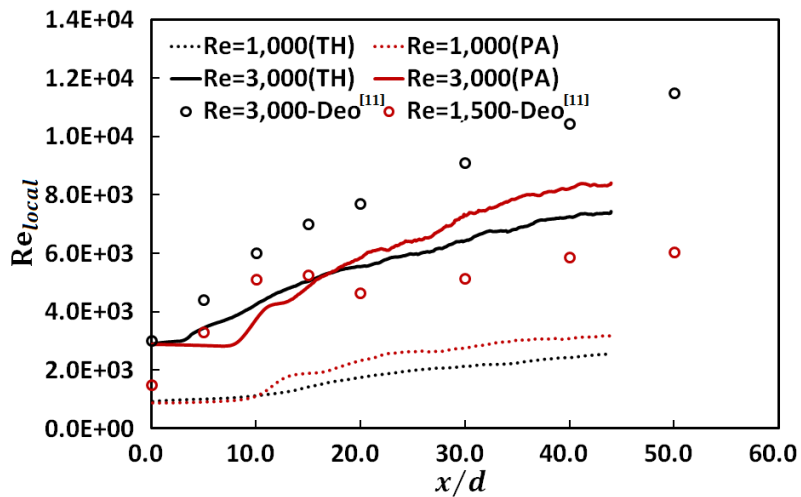


Figure 4.12 Evolution of local Re along the jet centerline

Furthermore, the cross-impact between two initial factors is discussed, i.e., the exit Re and the exit profile of the mean velocity, which causes some difference on the effects of the single factor on the plane jet. Comparing the exit Re-dependency of the

plane jet in the cases with PA with that in the cases with TH, it is observed that the length of the potential core is almost same in two cases with different exit  $Re$ , and in the downstream region the turbulent values of velocity and scalar with different  $Re$  don't converge like that with TH. Here, it needs be highlighted that the cross-impact between all kinds of factors related to the initial condition of the plane jet should be discussed in the relative studies.

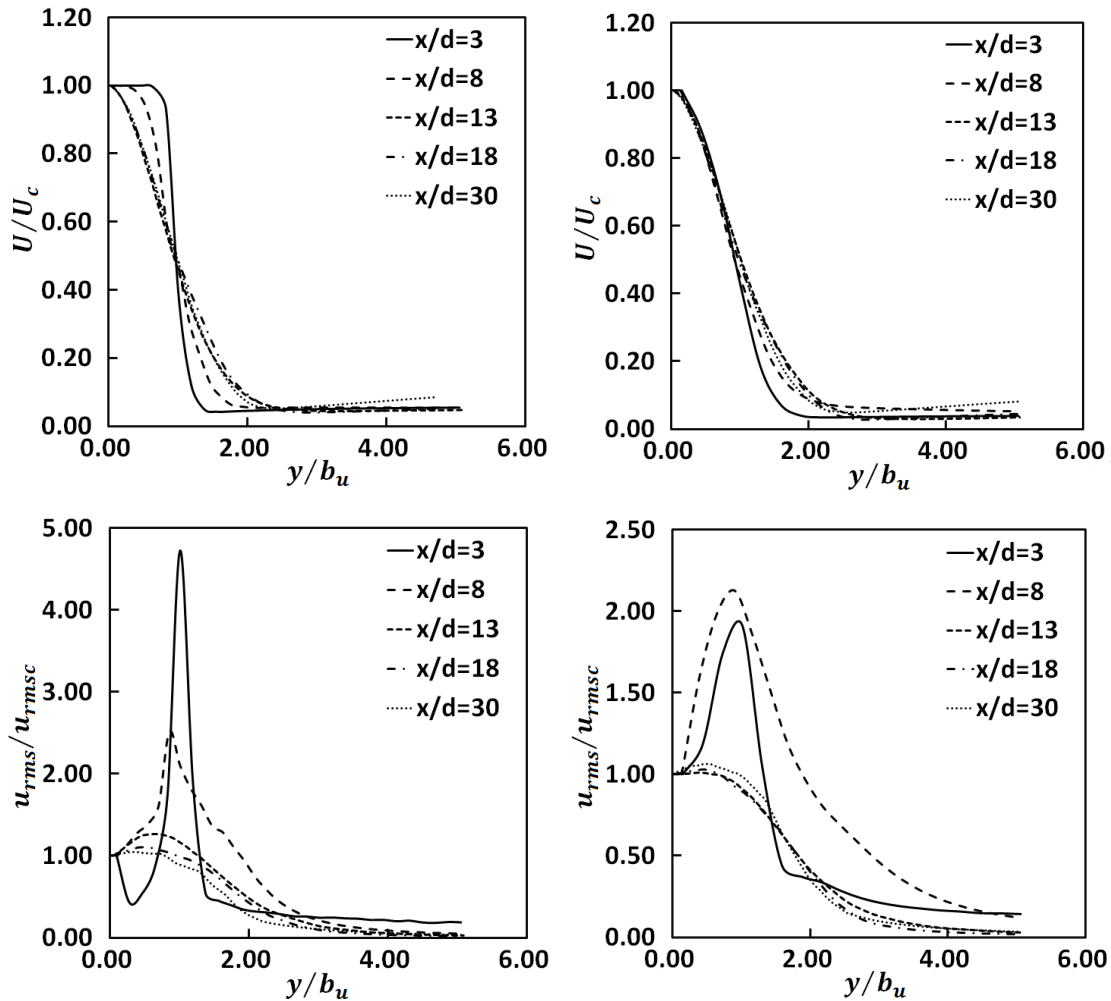


Figure 4.13 Lateral profiles of mean and turbulent streamwise velocities with  $Re = 2,000$ . (Left) The case with TH; (Right) the case with PA.

Further comparison is based on the local Reynolds number  $Re_{local}$ , which is defined as  $2b_u U_c / \nu$ , where  $b_u$  is the half-width of the mean streamwise velocity profile. Figure 4.12 shows the variation of  $Re_{local}$  along the jet centerline. The increase of  $Re_{local}$  with the flow development marks the transition of the flow from laminar to fully-developed turbulence, and this increase is slower at the low exit  $Re$ .

Comparing the results in DNS and experiments, Smaller  $Re_{local}$  in the DNS is also attributed to the existence of the co-flow, which can slow the turbulence development in the jet.

#### 4.4.2 Lateral Evolution of Plane Jet

##### 4.4.2.1 Self-similarity

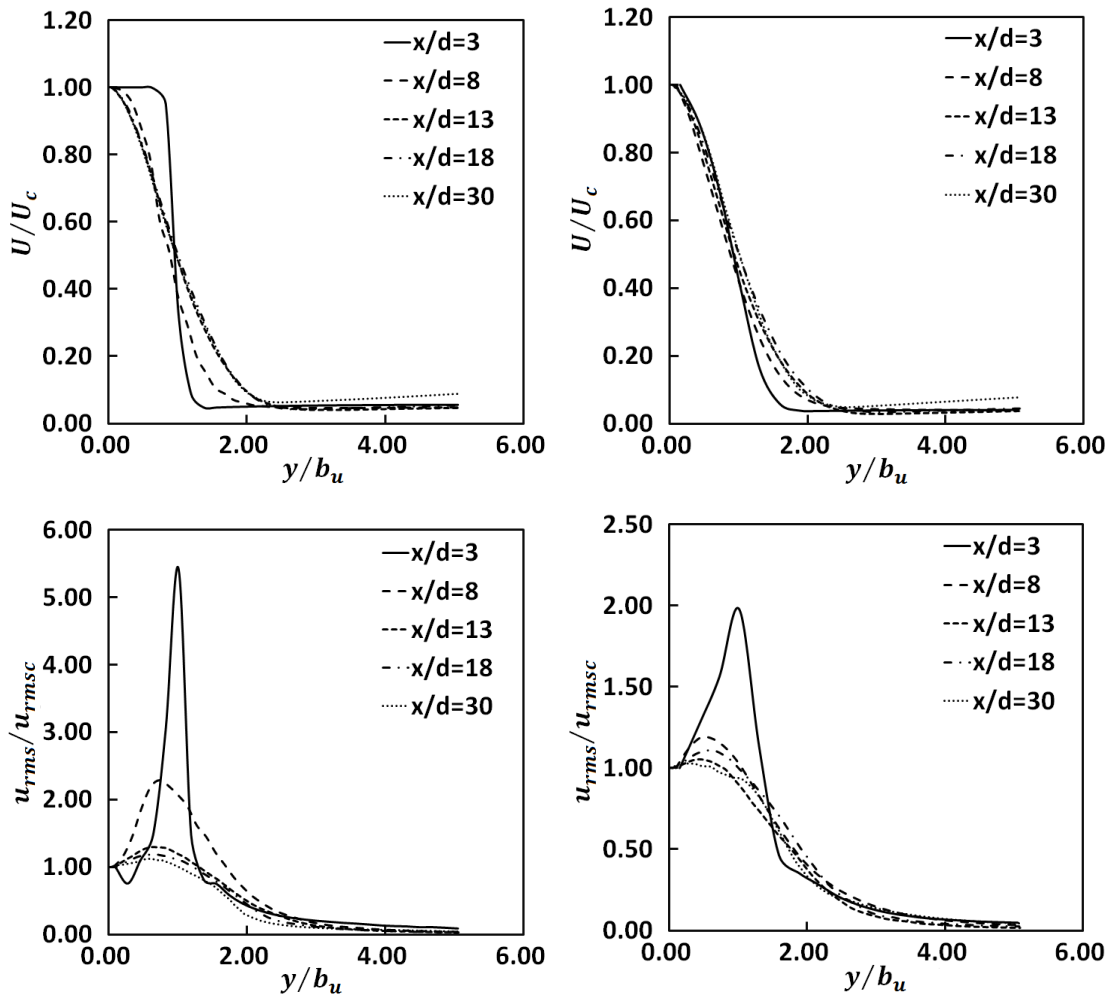


Figure 4.14 Lateral profiles of mean and turbulent streamwise velocities with  $Re = 3,000$ . (Left) The case with TH; (Right) the case with PA.

In this section, the influence of mean exit velocity profile on the self-similarity of the plane jet is studied based on the lateral profiles of velocity. The jets with  $Re = 2,000$  and  $Re = 3,000$  are analyzed for discussing this topic.

The lateral profiles of the mean and turbulent streamwise velocities are shown by Figure 4.13 for  $Re = 2,000$ , and Figure 4.14 for  $Re = 3,000$ , respectively, at five

different streamwise locations. The local centerline mean streamwise velocity ( $U_c$ ), the local centerline turbulent streamwise velocity ( $u_{rmsc}$ ), and the half-width of the mean velocity profile ( $b_u$ ) are used to normalize the parameters. With two different exit Re, in the cases with PA the results show that the self-similarities of the parameters are achieved faster, especially for the turbulent ones.

#### 4.4.2.2 Evaluation of Lateral Profiles

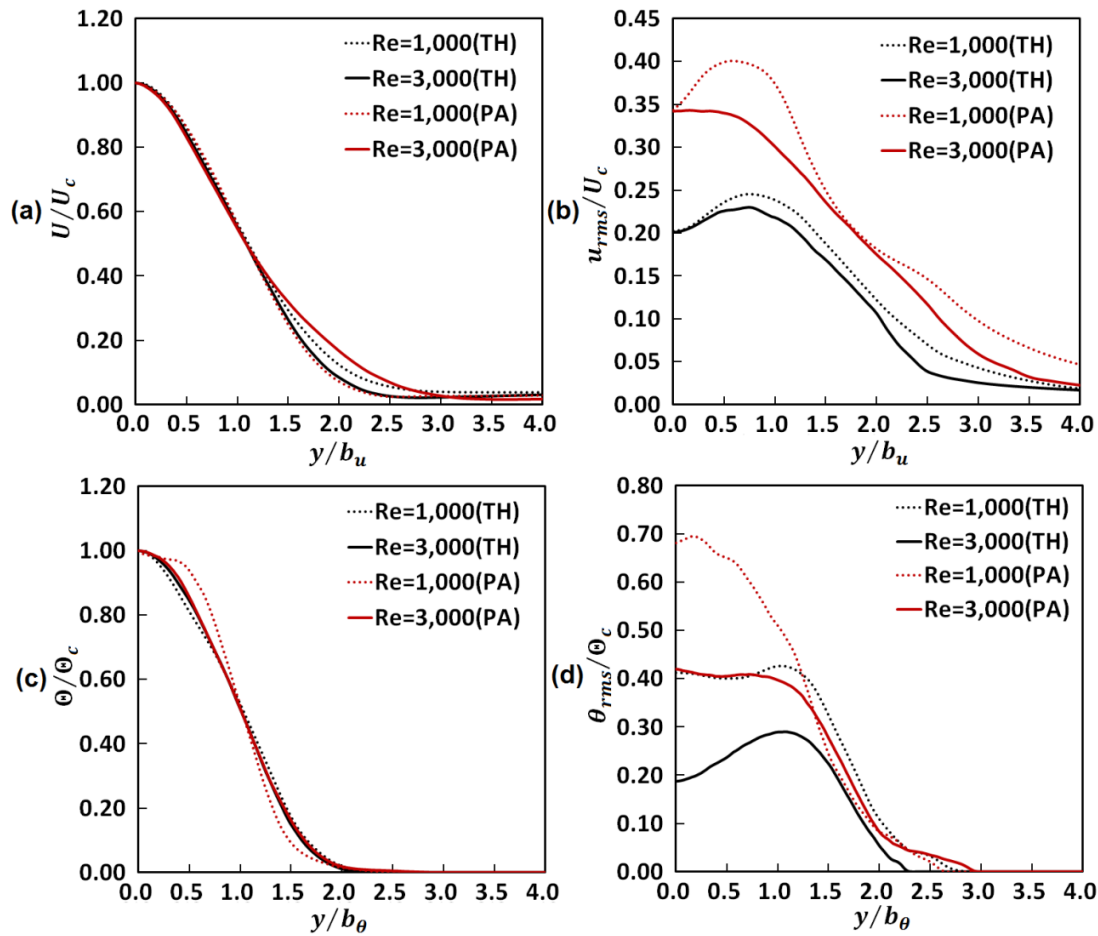


Figure 4.15 Lateral profile of variables at  $x/d = 15.0$ . (a) Mean streamwise velocity; (b) turbulent streamwise velocity; (c) mean scalar; (d) turbulent scalar.

The lateral evolution of the plane jet and the influence of mean exit velocity profiles are studied at two streamwise locations,  $x/d = 15.0$  and  $x/d = 35.0$ . Figures 4.15 and 4.16 illustrate the lateral profiles of the streamwise velocity and scalar, in which the lateral coordinate  $y$  is normalized by  $b_u$  (the half jet width for the mean velocity field), and  $b_\theta$  (the half jet width for the mean scalar field), respectively.



The influence of mean exit velocity profiles on the lateral evolution of mean flow is not obvious based on the lateral profiles of mean variables at two locations. At  $x/d = 15.0$ , the turbulent intensity stays at a stronger level with the cases with PA; at  $x/d = 35.0$ , the lateral profiles of turbulent variables present similar contour and almost coincide in two cases with  $Re = 3,000$  and the case with  $Re = 1,000$ (PA), which shows the influence of mean exit velocity profiles is also weak in the downstream region similar to the influence of exit  $Re$ , studied in Chapter 3.

Figures 4.17(a) and 4.19(a) show the lateral profiles of Reynolds stress, and the lateral profiles of turbulent scalar fluxes are shown in Figures 4.17(b), 4.17(c), 4.19(b), and 4.19(c), in which the symbol  $\langle \rangle$  denotes the statistics calculated by averaging in time, based on the data from 20,000 time steps, as well as across the homogenous spanwise direction.

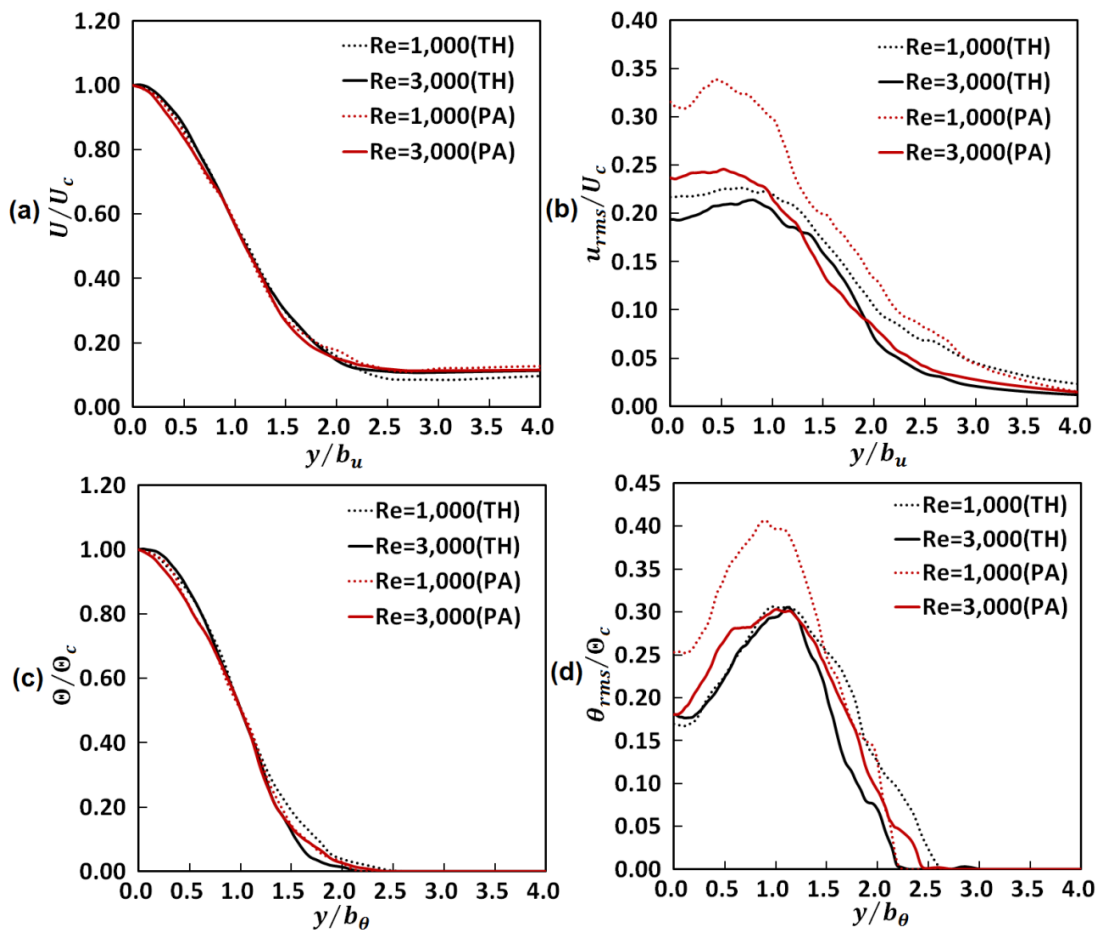


Figure 4.16 Lateral profile of variables at  $x/d = 35.0$ . (a) Mean streamwise velocity; (b) turbulent streamwise velocity; (c) mean scalar; (d) turbulent scalar.

At  $x/d = 15.0$ , in the cases with PA the fluxes of streamwise momentum and scalar caused by the fluctuating velocity field are enhanced. In the case with  $Re = 1,000(PA)$ , the Reynolds stress and turbulent scalar flux in the lateral direction are not zero at the jet centerline, which should be zero considering the statistical symmetry of the plane jet. These results should be attributed to the quite severe sway of the jet in the lateral direction in comparison with the other cases, which can be checked in the instantaneous fields, and the flow structure at  $x/d = 15.0$ , which will be discussed in Chapter 5. By computing the statistics based on more 10,000 samples than the original sample numbers, the deviation of these two variables from zero becomes smaller, as shown by Figure 4.18, in which  $\Gamma'$  and  $y'$  are the dimensionless variables and lateral coordinate, respectively.

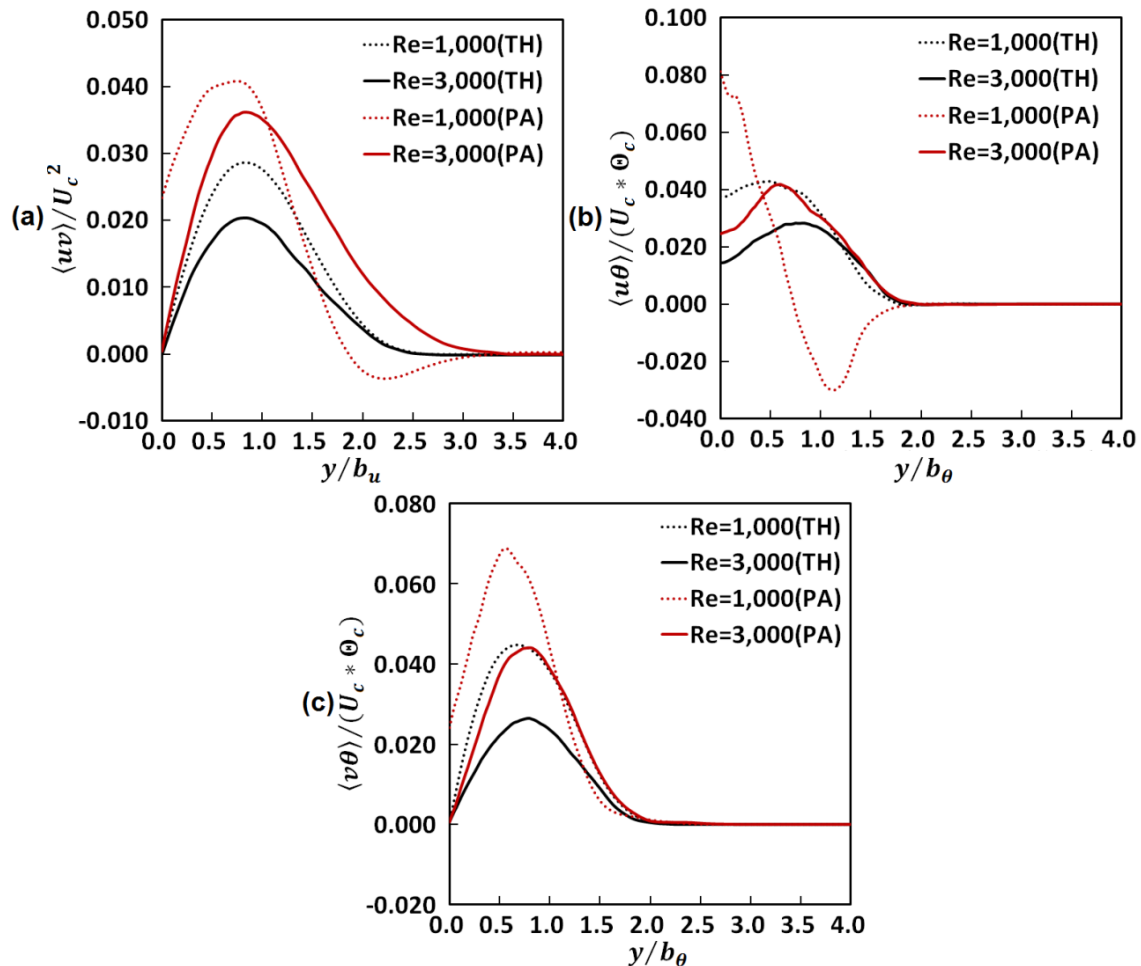


Figure 4.17 Lateral profile of variables at  $x/d = 15.0$ . (a) Reynolds stress; (b) streamwise turbulent scalar flux; (c) lateral turbulent scalar flux.

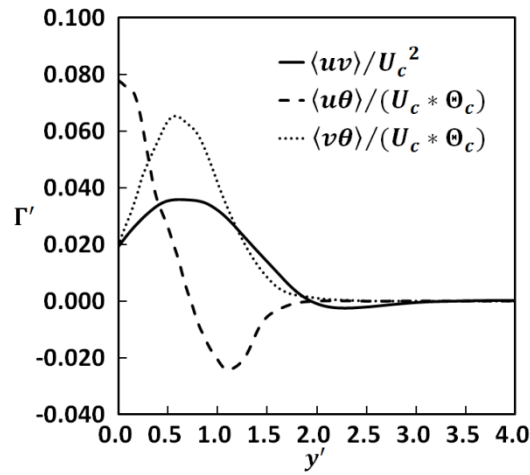


Figure 4.18 Lateral profile of variables at  $x/d = 15.0$  in the case of  $Re = 1,000$ (PA) based on 30,000 samples

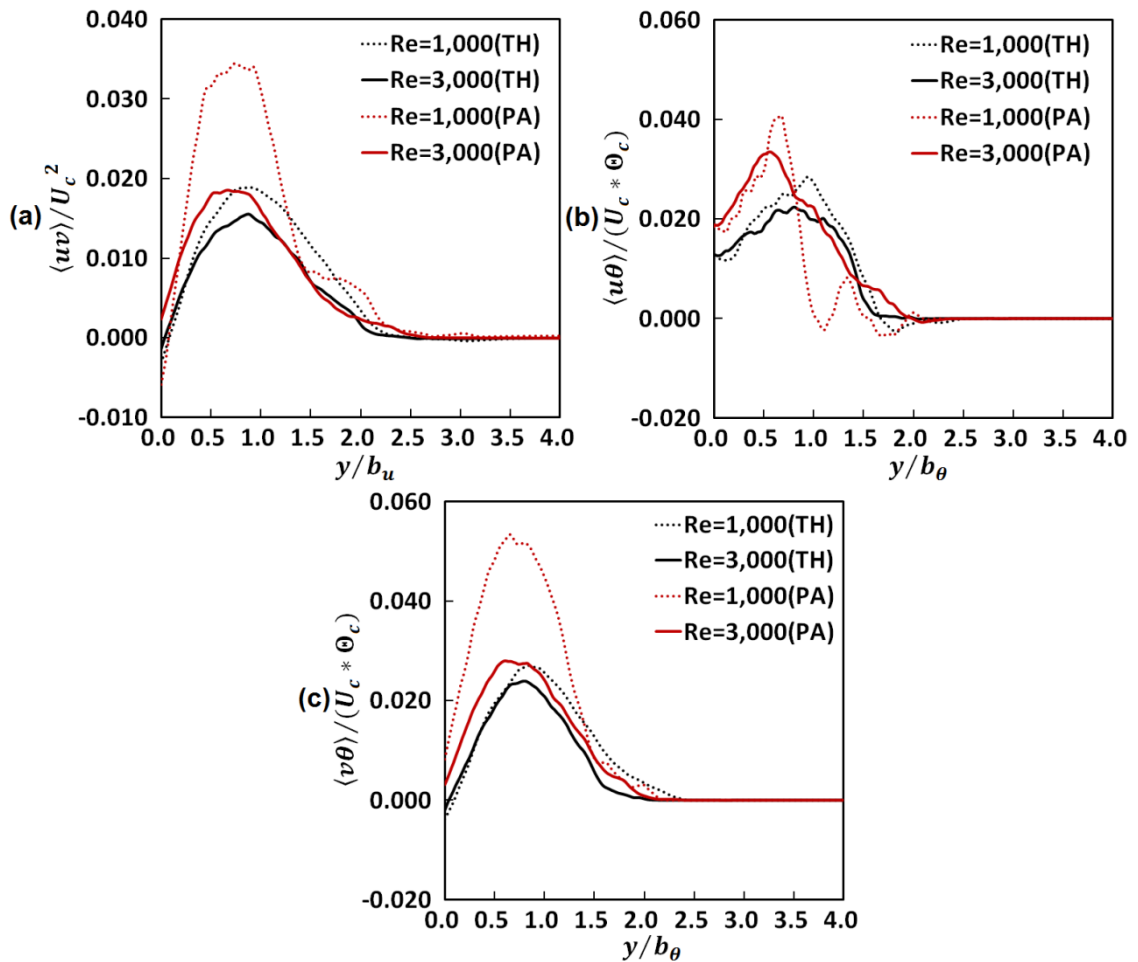


Figure 4.19 Lateral profile of variables at  $x/d = 35.0$ . (a) Reynolds stress; (b) streamwise turbulent scalar flux; (c) lateral turbulent scalar flux.

At  $x/d = 35.0$ , the lateral profiles of variables also present similar contour and almost coincide in two cases with  $Re = 3,000$  and the case with  $Re = 1,000$ (TH). But in the case with  $Re = 1,000$ (PA), the lateral profiles of variables are quite different, which implies the effect of the exit  $Re$  is amplified in the cases with PA in the downstream region of the plane jet.

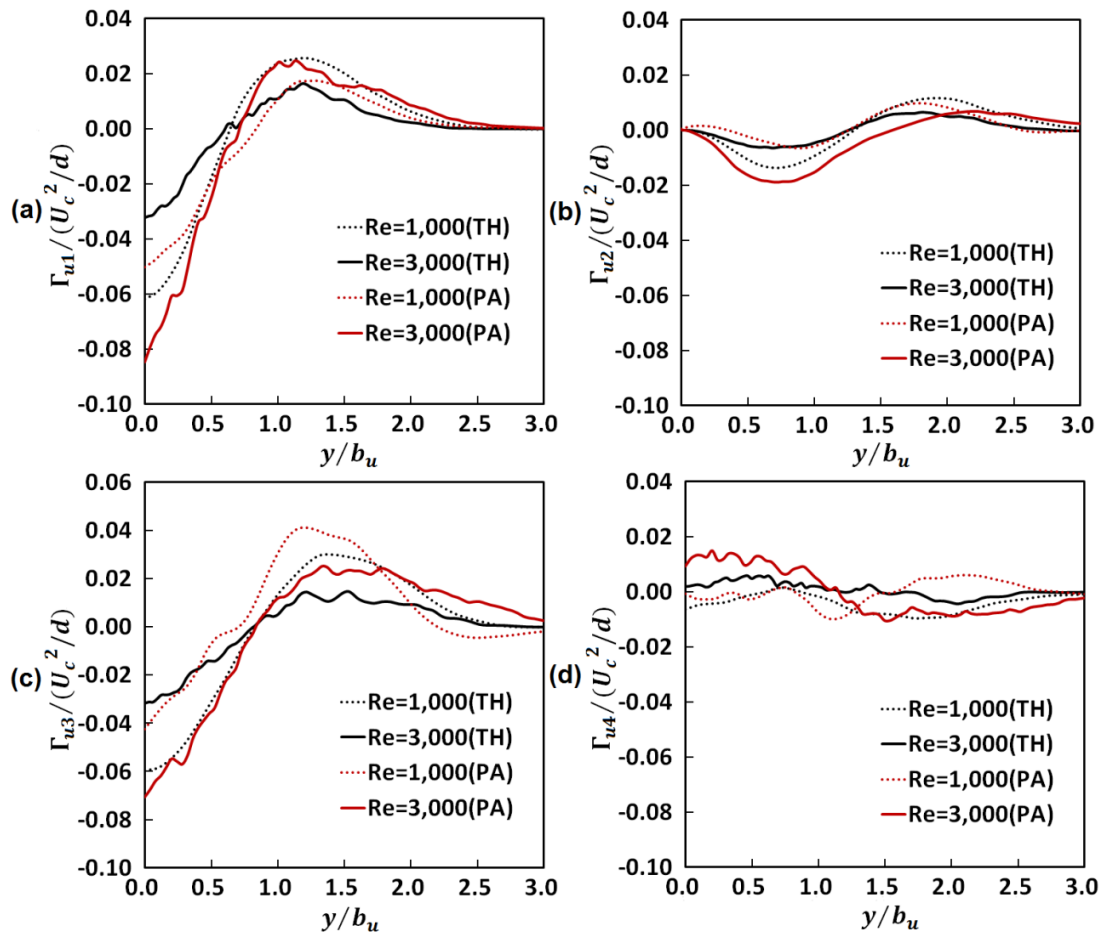


Figure 4.20 Lateral profile of the mean streamwise momentum transport at  $x/d = 15.0$ . (a) Streamwise convection term; (b) lateral convection term; (c) lateral turbulent transport term; (d) streamwise turbulent transport term.

The behaviors of the convection and turbulent transport in the mean streamwise momentum transport are investigated in the following part. Figures 4.20 and 4.21 show the lateral profiles of four terms, i.e., the streamwise convection term ( $\Gamma_{u1} = U(\partial U/\partial x)$ ), the lateral convection term ( $\Gamma_{u2} = V(\partial U/\partial y)$ ), the lateral turbulent transport term ( $\Gamma_{u3} = \partial\langle uv\rangle/\partial y$ ), and the streamwise turbulent transport

term ( $\Gamma_{u4} = \partial\langle u^2 \rangle / \partial x$ ), which are non-dimensionalized by  $U_c^2/d$ , at the location  $x/d = 15.0$ .

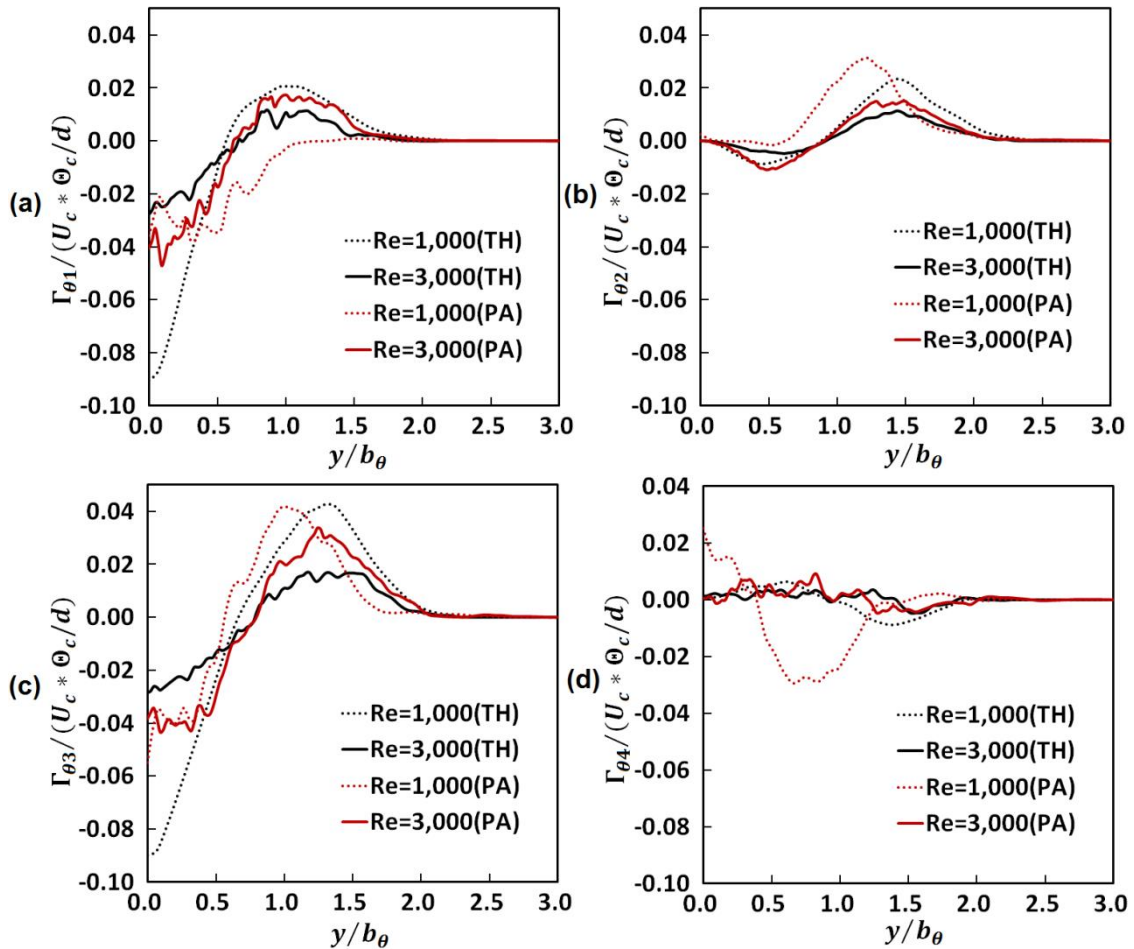


Figure 4.21 Lateral profile of the mean scalar transport at  $x/d = 15.0$ . (a) Streamwise convection term; (b) lateral convection term; (c) lateral turbulent transport term; (d) streamwise turbulent transport term.

At  $x/d = 15.0$ , the streamwise convection and lateral turbulent transport are dominant in the mean streamwise momentum transport, especially in the region near the jet centerline. The influence of mean exit velocity profile on the convection and turbulent transport acting on the mean streamwise momentum transport is not clear comparing the data in the present cases; meanwhile, the influence of exit Re is also smeared in the cases with PA.

The lateral evolution of these four terms in the mean scalar transport are calculated at the location  $x/d = 15.0$ , shown by Figure 4.21, which are the

streamwise convection term ( $\Gamma_{\theta_1} = U(\partial\theta/\partial x)$ ), the lateral convection term ( $\Gamma_{\theta_2} = V(\partial\theta/\partial y)$ ), the lateral turbulent transport term ( $\Gamma_{\theta_3} = \partial\langle v\theta \rangle/\partial y$ ), and the streamwise turbulent transport term ( $\Gamma_{\theta_4} = \partial\langle u\theta \rangle/\partial x$ ), normalized by  $U_c\theta_c/d$ . These four terms show the similar behavior to their counterpart in the mean streamwise momentum transport, except the streamwise turbulent transport term with  $Re = 1,000(PA)$ .

#### 4.5 Conclusion

In this chapter, based on the data from DNS of plane jets with two kinds of mean velocity profiles at the jet exit, the influence of the exit mean velocity profile is investigated; meanwhile, the cross impact between the exit  $Re$  and the exit mean velocity profile is also discussed.

Main results are summarized as follows:

1. The obvious influence of the exit mean velocity profile is observed in the present study. In the transition process of the plane jet, the large decay rate of mean variables and large local maxima of the turbulent variables are found, and the fluxes of streamwise momentum and scalar caused by the fluctuating velocity field are enhanced in the cases with PA.
2. The influence of mean exit velocity profiles is also weak in the downstream region similar to the influence of exit  $Re$ .
3. The cross-impact between the exit  $Re$  and the exit profile of the mean velocity exists and cannot be ignored. In the cases with PA, the effect of the exit  $Re$  is amplified in the downstream region of the plane jet, and the length of the potential core is almost same in two cases with different exit  $Re$ , and in the downstream region the turbulent values of velocity and scalar with different exit  $Re$  do not converge like that with TH.

#### References

- [1] WU N., SAKAI Y., NAGATA K., SUZUKI H., TERASHIMA O. and HAYASE T. Analysis of flow characteristics of turbulent plane jets based on velocity and scalar fields using DNS[J]. *Journal of Fluid Science and Technology*, **2013**, 8(3): 247-261.

- [2] WU N., SAKAI Y., NAGATA K., ITO Y., TERASHIMA O. and HAYASE T. Influence of Reynolds number on coherent structure, flow transition, and evolution of the plane jet[J]. *Journal of Fluid Science and Technology*, **2014**, 9(2): 14pages.
- [3] WU N., SAKAI Y., NAGATA K., SUZUKI H., TERASHIMA O. and HAYASE T. Analysis of flow characteristics of turbulent plane jets based on velocity and scalar fields using DNS[C]. *Proceeding of the 9<sup>th</sup> International Conference on Flow Dynamics*, Sendai, Japan, **2012**: 98-99.
- [4] HUSSAIN A. K. M. F. and CLARK A. R. Upstream influence on the near field of a plane turbulent jet[J]. *Physics of Fluids*, **1977**, 20(9): 1416-1426.
- [5] GEORGE W. K. *Advances in Turbulence - The self-preservation of turbulent flows and its relation to initial conditions and coherent structures*[M]. Berlin, Germany: Springer-Verlag, **1989**: 39-73.
- [6] HUSSAIN A. K. M. F. and ZEDAN M. F. Effects of the initial condition on the axisymmetric free shear layer: Effects of the initial momentum thickness[J]. *Physics of Fluids*, **1978**, 21(7): 1100-1112.
- [7] GOLDSCHMIDT V. W. and BRADSHAW P. Effect of nozzle exit turbulence on the spreading (or widening) rate of plane free jets[C]. *Joint Engineering, Fluid Engineering and Applied Mechanics Conference*, ASME, Boulder, Colorado, USA, **1981**: 1-7.
- [8] CHAMBERS A. J., ANTONIA R. A. and BROWNE L. W. B. Effect of symmetry and asymmetry of turbulent structures on the interaction region of a plane jet[J]. *Experiments in Fluids*, **1985**, 3(6): 343-348.
- [9] DEO R. C., MI Jian-chun and NATHAN G. J. The influence of nozzle-exit geometric profile on statistical properties of a turbulent plane jet[J]. *Experimental Thermal and Fluid Science*, **2007**, 32(2): 545-559.
- [10] VAN DER HEGGE ZIJNEN B. G. Measurements of the distribution of heat and matter in a plane turbulent jet of air[J]. *Applied Scientific Research, Section A*, **1958**, 7(4): 277-292.
- [11] BASHIR J. and UBEROI M. S. Experiments on turbulent structure and heat transfer in a two-dimensional jet[J]. *Physics of Fluids*, **1975**, 18(4): 405-410.
- [12] GOULDIN F. C., SCHEFER R. W., Johnson S. C. and Kollmann W. Nonreacting turbulent mixing flows[J]. *Progress in Energy and Combustion Science*, **1986**,

12(4): 257-303.

[13] DEO R. C., MI Jian-chun and NATHAN G. J. The influence of nozzle aspect ratio on plane jets[J]. *Experimental Thermal and Fluid Science*, **2007**, 31(8): 825-838.

[14] DEO R. C., MI Jian-chun and NATHAN G. J. The influence of Reynolds number on a plane jet[J]. *Physics of Fluids*, **2008**, 20(7): 075108.

*[J]: Journal Article*

*[M]: Monograph*

*[C]: Conference Proceeding*



## Chapter 5

### **VISUALIZATION AND STUDY ON COHERENT STRUCTURE AND TURBULENT/NON-TURBULENT INTERFACE[1][2]**

Via the Reynolds decomposition, turbulent flow is decomposed into an average or steady component and a perturbation or fluctuating component, in which the fluctuating component is characterized by the eddies over a wide range of length scales and structures. As a result, the turbulent flow can be realized as a superposition of a spectrum of velocity fluctuations or eddies upon a mean flow. It is important to study the characteristics of eddies embodied in the turbulent flow. The eddies or vortices are generally defined as the coherent patterns of velocity, vorticity and pressure, therefore, in this chapter, based on the data about velocity, pressure and scalar, the characteristics of coherent structure (CS) and turbulent/non-turbulent (T/NT) in the plane jet with different initial conditions are analyzed.

#### **5.1 Introduction to Coherent Structure in Turbulence**

Study on CS is the effort to find the order in the apparent disorder of turbulence. It is now accepted that the evolution and behavior of any shear flow may be controlled by coherent structures, which are of varying size and are responsible for the energy exchange between the mean flow and the turbulence. In the flow development, the evolution and interaction of these CSs create a complex three-dimensional flow field that eventually evolves to a self-similar state in the far-field.

The investigation on the importance, perhaps even the dominance of the CSs on the processes of heat, mass, and momentum transport in turbulent flows started around 1970, about the turbulent boundary layer by Kline et al.[3], the turbulent mixing layer by Brown and Roshko[4], the turbulent plane jet by Bradbury[5], and

Everitt and Robins[6]. Afterwards, some discussions about the effects of the initial conditions on the characteristics and evolution of CSs in shear flows were also made by Gutmark and Ho[7], and Hussain[8]. The dynamics and characteristics of CS keep being a hot and necessary topic in turbulence study since it was involved, in which one significant job, need be done, is the identification of CS.

In Lesieur's book[9], CSs are tentatively described as regions of the flow satisfying three conditions:

1. The vorticity concentration  $\omega$  should be high enough in order to produce a local roll up of the surrounding fluid.
2. The local roll up should approximately keep their shape during a time, which is far enough in front of the local turnover time  $\omega^{-1}$ .
3. The local roll up should be unpredictable.

Following these features, it seems that a high vorticity modulus  $\omega$  could be a possible candidate for the identification of CS. Based on  $\omega$ -isosurfaces, Comte et al.[10] investigated the formation and dynamics of three-dimensional vortices in spatially-growing incompressible mixing layers. However, this method does not always work, for example, in the flows with a solid boundary, where the mean shear created by the no-slip condition is usually much larger than the typical vorticity concentration of the near-boundary vortices. Therefore, some work are needed to distinguish vortices from internal shear layers, focusing on this topic, Dubief and Delcayre[11] tried to find the proper coherent-vortex identification method in turbulence study, in which criterions based on the pressure, vorticity, second eigenvalue  $\lambda_2$ [12] and second invariant of velocity gradient were used and compared to detect the CSs in the isotropic turbulence, mixing layer, backward-facing step flow and channel flow.

## 5.2 Coherent Structure in Plane Jet

In this section, the case with  $Re = 2,000$ (TH) is taken for example to illustrate the CS in the plane jet.

In the present work, the CS in plane jets is identified by performing the flow structure visualization schemes based on the low pressure iso-surfaces and  $Q$ -criterion. Following the work of da Silva and Metals[13], it is found only the most

intense and large-scale vortices in flow evolution can be visible based on the iso-surfaces of the pressure; meanwhile the  $Q$ -criterion not only displays these intense structures but also provides a more detailed view of the other small-scale structures.

The  $Q$ -criterion was named after the second invariant of the velocity gradient tensor  $\nabla \vec{u}$ [14],

$$Q = 1/2 (\Omega_{ij}\Omega_{ij} - S_{ij}S_{ij}) \quad (5.1)$$

where  $\Omega_{ij} = (\partial u_i/\partial x_j - \partial u_j/\partial x_i)/2$  is the antisymmetric component of  $\nabla \vec{u}$ ;  $S_{ij} = (\partial u_i/\partial x_j + \partial u_j/\partial x_i)/2$  is the symmetric component of  $\nabla \vec{u}$ ;  $u_i$  and  $u_j$  represent the components of the instantaneous velocity vector;  $x_i$  and  $x_j$  represent the coordinates in a three-dimensional Cartesian coordinate system.

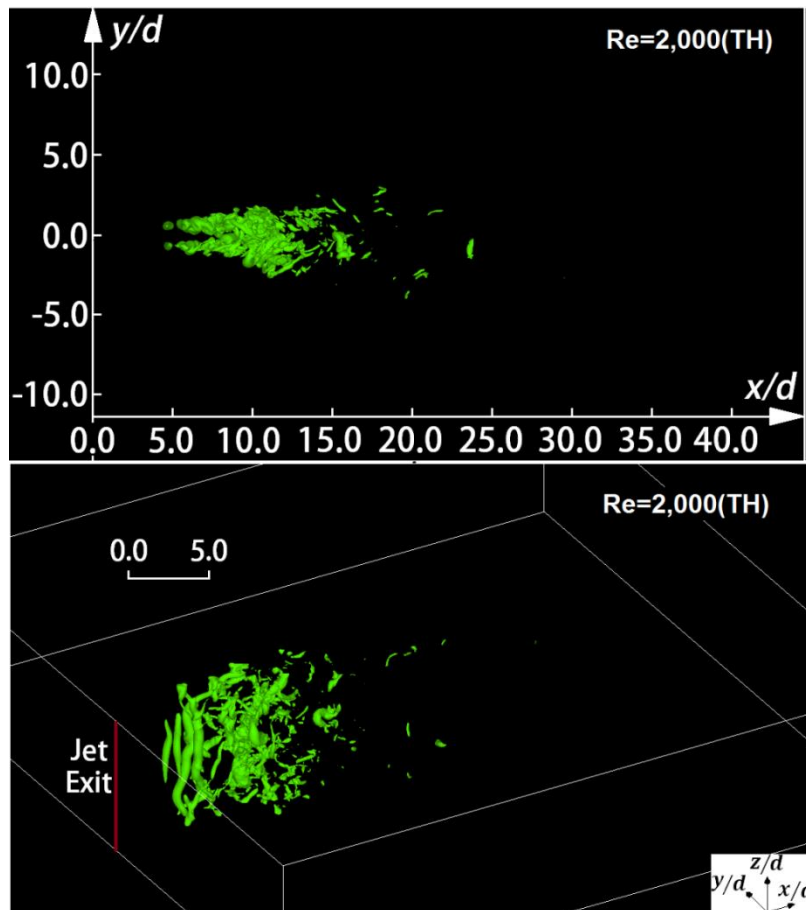


Figure 5.1 CS in the plane jet based on the isosurfaces of pressure

The amount and size of CS detected is closely related to the choice of the threshold values of  $Q$  and  $p$ . In the present work, based on the suggestions about

the threshold values of  $Q$  and  $p$  in the study of Dubief and Delcayre[12], the CSs in the plane jet with  $Re = 2,000$ (TH) are visualized based on the iso-surfaces of  $p'$ , as shown in Figure 5.1, and the iso-surfaces of  $Q'$ , as shown in Figure 5.2, where  $p' = p/(\rho_0 U_b^2) = -0.1$ ,  $p'$  is the dimensionless value of the instantaneous pressure ( $p$ ), and  $\rho_0$  is the density of the flow medium;  $Q' = Q/(U_b^2/d^2) = 0.8$ ,  $Q'$  is the dimensionless second invariant of the velocity gradient tensor. In Figures 5.1 and 5.2, it represents  $5.0d$  per unit length, and the same unit length is used for the other figures in the following section.

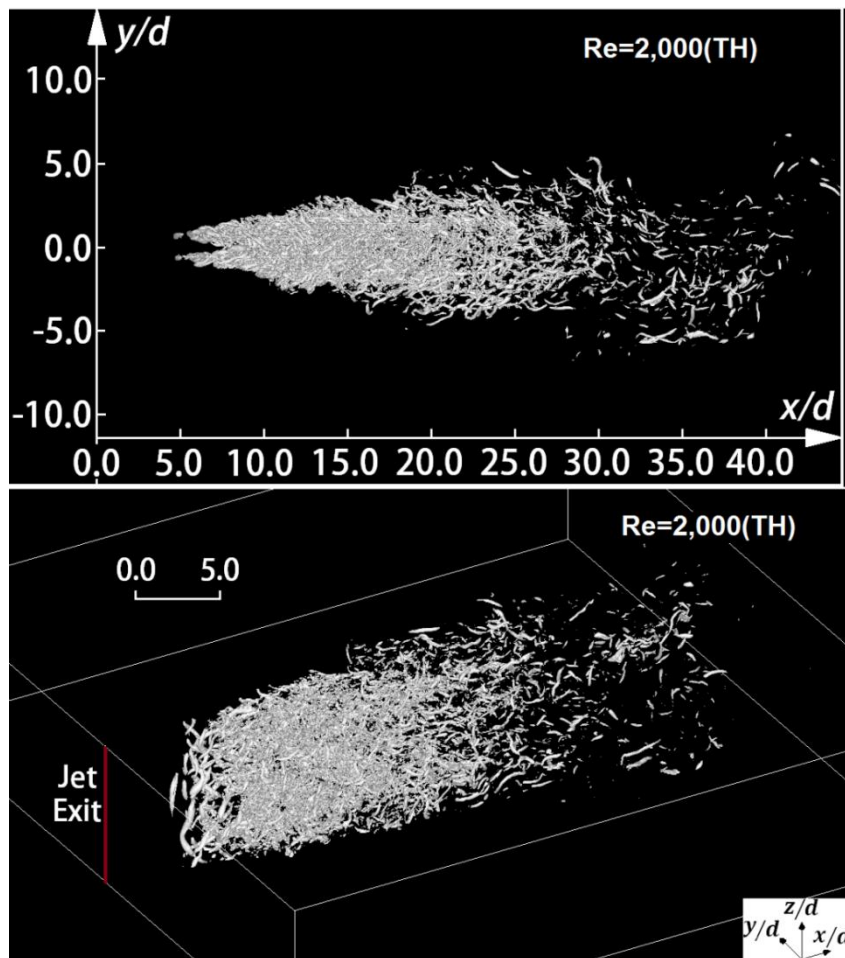


Figure 5.2 CS in the plane jet based on the isosurfaces of second invariant of velocity gradient tensor

The visualization results show that the isosurfaces of low pressure highlight the large-scale CSs near the jet exit, especially the big rollers in the spanwise direction which are the products of the Kelvin–Helmholtz vortices generated from the growth of

small perturbations induced by the initial velocity difference across the interface between the ambient flow and the plane jet. The isosurfaces of  $Q'$  show the small-scale CSs with smaller preferential spatial orientation compared to the large scales ones, most of which are spanwise and streamwise.

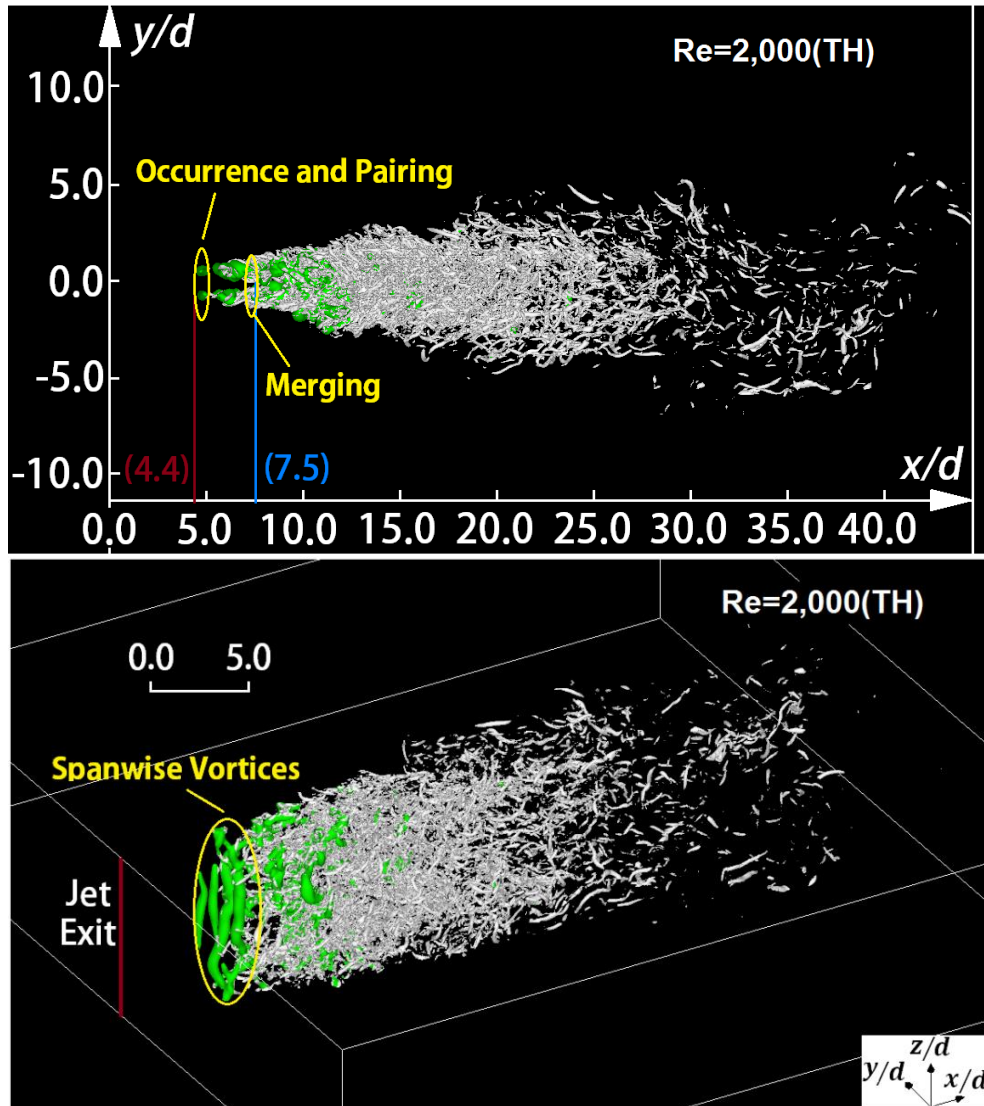


Figure 5.3 CS in the plane jet. Green structures show the isosurfaces of  $p'$ ; grey structures show the isosurfaces of  $Q'$

Figure 5.3 is the superposition of the results in Figures 5.1 and 5.2, which better presents the CSs with all kinds of scales in the plane jet. In Figure 5.3, the locations of the occurrence and merging of the CSs and the jet exit are separately marked. The results show that some pairing processes of the CSs exist because initial perturbations are two dimensional, and then three-dimensional perturbations triggered the helical

pairing of CS, which is characterized by staggered stretchings and local reconnections. The similar events were verified in the study on the plane mixing layer by Comte et al.[15]. In the downstream part including the fully developed region, the CSs keep small-scale structures and are distributed with random orientation.

### 5.3 Influence of Initial Condition on Coherent Structure

In this section, the same procedure of CS visualization is carried out in the other plane jets with different initial conditions. Figure 5.4 shows the CS with different exit Re and Figure 5.5 shows the CS with the parabola exit mean velocity profile, in which the locations of the occurrence and merging of CS and the jet exit are also marked. These results present the sequential appearance of the occurrence, the pairing, the merging, and the fracturing of CS with varying initial conditions.

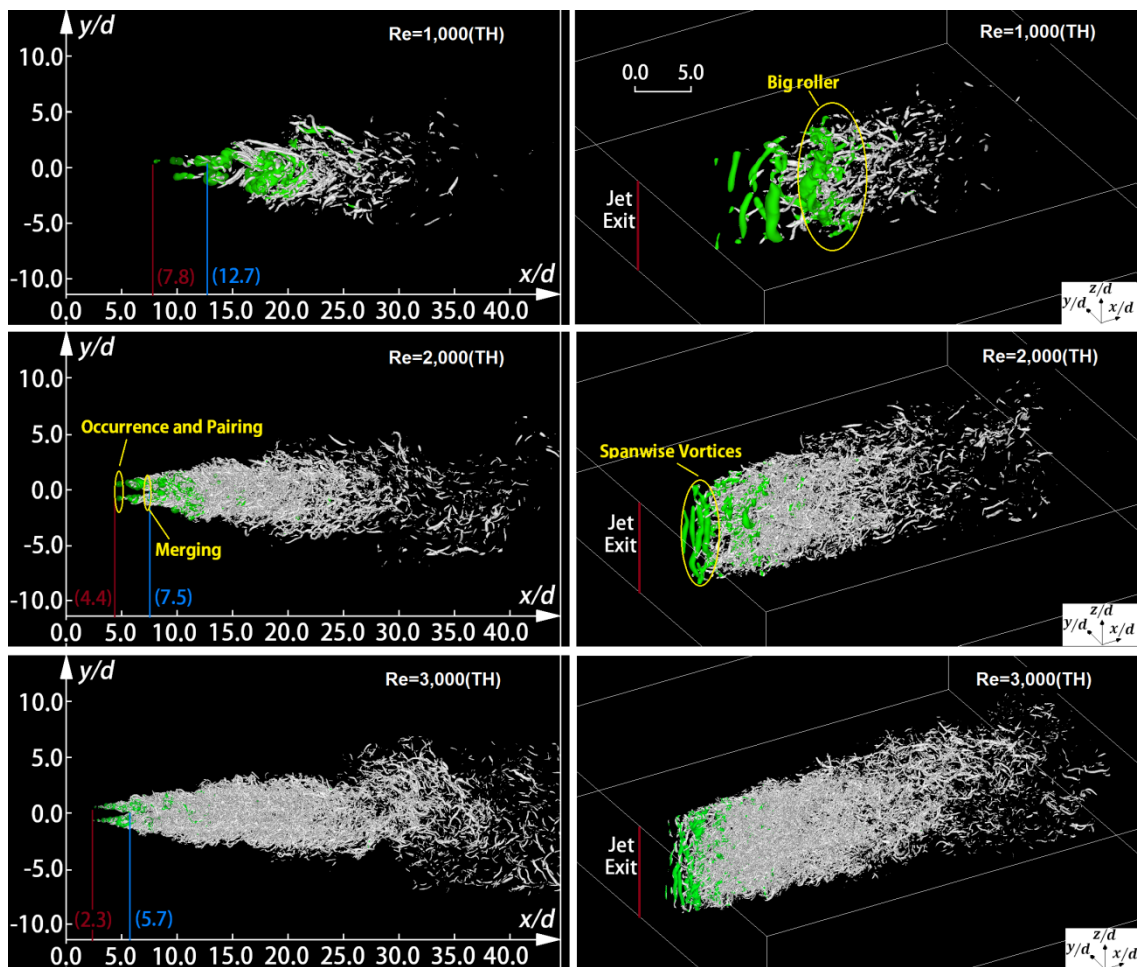


Figure 5.4 CS in plane jets with different exit Re

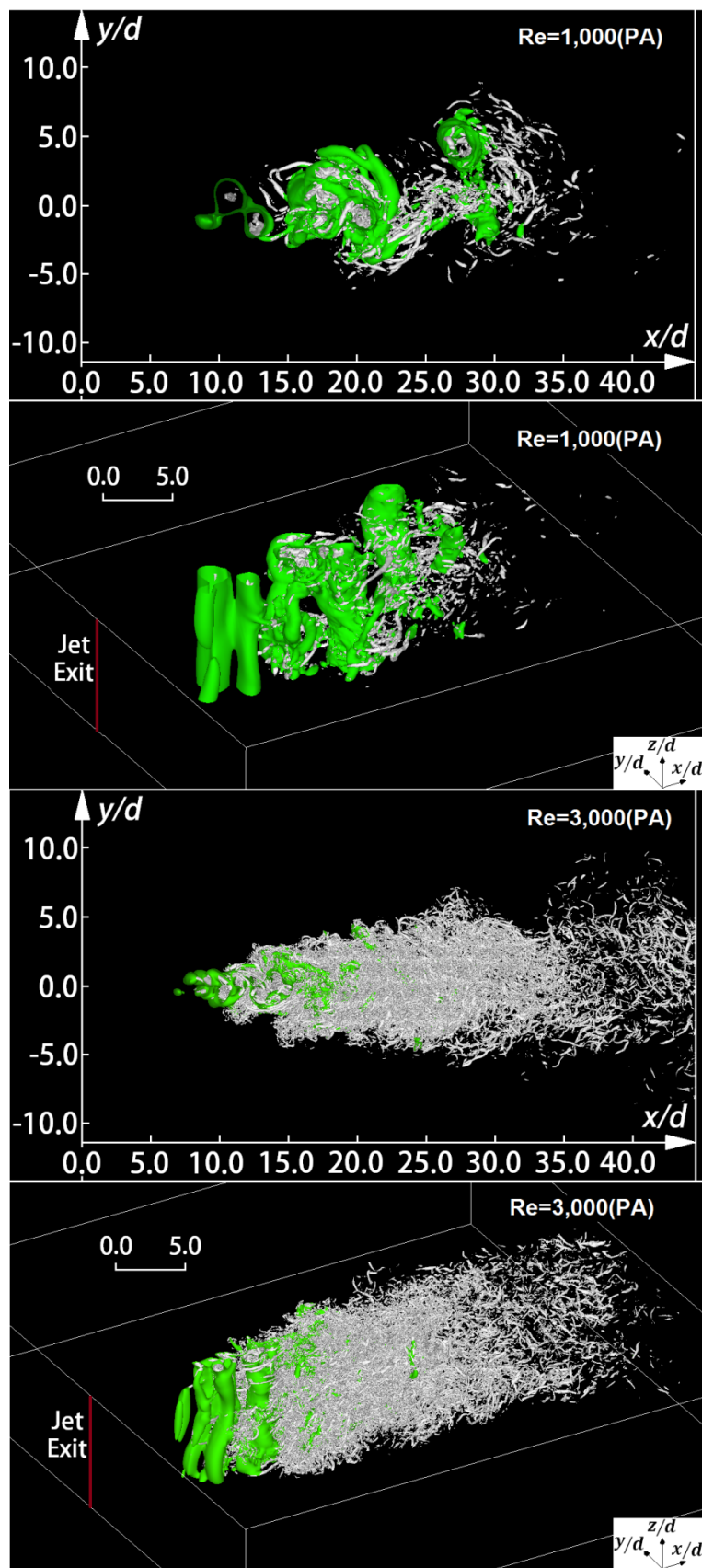


Figure 5.5 CS in plane jets with parabola exit mean velocity profile



First, in all cases the Kelvin–Helmholtz instability leads to the formation of the rolling up of the spanwise vortex structures, the rollers in the upper and lower two shear layers appear at the same time with opposite signs and form the typical dipole structure.

The exit  $Re$  dependency of the characteristics and behavior of CS is observed that the increase of the exit  $Re$  advances the occurrence and merging of CS, and in this situation the size of the large-scale CSs (green structures) becomes smaller. At the early stage of CS evolution, more organized and large vortices in the cases with low  $Re$  will strengthen the mixing between the plane jet and the ambient fluid, which corresponds to the larger decay rate of the mean velocity and scalar, seen in Figure 3.4, and the greater turbulent variables, seen in Figure 3.5.

The effects of the change of the exit mean velocity profile are studied based on the comparison of Figures 5.3 and 5.5. In the cases with PA, it is found hard to distinguish the locations of the occurrence and merging of CS, which is different from the cases with TH. One reasonable explanation is that the absence of the large velocity gradient between the jet and the co-flow in the cases with PA postpones the emergence of KH instability, which will help boost the initial CS. And it is quite obvious that the scale of CSs in the transition process of plane jets with PA is much larger than the ones with TH, which makes an explanation for the stronger turbulent behavior in the plane jets with PA in Chapter 4. In addition, in the cases with PA, exit  $Re$  shows the same effects on the scale of CSs as that in the cases with TH, i.e., larger scale CS exists with lower exit  $Re$ .

#### **5.4 Introduction to Turbulent/Non-turbulent Interface**

Entrainment exists in free shear flows such as mixing layers, wakes, and jets. In these flows, the flow field can be divided into two regions. One region is marked by the turbulence and high vorticity, and the other region is marked by the irrotational flow. These two regions are connected by the turbulent/non-turbulent (T/NT) interface, where the entrainment mechanism works. The T/NT interface plays an important role in the development of free shear flows, and the study on the characteristics of flows related to the T/NT interface will be especially helpful for understanding the nature of the turbulent entrainment.



The first step of the investigation on the T/NT interface is to define the location of the interface, where the vorticity and the passive scalar are testified to be the proper parameters to detect the interface. Mathew and Basu[16] studied the turbulent entrainment by searching for the possible differences between the entrainment in plane mixing layers and round jets, in which the vorticity was used to define the transition stage between the non-turbulent and turbulent state. Bisset et al.[17] also defined the T/NT interface for a far wake based on the vorticity, and the characteristics of velocity and temperature fields crossing the T/NT interface were investigated. Moreover, the detection of the T/NT interface based on the scalar was mainly used and proved to be effective in the turbulent jets by Prasad and Sreenivasan[18], and Westerweel et al.[19][20].

### 5.5 Turbulent/Non-turbulent Interface in Plane Jet

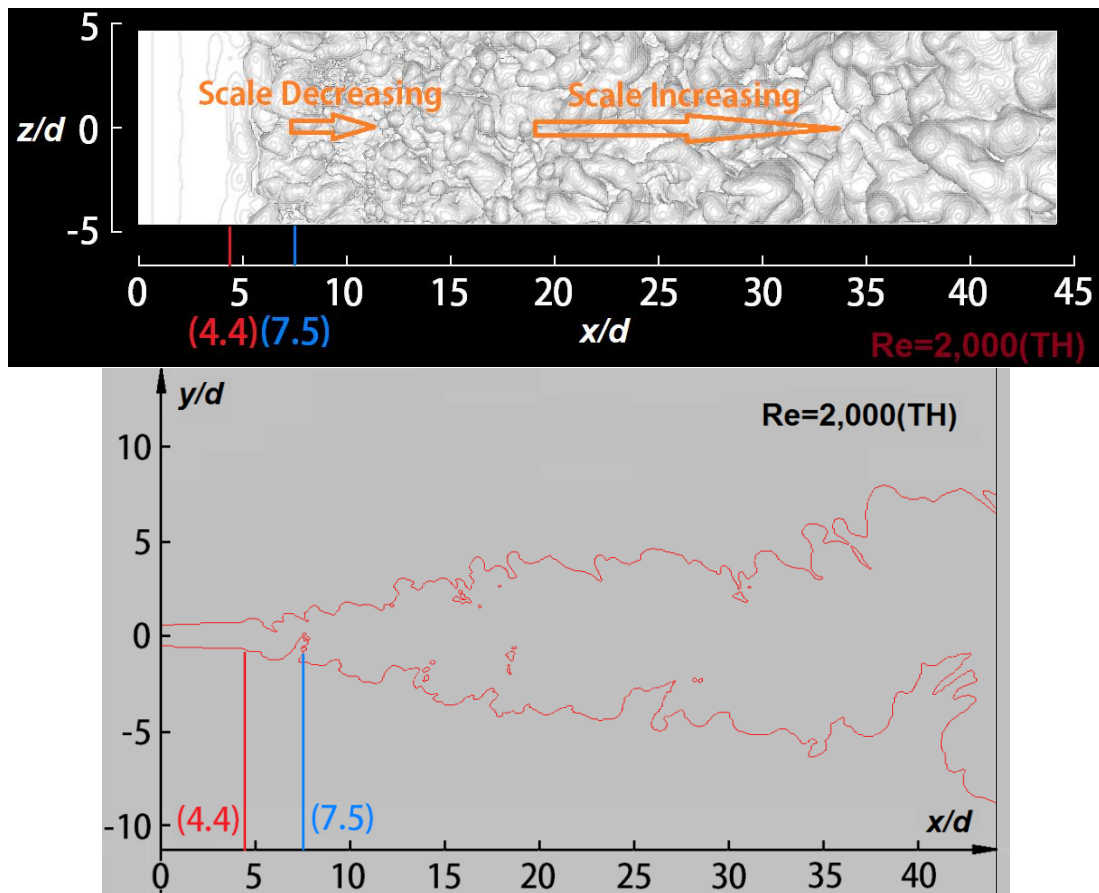


Figure 5.6 T/NT interface with  $Re = 2,000(TH)$ . (Top) Top view; (Bottom) side view.

Following the previous work, in the present study, the interface between the

plane jet and the ambient fluid will be defined based on the instantaneous scalar field, where the interface is defined and visualized by detecting a local minimum (0.1 in present work) of scalar value between the irrotational external flow, in which the scalar value is zero, and the jet flow region, in which the scalar value is larger than zero.

Figure 5.6 shows the interface between the plane jet and the ambient fluid in the case with  $Re = 2,000$ (TH), from the top view and the side view. And for scanning the relation between the CS and the interface, in Figure 5.6 the locations of the occurrence and merging of the CS, as seen in Figure 5.4, are also red-marked and blue-marked, separately.

By observing the characteristics of the contortion of the interface, it is illustrated that the initial development of the interface is stable in the region close to the jet exit, and then, two-dimensional development is induced at some location, close to which the first CS is detected. Afterwards, the jet develops three-dimensionally which causes the three-dimensional contortion of the interface. Furthermore, in the evolution of the interface it obviously presents complexity with a large range of length scales, which first decrease and then increase.

## 5.6 Influence of Initial Condition on Turbulent/Non-turbulent Interface

In this section, by visualizing the interface with different initial conditions, the effects of exit  $Re$  and mean velocity profiles on the characteristics and evolution of the interface are studied. These results are shown by Figures 5.7-5.9.

First, the influence of exit  $Re$  on the characteristics of the interface between the ambient flow and the plane jet shows some consistent features with that on the CS. The increase of Reynolds number advances the flow transition from laminar to turbulence, which can be detected by the faster build-up of the interface complexity; in the images with larger Reynolds number, a more contorted interface can be seen and interfaces retain a smaller scale, especially in the near field region behind the potential core.

In the cases with PA, based on the side view of the interface it presents that the lateral contortion is larger than that with TH at same exit  $Re$ . In addition, the increase of exit  $Re$  also advances the evolution of the interface, which is same as the effects of

exit Re in the cases with TH.

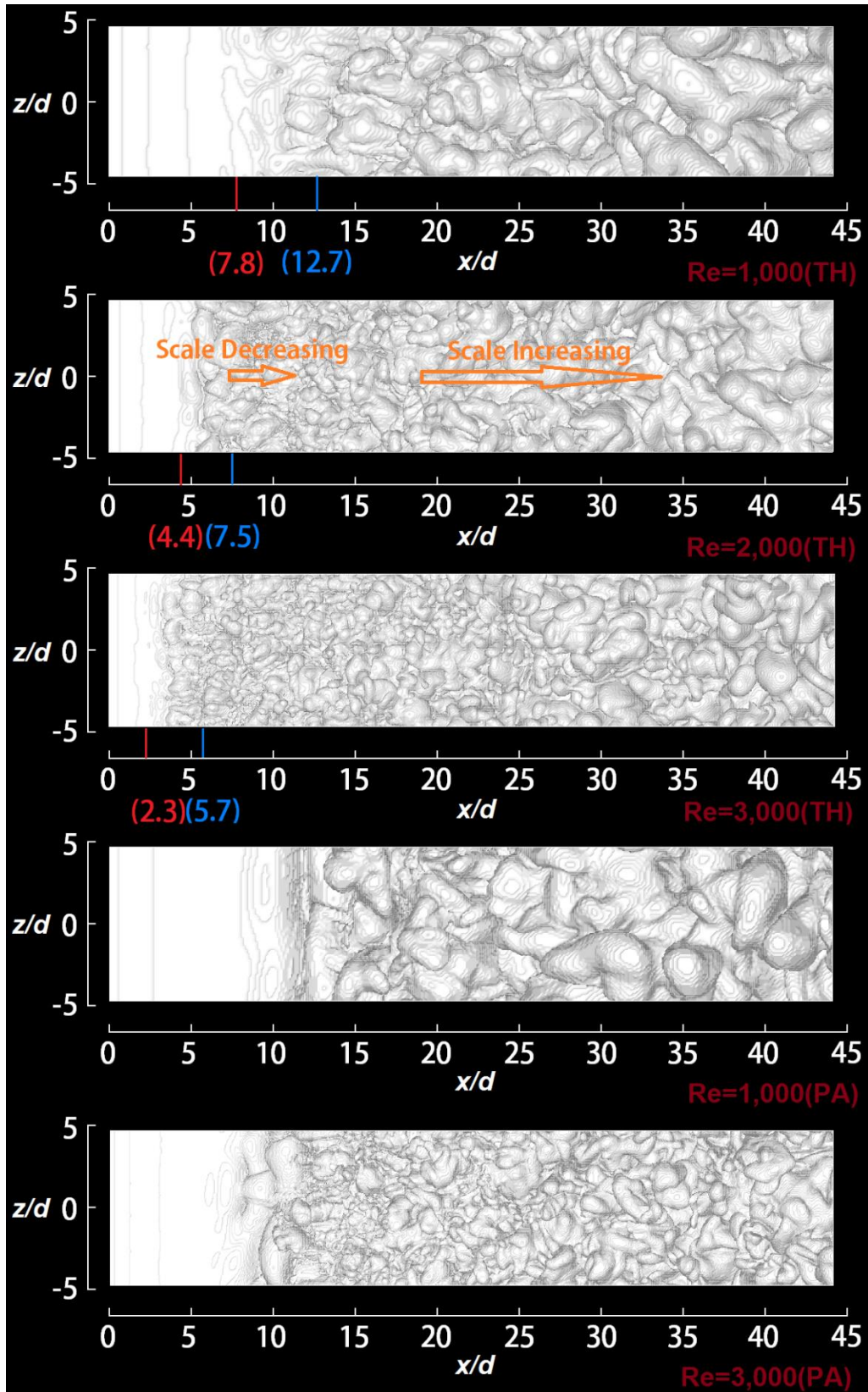


Figure 5.7 Top view of T/NT interface

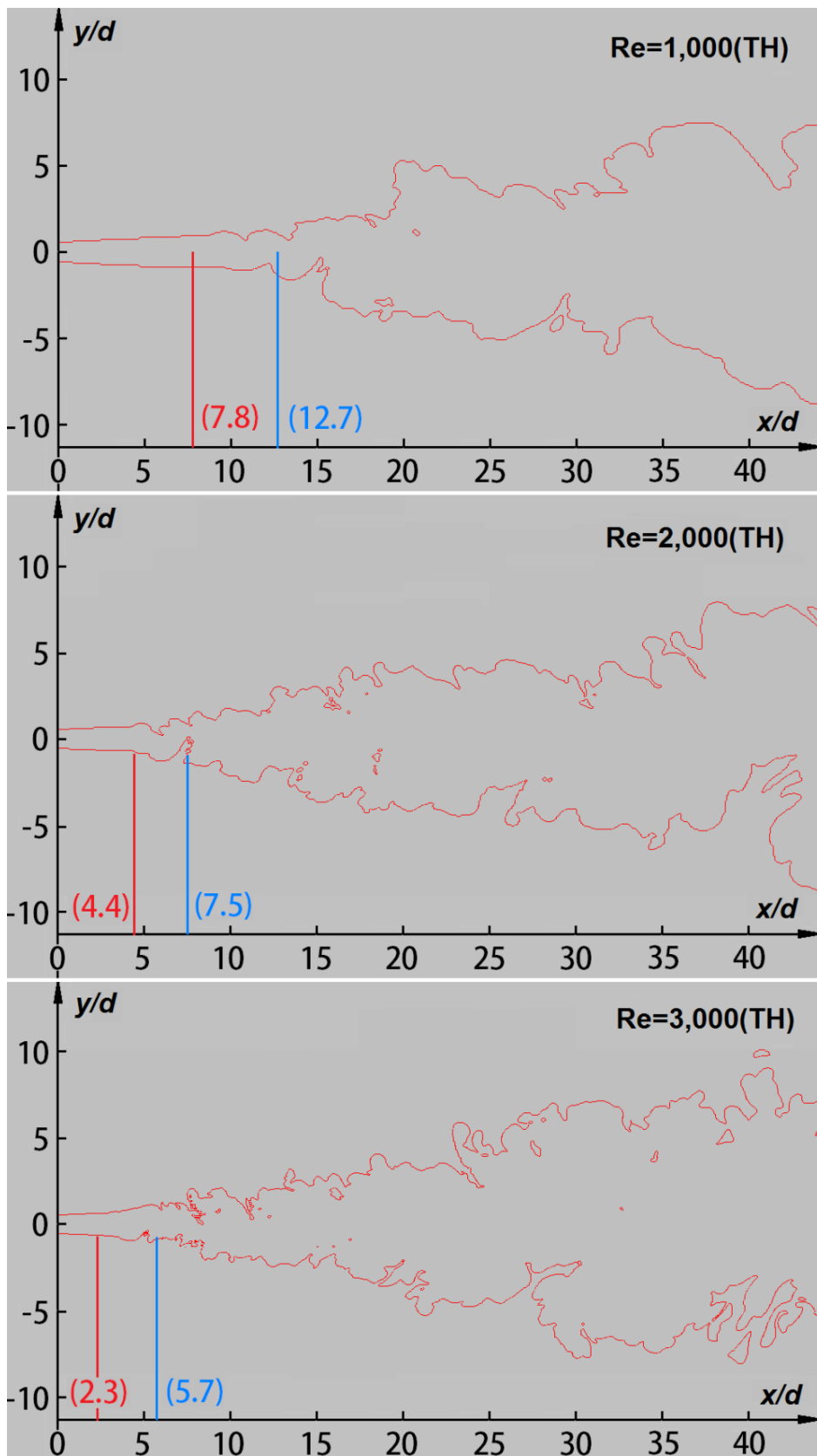


Figure 5.8 Side view of T/NT interface with different exit Re

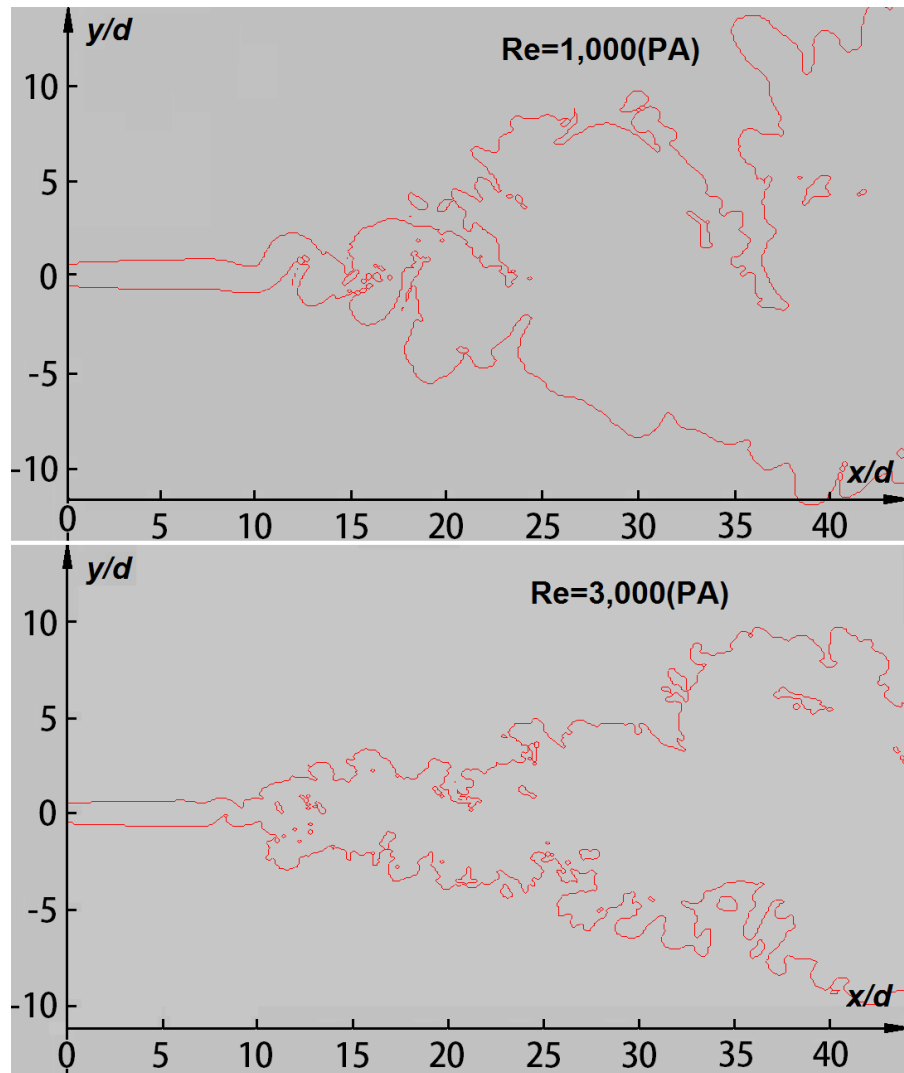


Figure 5.9 Side view of T/NT interface with parabola exit mean velocity profile

### 5.7 Conclusion

In this chapter, the information on the characteristics and evolution of CS and the T/NT interface, and the influence of exit Re and mean velocity profile on turbulence structures related to these two topics are provided. The process of occurrence, pairing and tearing of CS accompanying the flow evolution of turbulent plane jets are visualized on the basis of the instantaneous velocity and pressure data. The characteristics of CS are observed and discussed, especially in the near field region, which is barely studied in the past researches. Moreover, the interface between the plane jet and the ambient fluid is investigated using the data from the scalar field.

The main results in this chapter are summarized as follows:

1. The large-scale CSs detected by the local minimum of pressure are mainly spanwise and the small-scale CSs detected by the second invariant of velocity gradient are more three-dimensional.

2. The evolution of the interface between the plane jet and the ambient fluid corresponds to the evolution of the jet, which is initially two-dimensional and then three-dimensional.

3. The increase of exit  $Re$  advances the occurrence and merging of CS, and induces more small-scale CS in the downstream region, meanwhile, in the case with low exit  $Re$ , the CS in a larger scale can be detected.

4. In the case with large exit  $Re$ , the evolution of the interface is also accelerated, and the topology of interface is more complicated.

5. In the transition process the scale of CSs with PA is much larger than the ones with TH.

## References

- [1] WU N., SAKAI Y., NAGATA K., ITO Y., TERASHIMA O. and HAYASE T. Influence of Reynolds number on coherent structure, flow transition, and evolution of the plane jet[J]. *Journal of Fluid Science and Technology*, **2014**, 9(2): 14pages.
- [2] WU N., SAKAI Y., NAGATA K., SUZUKI H., TERASHIMA O. and HAYASE T. Effects of initial condition on coherent structure and evolution of turbulent plane jets[C]. *International Conference on Jets, Wakes and Separated Flows, Nagoya, Japan*, **2013**: ICJWSF2013-1010.
- [3] KLINE S. J., REYNOLDS W. C., SCHRAUB F. A. and PRNSTADLER P. W. The structure of turbulent boundary layers[J]. *Journal of Fluid Mechanics*, **1967**, 30(part4): 741-773.
- [4] BROWN G. L. and ROSHKO A. On density effects and large structure in turbulent mixing layers[J]. *Journal of Fluid Mechanics*, **1974**, 64(part4): 775-816.
- [5] BRADBURY L. J. S. The structure of a self-preserving turbulent plane jet[J]. *Journal of Fluid Mechanics*, **1965**, 23(part1): 31-64.
- [6] EVERITT K. W. and ROBINS A. G. The development and structure of turbulent plane jets[J]. *Journal of Fluid Mechanics*, **1978**, 88(part3): 563-583.

- [7] GUTMARK E. and HO C. M. Preferred modes and the spreading rates of jets[J]. *Physics of Fluids*, **1983**, 26(10): 2932-2938.
- [8] HUSSAIN A. K. M. F. Coherent structures – reality and myth[J]. *Physics of Fluids*, **1983**, 26(10): 2816-2850.
- [9] LESIEUR M. *Turbulence in Fluids*[M]. Dordrecht, The Netherland: Springer, **1997**: 6-7.
- [10] COMTE P., SILVESTRINI J. H. and BÉGOU P. Streamwise vortices in large-eddy simulations of mixing layers[J]. *European Journal of Mechanics – B/Fluids*, **1998**, 17(4): 615-637.
- [11] DUBIEF Y. and DELCAYRE F. On coherent-vortex identification in turbulence[J]. *Journal of turbulence*, **2000**, 1(1): N11.
- [12] JEONG J. and HUSSAIN F. On the identification of a vortex[J]. *Journal of Fluid Mechanics*, **1995**, 285: 69-94.
- [13] DA SILVA C. B. and METAIS O. On the influence of coherent structures upon interscale interactions in turbulent plane jets[J]. *Journal of Fluid Mechanics*, **2002**, 473: 103-145.
- [14] HUNT J. C. R., WRAY A. A. and MOIN P. Eddies, streams and convergence zones in turbulent flows[C]. *Proceeding of the Summer Program (Center for Turbulence Research)*, **1988**: 193-208.
- [15] COMTE P., LESIEUR M. and LAMBALLAIS E. Large- and small-scale stirring of vorticity and a passive scalar in a 3-D temporal mixing layer[J]. *Physics of Fluids A: Fluid Dynamics*, **1992**, 4(12): 2761-2778.
- [16] MATHEW J. and BASU A. J. Some characteristics of entrainment at a cylindrical turbulence boundary[J]. *Physics of Fluids*, **2002**, 14(7): 2065-2072.
- [17] BISSET D. K., HUNT J. C. R. and ROGERS M. M. The turbulent/non-turbulent interface bounding a far wake[J]. *Journal of Fluid Mechanics*, **2002**, 451: 383-410.
- [18] PRASAD R. R. and SREENIVASAN K. R. Scalar interfaces in digital images of turbulent flows[J]. *Experiments in Fluids*, **1989**, 7(4): 259-264.
- [19] WESTERWEEL J., HOFMANN T., FUKUSHIMA C. and HUNT J. C. R. The turbulent/non-turbulent interface at the outer boundary of a self-similar turbulent jet[J]. *Experiments in Fluids*, **2002**, 33(6): 873-878.
- [20] WESTERWEEL J., FUKUSHIMA C., PEDERSEN J. M. and HUNT J. C. R. *Mechanics of*

the turbulent-nonturbulent interface of a jet[J]. Physical Review Letters, **2005**, 95(17): 174501.

*[J]: Journal Article*

*[M]: Monograph*

*[C]: Conference Proceeding*



## Chapter 6

### INVARIANTS OF VELOCITY-GRADIENT, RATE-OF-STRAIN, AND RATE-OF-ROTATION TENSORS[1]

With the utilization of DNS, the dynamics, topology, and geometry of the plane jet in the fine scale can be investigated based on the analysis about the invariants of the velocity-gradient, rate-of-strain, and rate-of-rotation tensors. In this chapter, the evolution and characteristics of the invariants of the velocity-gradient, rate-of-strain, and rate-of-rotation tensors in the plane jets with different initial conditions are studied based on their joint probability density function (pdf) and some relevant statistics.

#### 6.1 Introduction

Up until almost 30 years ago, because the method about experimentally measuring the velocity gradient tensor was absent and the numerical simulation of the flow dynamics was only used tentatively, because the research on the parameters related to the velocity-gradient tensor was hard to conduct.

In 1985, the first numerical work, focusing on the properties of the small scales of turbulence defined by the velocity gradient tensor, was carried out to investigate an idealized isotropic turbulent flow based on the spectral method by Kerr[2]. In 1987, Balint et al.[3] measured the full velocity-gradient tensor in a turbulent boundary layer, using a miniature nine-sensor hot-wire probe. This is the first experimental work, in which the statistical data about the vorticity field and the full dissipation rate were provided. In the same year, the investigations on a turbulent channel flow by Kim et al.[4] and a temporally developing mixing layer by Metcalfe et al.[5] on the basis of the direct numerical simulation were published, which further developed the detailed

study of small scales in these important shear flows in view of the velocity gradient tensor.

Since the seminal work by Chong et al.[6], the study of turbulent flows based on the analysis of the invariants of the velocity-gradient tensor has attracted much more attention. The investigation on the properties of the invariants of the velocity-gradient tensor can illustrate the features of the flow motion in the fine scale, properly, which has been confirmed in the turbulent channel flow[7], the isotropic turbulence[8], the mixing layer[9], and the wake flow[10]. Da Silva et al.[11] analyzed the evolution of the invariants of the velocity-gradient tensor across the turbulent/nonturbulent interface in the self-preserving region of the plane jet, in which the kinematics, dynamics, and topology of the flow during the entrainment process were clarified.

According to the references, the transition process of the plane jet was barely evaluated based on the analysis of the invariants of the velocity-gradient tensor, meanwhile, the effects of initial condition on the plane jet have not been verified either from this topic. In the present work, presented in this chapter, the flow transition process in the spatially-developing plane jets and the effects of exit Re and mean velocity profile on the flow evolution are investigated in view of the invariants of the velocity-gradient, rate-of-strain, and rate-of-rotation tensors. The kinematics, dynamics and local structure of the plane jet in the fine-scale are studied by analyzing the evolution of the invariants of the velocity gradient tensor.

## 6.2 Definition and Physical Meaning

The dynamical behavior of the velocity gradient tensor is fundamentally important, which dominates the mechanism of the deformation of fluid elements and in turn is related to the energy cascade process in turbulence.

In this section, I first recall the definition and physical meaning of the invariants of the velocity gradient, rate-of-strain, and rate-of-rotation tensors.

The velocity gradient tensor  $A_{ij} = \partial u_i / \partial x_j$  can be split into two components, e.g., the symmetric  $S_{ij}$  and the skew-symmetric  $\Omega_{ij}$ , where  $S_{ij} = (\partial u_i / \partial x_j + \partial u_j / \partial x_i) / 2$  and  $\Omega_{ij} = (\partial u_i / \partial x_j - \partial u_j / \partial x_i) / 2$  are the rate-of-strain and rate-of-rotation tensors, respectively.

The characteristic equation for  $A_{ij}$  can be written as follows:

$$\lambda_i^3 + P\lambda_i^2 + Q\lambda_i + R = 0, \quad (6.1)$$

where  $\lambda_i$  are the eigenvalues of  $A_{ij}$ ,  $P$ ,  $Q$  and  $R$  are the first, second, and third invariants of  $A_{ij}$  respectively, which are written as the following formulae,

$$P = -\text{tr}(A_{ij}) = -S_{ii}, \quad (6.2)$$

$$Q = \frac{P^2 - \text{tr}(A_{ij}A_{ij})}{2} = \frac{(P^2 - S_{ij}S_{ij} + \Omega_{ij}\Omega_{ij})}{2}, \quad (6.3)$$

$$\begin{aligned} R &= -\det(A_{ij}) = (-P^3 + 3PQ - \text{tr}(A_{ij}A_{ij}A_{ij}))/3 \\ &= (-P^3 + 3PQ - S_{ij}S_{jk}S_{ki} - 3\Omega_{ij}\Omega_{jk}S_{ki})/3, \end{aligned} \quad (6.4)$$

Considering the incompressibility of the flow ( $P = 0$ ), the invariants of  $A_{ij}$  for the incompressible flow can be modified as

$$P = 0, \quad (6.5)$$

$$Q = \frac{(-S_{ij}S_{ij} + \Omega_{ij}\Omega_{ij})}{2}, \quad (6.6)$$

$$R = \frac{-S_{ij}S_{jk}S_{ki} - 3\Omega_{ij}\Omega_{jk}S_{ki}}{3}, \quad (6.7)$$

where  $Q$  can be divided into the strain component ( $Q_s = -S_{ij}S_{ij}/2$ ), and the rotation component ( $Q_w = \Omega_{ij}\Omega_{ij}/2$ ); and  $R$  is composed of the strain component ( $R_s = -S_{ij}S_{jk}S_{ki}/3$ ) and  $-\Omega_{ij}\Omega_{jk}S_{ki}$ .

Following the above definition for each parameter, the modulus of the second invariant of the rate-of-strain tensor  $Q_s$  is proportional to the local rate of viscous dissipation of kinetic energy  $\varepsilon = 2\nu S^2 = -4\nu Q_s$ , where  $S^2/2 = S_{ij}S_{ij}/2$  is the strain product; the second invariant of the rate-of-rotation tensor  $Q_w$  is proportional to the enstrophy density  $\Omega^2/2 = \Omega_{ij}\Omega_{ij} = 2Q_w$ ; the modulus of the third invariant of the rate-of-strain tensor  $R_s$  is proportional to the strain skewness  $S_{ij}S_{jk}S_{ki}$ . Moreover, it is known that  $-S_{ij}S_{jk}S_{ki}$  is part of the production term in the strain product transport equation[12], which implies that a positive value of  $R_s$  is related to the production of strain product, whereas a negative value of  $R_s$  corresponds to the destruction of strain product.

The values of the invariants are independent of the orientation of the coordinate system and contain the information concerning the rates of vortex stretching and rotation, and the topology and geometry of deformation of the infinitesimal fluid elements. Based on the analysis of the invariants, the topology of the flow (enstrophy dominated versus strain dominated) or the enstrophy production (vortex stretching versus vortex compression) can be observed with the utilization of a relatively small number of variables, e.g. the second and third invariants of the velocity gradient tensor.

### 6.3 Results and Discussion

#### 6.3.1 Joint Pdfs of the Velocity Gradient Tensor Invariants

In this section, the local structure of the joint pdfs of invariants at several locations along the jet centerline is observed in order to assess the evolution of the geometry of flow motions along with the flow transition in the plane jet.

The approach taken in DNS was to compute the second and third invariants of the velocity gradient, rate-of-strain, and rate-of-rotation tensors at each grid point and time step in the computational domain first. And then the calculation of the joint pdfs of the invariants are made at three locations at the jet centerline, which are  $x/d = 0.5$ ,  $x/d = 13.0$ , and  $x/d = 37.0$ . At each location, the joint pdfs are computed based on the average of the values of the invariants at 5,000 time steps and  $5(y) \times 5(z)$  grid points centered at the jet centerline.

The evaluation of the effects of initial condition on the invariants is carried out based on the cases with  $Re = 1,000(\text{TH})$ ,  $Re = 1,000(\text{PA})$ ,  $Re = 3,000(\text{TH})$ , and  $Re = 3,000(\text{PA})$ .

##### 6.3.1.1 Joint Pdfs of $(Q_w, -Q_s)$

The invariant map of  $(Q_w, -Q_s)$  is shown in Figure 6.1, which can be used to analyze the geometry of the dissipation of kinetic energy[12]. The horizontal line, defined by  $-Q_s = 0$ , represents flow elements with high enstrophy but very small dissipation, as the solid body rotation at the center of a vortex tube. On the other hand, the vertical line, defined by  $Q_w = 0$  represents flow elements with high dissipation but little enstrophy density, which corresponds to the flow elements

containing strong dissipation outside and away from the vortex tubes, just as the irrotational dissipation. Moreover, the line angling  $45^\circ$  with the vertical and horizontal lines, at which  $Q_w = -Q_s$ , and it represents the flow elements with high dissipation accompanied by high enstrophy density, which is consistent with the vortex sheet structures.

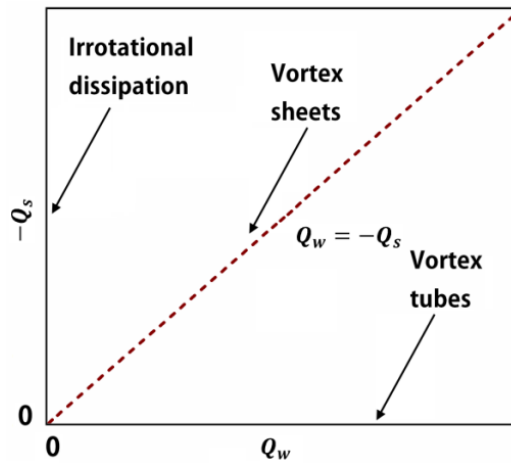


Figure 6.1 Sketch of the invariant map of  $(Q_w, -Q_s)$

Figure 6.2 shows the joint pdfs of  $(Q_w, -Q_s)$  at three typical locations along the jet centerline in all four kinds of initial conditions, in which the invariants are normalized by  $\langle S_{ij}S_{ij} \rangle$ , which is the average of all sampling data at all typical locations; the shown values of probability density vary from 0.01% to 15.00%.

On the basis of the results at  $Re = 1,000(PA)$ , firstly the evolution of the geometry of the dissipation in the flow transition process is investigated. At the location  $x/d = 0.5$ , which is close to the jet exit, the obvious tendency for all levels of the probability density is observed to align with the vertical line defined by  $Q_w = 0$ , which attests a strong predominance of dissipation over enstrophy in this region for all the scales of flow motion. Meanwhile,  $Q_w$  integrally possesses the smaller value than  $Q_s$ , which reveals the absence of the solid body rotation.

The flow at the location  $x/d = 13.0$  contains larger values of  $Q_w$  than the flow at the previous location  $x/d = 0.5$ , which illustrates the growth of vortex tubes, especially at the levels of small probability density.

With regard to the flow elements at the location of  $x/d = 37.0$ , the contour lines, associated with the most frequent values of  $Q_w$  and  $Q_s$ , present the tendency

aligning with the vertical line defined by  $Q_w = 0$ ; however, the contour lines for the most intense values of  $Q_w$  and  $Q_s$ , with small probability densities, show the tendencies, aligning not only with the vertical line defined by  $Q_w = 0$  but also with the horizontal line defined by  $-Q_s = 0$ .

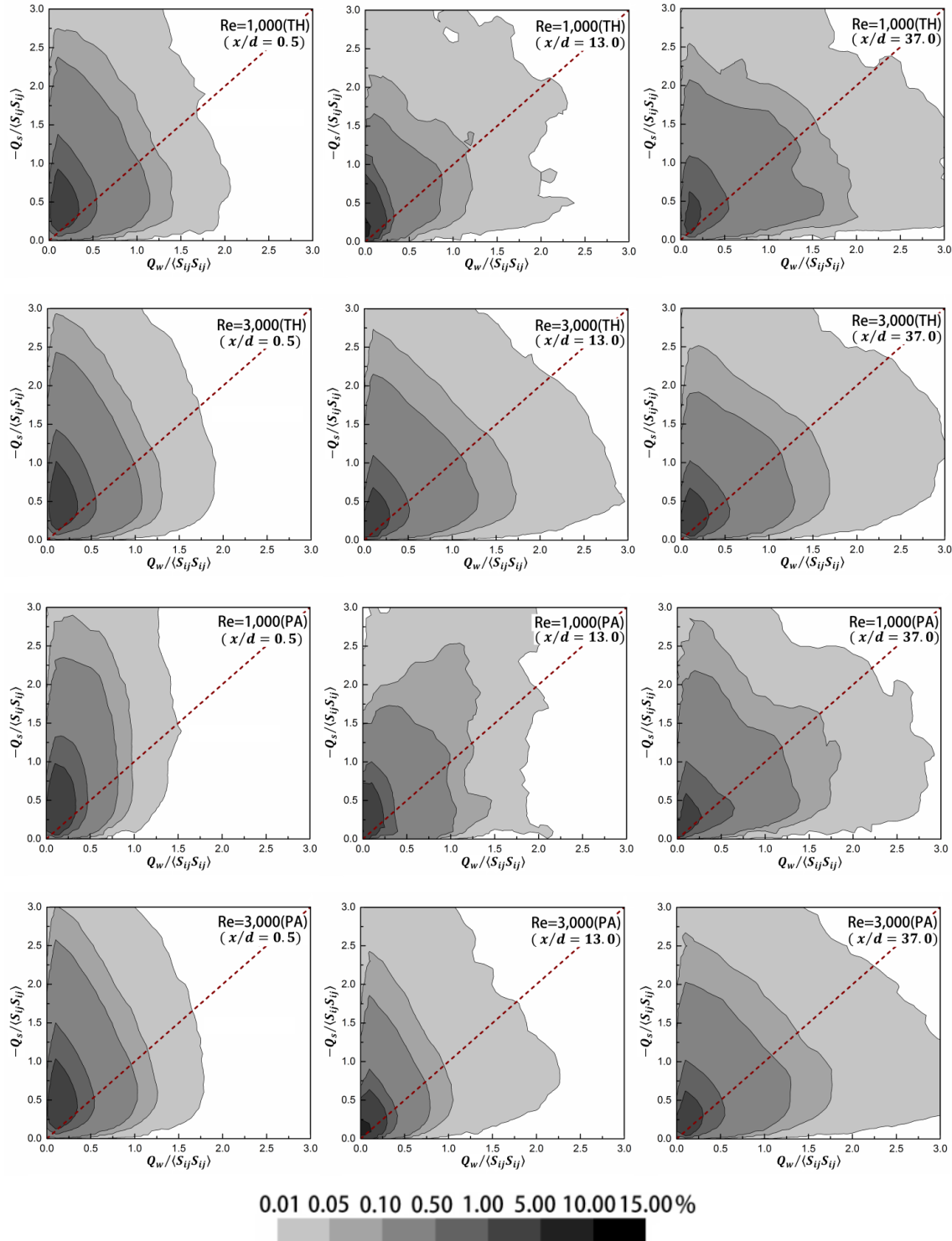


Figure 6.2 Joint pdfs of  $(Q_w, -Q_s)$

In the flow transition process, the characteristics of joint pdfs of  $(Q_w, -Q_s)$  reveal most of the flow domain has small velocity gradients, which can be confirmed by the largest values of the joint pdfs lying around the origin,  $(Q_w = 0, -Q_s = 0)$ . In the downstream region of the plane jet, where the flow approaches to the fully-developed state, the vortex tubes with solid body rotation and little kinetic energy dissipation exist but as the rare events. In addition, the results point to a topology in the fully-developed plane jet, which is characterized by the coexistence of vortex tubes, vortex sheets, and zones of irrotational dissipation but that the irrotational dissipation with small velocity gradient dominates in the flow.

Moreover, as the exit Re increases from 1,000 to 3,000, the shape of the joint pdfs map at  $x/d = 13.0$  and  $x/d = 37.0$  shows better similarity, which confirms the faster transition to the typical dissipation geometry in the fully-developed state of the plane jet. Meanwhile, the stronger tendency towards the irrotational dissipation at  $Re = 1,000(PA)$  supplies the answer to nonzero mean velocity decay near the jet exit, shown by Figures 4.6 and 4.7.

6.3.1.2 Joint Pdfs of  $(R, Q)$

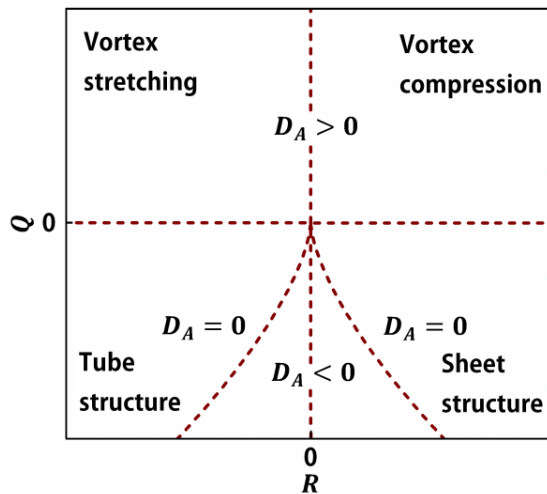


Figure 6.3 Sketch of the invariant map of  $(R, Q)$

On the basis of the definitions of  $Q$  and  $R$ , firstly, the sign of  $Q$  illustrates the physical nature of fluid elements. With the positive  $Q$ , the enstrophy dominates over the strain product, whereas, with the negative  $Q$ , the strain product is larger than the enstrophy. Secondly, after the sign of  $Q$  is determined, the meaning of  $R$  can be

inferred. If  $Q \ll 0$ ,  $R \approx R_s = -S_{ij}S_{jk}S_{ki}/3$ , therefore, the positive  $R$  is related to the production of strain product with the sheet structure, whereas, the negative  $R$  is related to the destruction of strain product with the tube structure. If  $Q \gg 0$ ,  $R \approx -\Omega_{ij}\Omega_{jk}S_{ki}$ , the positive  $R$  implies the vortex is more compression than stretching, whereas, the vortex stretching is dominant with the negative  $R$ . The above four cases are shown in Figure 6.3[12].

The  $(R,Q)$  map will assist us in analyzing the relation between the local flow topology (enstrophy or strain dominated) and the strain production term (vortex stretching or vortex compression), which is associated geometry of the deformation of the fluid elements (contraction or expansion).

The tent-like curve in Figure 6.3 is the line defined by  $D_A = 0$ , where  $D_A$  is the discriminant of  $A_{ij}$  given by

$$D_A = 27/4 R^2 + Q^3 \quad (6.8)$$

The joint pdfs of  $(R,Q)$  are shown by Figure 6.4, where the invariants are also normalized by  $\langle S_{ij}S_{ij} \rangle$ , and the contour levels are set same as Figure 6.2.

The analysis of Figure 6.4 is also based on the condition  $Re = 1,000(PA)$ . At the location  $x/d = 0.5$ , the joint pdfs show the symmetrical shape along the vertical line, defined by  $R = 0$ , with narrow top and wide bottom. The symmetrical distribution of  $R$  implies the equilibrium between vortex stretching and vortex compression as well as between tube structure and sheet structure; in addition, the predominance of the strain product over the enstrophy can be captured because the joint pdfs below the horizontal line, defined by  $Q = 0$ , keep larger area.

At location  $x/d = 13.0$ , the transformation into the characteristic teardrop shape of the joint pdfs contour starts from the parts with small probability densities and intense values of  $R$  and  $Q$ , and the bottom part of the contours is transformed more obviously, which reveals the evolution of the fluid elements deformation is faster than the evolution of the vortex structure in the transition process of the plane jet.

When the flow arrives at the location  $x/d = 37.0$ , the  $(R,Q)$  map presents the characteristic teardrop shape, where we can observe the strong anti-correlation in the regions  $(R > 0, Q < 0)$  and  $(R < 0, Q > 0)$ . The teardrop shape represents the dominant sheet structure and enstrophy production by vortex stretching, which is at



the core of the description of the turbulence energy cascade from the large scales to the small scales in the fully-developed turbulence.

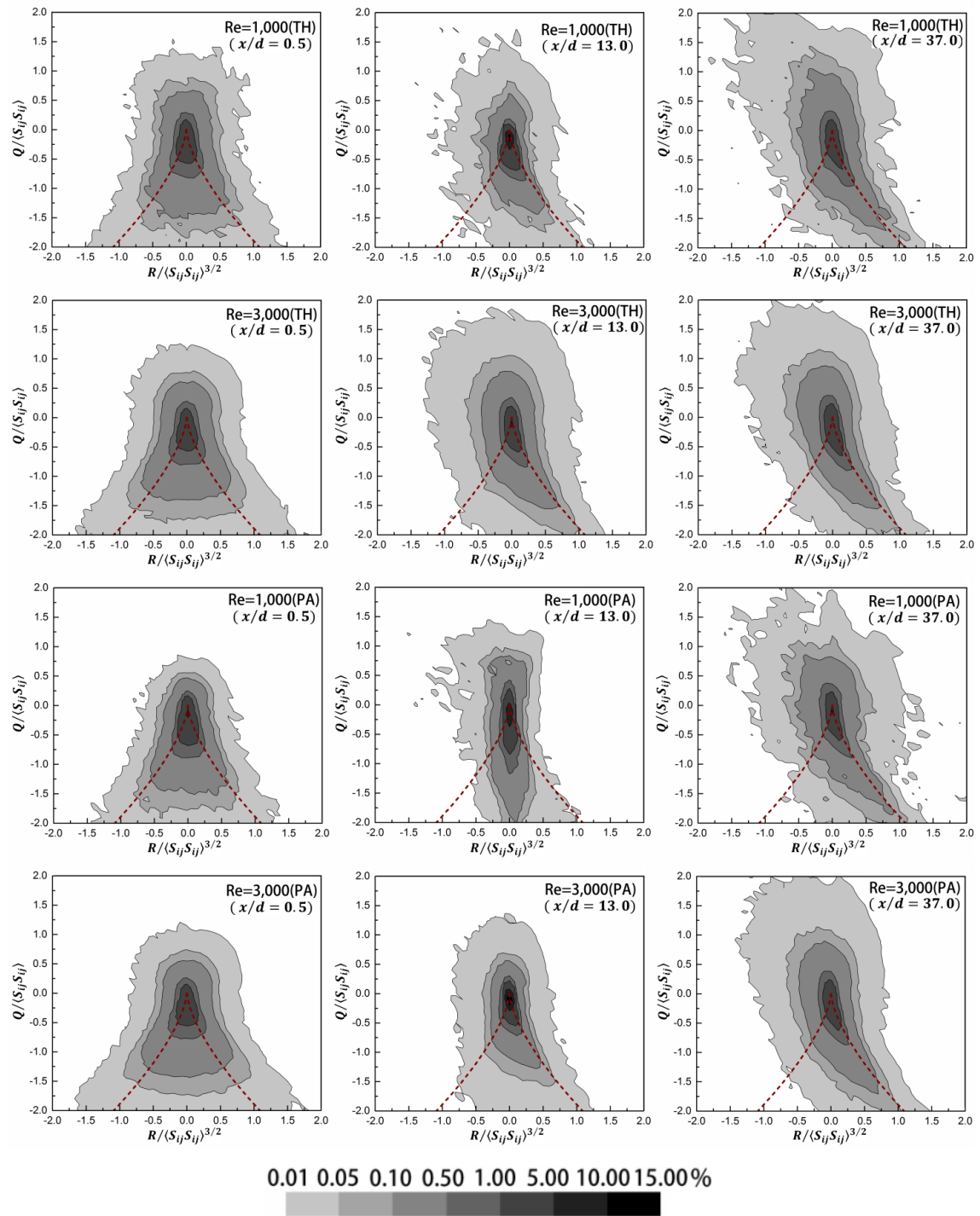


Figure 6.4 Joint pdfs of  $(R, Q)$

Following the observation about the effects of initial condition on the joint pdfs of  $(Q_w, -Q_s)$ , likewise, the results of the joint pdfs of  $(R, Q)$  show that the flow transition

is faster with the large exit  $Re$  and in the case with  $Re = 1,000(PA)$  the dissipation of kinetic energy is intenser. Moreover, another point tending to be clearer is that, if I make a comparison between  $Re = 3,000(TH)$  and  $Re = 3,000(PA)$  at the location  $x/d = 13.0$ ,  $Q$  presents more large positive values. The shape of contours is more similar between  $x/d = 13.0$  and  $x/d = 37.0$  at  $Re = 3,000(TH)$  than  $Re = 3,000(PA)$ . This implies the top hat profile for the mean velocity at the jet exit will advance the transition of the local geometry and topology of the fluid elements in the plane jet.

### 6.3.1.3 Joint Pdfs of $(R_s, Q_s)$

$R_s$  and  $Q_s$  are the third and second invariants of the rate-of-strain tensor  $S_{ij}$  respectively, which inspires us that the  $(R_s, Q_s)$  map will be useful to analyze the geometry of the local straining (or deformation) of the fluid elements.

Since  $Q_s = -\varepsilon/4\nu$ , the  $Q_s$  with large negative value is associated with the intense kinetic energy dissipation. In addition, the deformation of the fluid element can be elucidated according to the sign of  $R_s$ , the positive value of  $R_s$  implies the expansion of the fluid element, where the local straining is enhanced, whereas, the destruction of the strain product is with the negative value of  $R_s$ , which follows the contraction of the fluid element.

Here,  $\alpha_s$ ,  $\beta_s$  and  $\gamma_s$  are defined to be the eigenvalues of  $S_{ij}$ , ordered as  $\alpha_s \geq \beta_s \geq \gamma_s$ , and then  $R_s$  can be written as  $-\alpha_s\beta_s\gamma_s$ , and the sign of  $R_s$  will accord with the sign of  $\beta_s$ . Due to the incompressibility,  $\alpha_s + \beta_s + \gamma_s = 0$  is valid, and hence  $R_s > 0$  implies that  $\alpha_s, \beta_s > 0$  and  $\gamma_s < 0$ , whereas,  $R_s < 0$  implies that  $\alpha_s > 0$  and  $\beta_s, \gamma_s < 0$ .

The invariant map of  $(R_s, Q_s)$  is shown by Figure 6.5, in which five red dash lines are drawn on the basis of several typical values of the eigenvalues of  $S_{ij}$  and the discriminant of  $S_{ij}$ , which is  $D_s = 27/4 R_s^2 + Q_s^3$ . Each line in the map is associated with a given flow geometry:  $\alpha_s:\beta_s:\gamma_s = 2:-1:-1$  (axisymmetric contraction),  $1:0:-1$  (two-dimensional flow),  $3:1:-4$  (biaxial stretching), and  $1:1:-2$  (axisymmetric stretching)[12].

Based on the joint pdfs of  $(R_s, Q_s)$  shown by Figure 6.6, the geometry of the straining of the fluid elements is analyzed. Taking  $Re = 1,000(PA)$  to be an example,

at the location  $x/d = 0.5$ , the joint pdfs are symmetrical along the line  $(1:0:-1)$ , it reveals that the deformation of flow elements shows no preference here; and all the shapes are with a wide bottom which implies large dissipation dominates at all levels of flow motion.

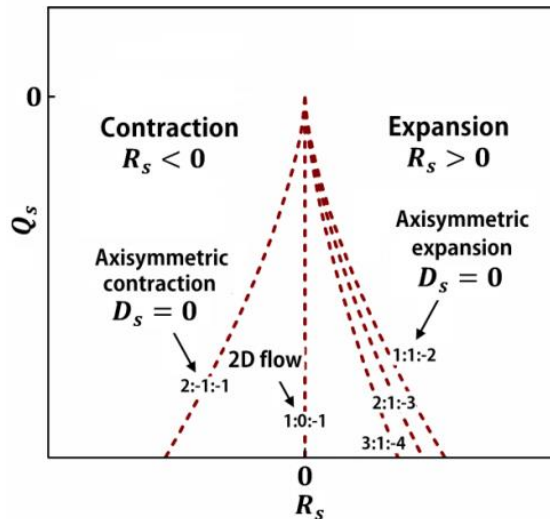


Figure 6.5 Sketch of the invariant map of  $(R_s, Q_s)$

The results at the location  $x/d = 13.0$  show the transformation of the joint pdfs also starts from the contour line with the large probability density. And the expansion gradually predominate the contraction, and in this process the local straining is continually enhanced.

The  $(R_s, Q_s)$  map at the location  $x/d = 37.0$  shows a strong preference for the zone  $(R_s > 0, Q_s < 0)$ , which indicates a predominance of sheet structures associated with expansive straining of the fluid elements, although contractive straining also exists at some much fewer points. Figures 6.7 and 6.8 are presented to be the supplement of Figure 6.6, the results in them show that the most probable geometry of the fluid elements corresponds to a geometry between 3:1:-4 (biaxial stretching) and 1:1:-2 (axisymmetric stretching).

At the location  $x/d = 0.5$ ,  $R_s$  possesses some larger value at the large exit Re, which illustrates stronger contraction or expansion of the fluid elements occurs near the jet exit in this condition.

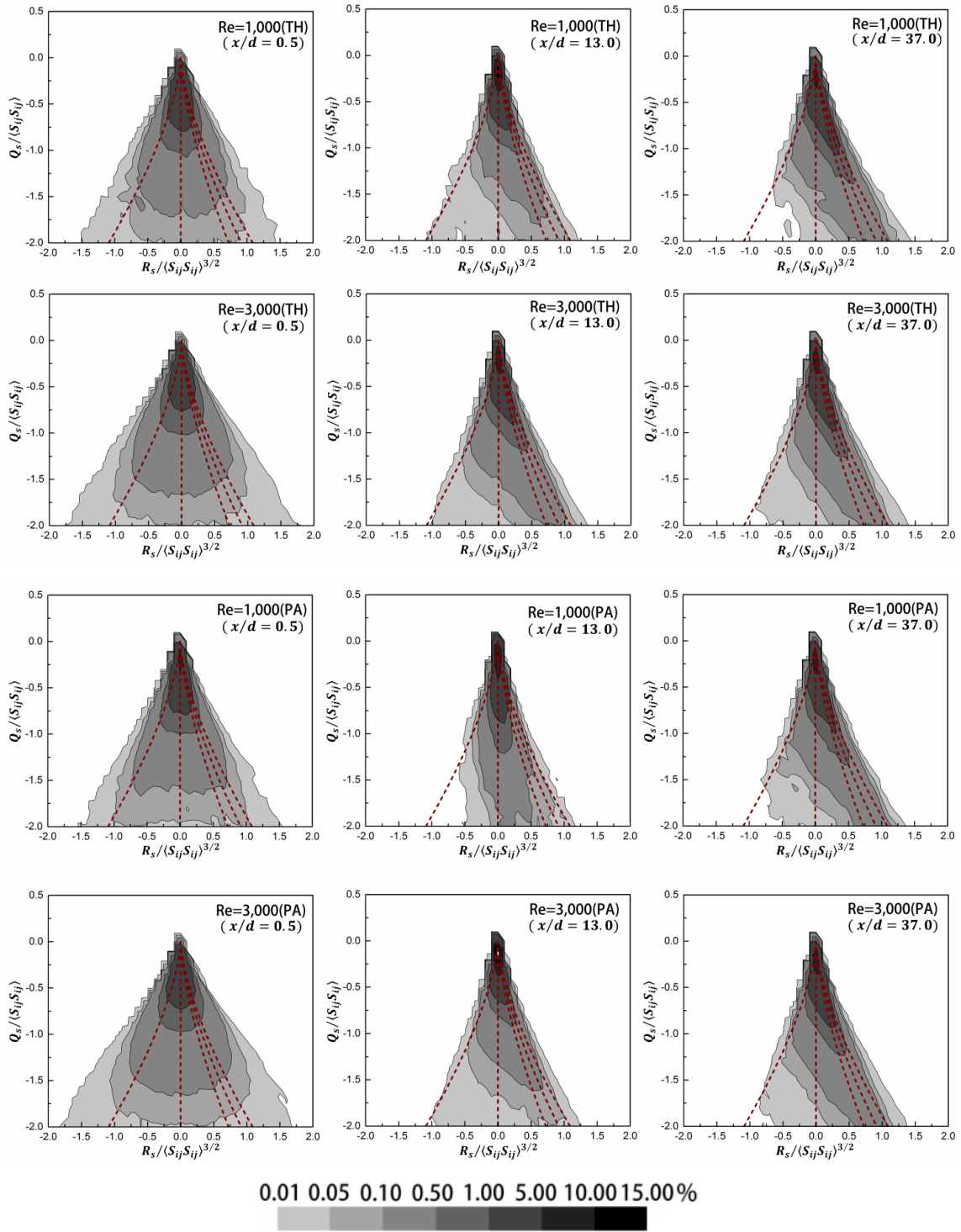


Figure 6.6 Joint pdfs of  $(R_s, Q_s)$  - (1)

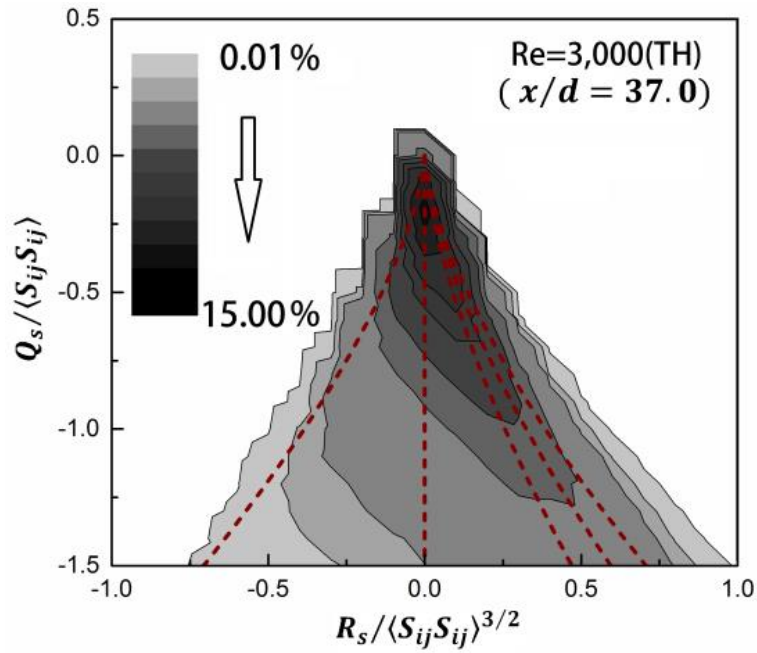


Figure 6.7 Joint pdfs of  $(R_s, Q_s)$  - (2)

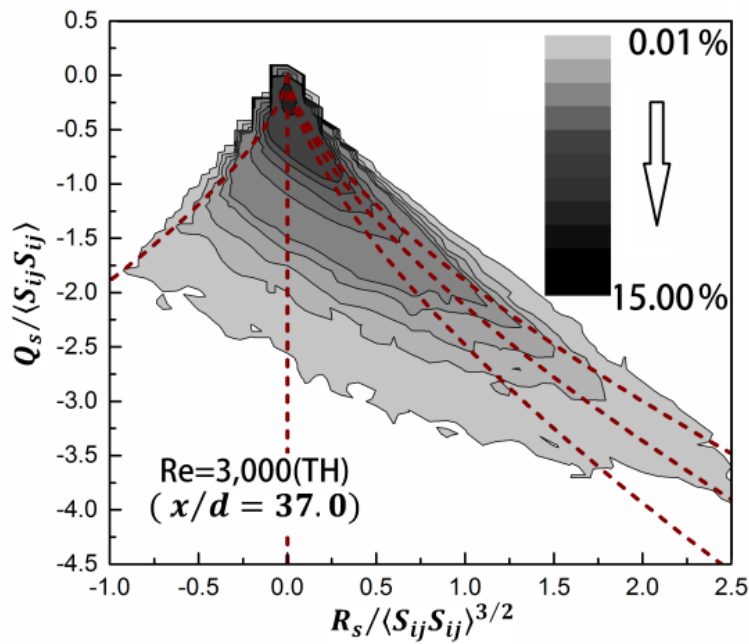


Figure 6.8 Joint pdfs of  $(R_s, Q_s)$  - (3)

### 6.3.2 Velocity Gradient Tensor Invariants along the Jet Centerline

This section shows the evolution of the invariants of the velocity gradient tensor along the jet centerline by Figure 6.9 for  $\langle Q_w \rangle$ , Figure 6.10 for  $\langle -Q_s \rangle$ , Figure 6.11 for  $\langle R \rangle$ , and Figure 6.12 for  $\langle R_s \rangle$ , which are normalized by  $U_b^2/d^2$  and  $U_b^3/d^3$

respectively. The statistics at each location of the jet centerline are calculated based on the average of the value of the variables at 5,000 time steps.

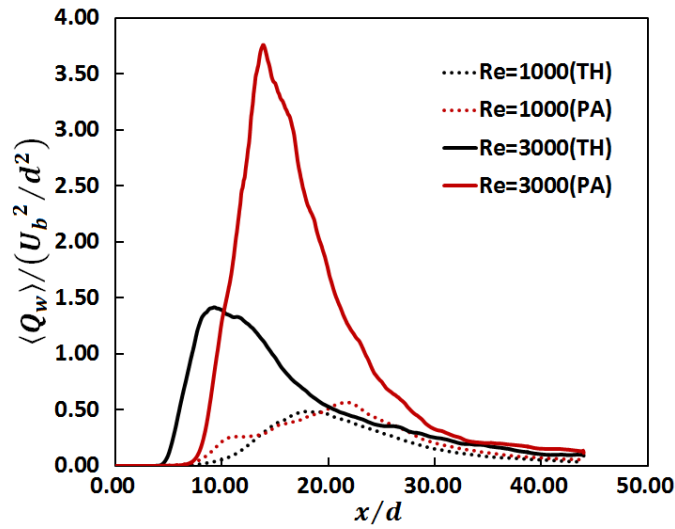


Figure 6.9 Profile of  $\langle Q_w \rangle$  along the jet centerline

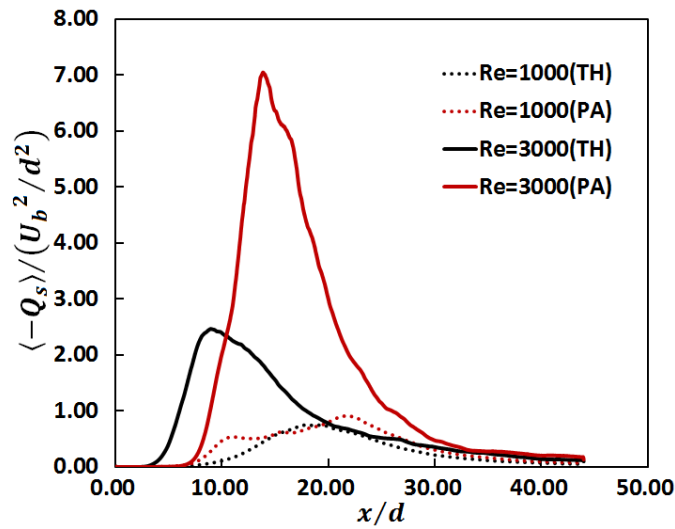


Figure 6.10 Profile of  $\langle -Q_s \rangle$  along the jet centerline

The curves in these four figures show similar behavior. Near the jet exit, the invariants present zero value, and it implies the absence of the velocity gradient, which is the general property in the potential core. The most remarkable values occur in the flow transition process, it reveals that the flow transition is accompanied by the severe rotation and straining of the flow elements. In the downstream region of the plane jet, the flow shows small magnitude for the second invariants, which is corresponding to

the more homogeneous and isotropic state there; meanwhile the third invariants are zero, which means the probability density for the negative  $R$  and  $R_s$  is same to the probability density for the positive ones. Moreover,  $Q_s$  almost predominates over  $Q_w$  in the whole development process of the plane jet, observed by the comparison of Figure 6.9 and Figure 6.10.

It is quite obvious that large exit Re and parabola profile for the exit mean velocity enhance the maxima of the invariants. Re = 3,000(TH) seems to lead to the fastest transition of the flow.

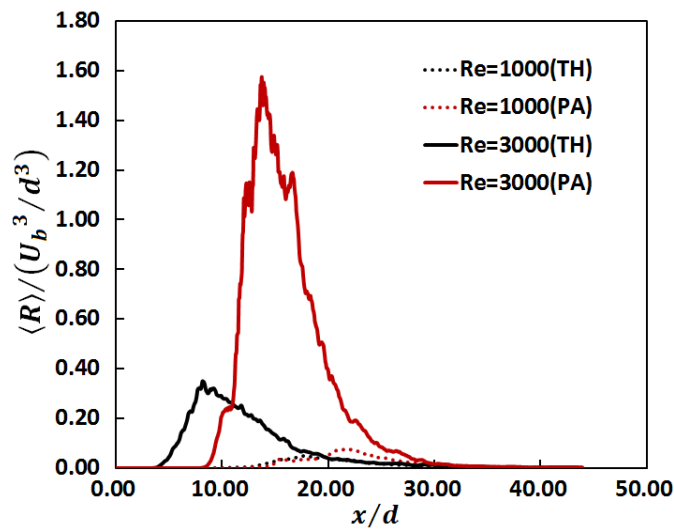


Figure 6.11 Profile of  $\langle R \rangle$  along the jet centerline

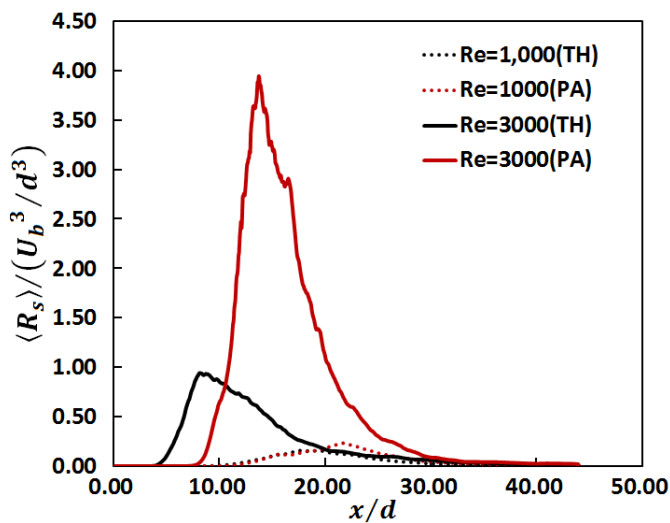


Figure 6.12 Profile of  $\langle R_s \rangle$  along the jet centerline

## 6.4 Conclusion

With the computation of the invariants of the velocity-gradient, rate-of-strain, rate-of-rotation tensors, the investigation in this chapter provides the information on the rates of vortex stretching and compression, the topology and geometry of deformation of the fluid element, and the kinetic feature of the local straining.

The results reveal that in the jet potential core, the flow possesses a strong predominance of dissipation over enstrophy and the equilibrium between vortex stretching and vortex compression. In the transition process of the plane jet, the evolution of vortex structure is faster than the evolution of the deformation of fluid elements; meanwhile the local straining is gradually enhanced. After the plane jet attains the fully-developed state, irrotational dissipation with small velocity gradient dominates, however, the vortex tubes with solid body rotation and small kinetic energy dissipation still exists with the small probability density; in addition, the characteristic teardrop shape of the  $(R, Q)$  map also forms, which implies the remarkable sheet structure and vortex stretching; the geometry of the fluid elements with the most frequent occurrence should be a geometry between biaxial stretching and axisymmetric stretching, proved by the  $(R_s, Q_s)$  map.

In addition, the large exit Re is obviously beneficial to the transition of the local topology and geometry of the plane jet to the fully-developed turbulent state.

## References

- [1] WU N., SAKAI Y., NAGATA K., ITO Y. and HAYASE T. Study on the Dynamics and Geometry of Developing Planar Jets in View of the Invariants of the Velocity Gradient Tensor[J]. Journal of Hydrodynamics, Ser. B, **2014**: Under Review.
- [2] KERR R. M. Higher-order derivative correlations and alignment of small-scale structures in isotropic numerical turbulence[J]. Journal of Fluid Mechanics, **1985**, 153: 31-58.
- [3] BALINT J. L., VUKOSLAVIĆEVIĆ P. and WALLACE J. M. A study of the vertical structure of the turbulent boundary layer[C]. Advances in Turbulence-Proceedings of the First European Turbulence Conference, Lyon, France, **1987**: 456-464.



- [4] KIM J., MOIN P. and MOSER R. Turbulence statistics in fully developed channel flow at low Reynolds number[J]. *Journal of Fluid Mechanics*, **1987**, 177: 133-166.
- [5] METCALFE R. W., ORSZAG S. A., BRACHET M. E., MENON S. and RILEY J. J. Secondary instability of a temporally growing mixing layer[J]. *Journal of Fluid Mechanics*, **1987**, 184: 207-243.
- [6] CHONG M. S., PERRY A. E. and CANTWELL B. J. A general classification of threedimensional flow fields[J]. *Physics of Fluids A: Fluid Dynamics*, **1990**, 2(5): 765-777.
- [7] BLACKBURN H. M., MANSOUR N. N. and CANTWELL B. J. Topology of fine-scale motions in turbulent channel flow[J]. *Journal of Fluid Mechanics*, **1996**, 310: 269-292.
- [8] OOI A., MARTIN J., SORIA J. and CHONG M. S. A study of the evolution and characteristics of the invariants of the velocity-gradient tensor in isotropic turbulence[J]. *Journal of Fluid Mechanics*, **1999**, 381: 141-174.
- [9] SORIA J. et al. A study of the finescale motions of incompressible timedevolving mixing layers[J]. *Physics of Fluids*, **1994**, 6(2): 871-884.
- [10] SORIA J. and CANTWELL B. J. Topological visualisation of focal structures in free shear flows[J]. *Applied Scientific Research*, **1994**, 53: 375-386.
- [11] Da SILVA C. B. and PEREIRE J. C. F. Invariants of the velocity-gradient, rate-of-strain, and rate-of-rotation tensors across the turbulent/nonturbulent interface in jets[J]. *Physics of Fluids*, **2008**, 20: 055101.
- [12] DAVIDSON P. A. *Turbulence - An introduction for scientists and engineers*[M]. New York, the USA: Oxford University Press, **2004**: 266-269.

[J]: *Journal Article*

[M]: *Monograph*

[C]: *Conference Proceeding*

## Chapter 7

### CONCLUSIONS AND FUTURE PROSPECT

In this thesis, the influence of the initial condition, including the typical Reynolds number and the mean velocity profile at the jet exit, on the spatial development of plane jets has been studied by means of the direct numerical simulation.

#### 7.1 Conclusions

The main conclusions in this thesis are:

1. The velocity and scalar fields in the plane jet is importantly dependent on the Reynolds number and the mean velocity profile at the jet exit. The relevant results show the length of the jet potential core becomes shorter and the flow transition is promoted with the increase of the exit Reynolds number; however, the larger turbulent variables are observed in the cases with the small exit  $Re$  in the flow development process. The large decay rate of mean variables and large local maxima of the turbulent variables are found in the cases with parabola profile of the exit mean velocity profile in the flow development process.

2. The transition of the plane jet from the laminar state to the turbulent state is advanced by a large Reynolds number and the parabola mean velocity profile at the jet exit.

3. The streamwise convection and the lateral turbulent transport are dominant in the transport of the mean streamwise momentum and mean scalar. In the near field region behind the potential core, the mean streamwise momentum and mean scalar transport are strengthened by a small exit  $Re$ ; meanwhile, the influence of the exit mean velocity profile on convection and turbulent transport in the mean streamwise momentum and mean scalar transport is not obvious.

4. The plane jet shows the stronger Reynolds number dependency in the

condition with a small Reynolds number; the influence of the initial condition on the plane jet is especially remarkable in the near field, but this dependency becomes weaker in the downstream region of the plane jet.

5. The cross-impact between the exit  $Re$  and the exit profile of the mean velocity cause the change in the effects of the single factor on the flow. In the cases with PA, the effect of the exit  $Re$  is amplified in the downstream region of the plane jet, and the length of the potential core is almost same in two cases with different exit  $Re$ , and in the downstream region the turbulent values of velocity and scalar with different exit  $Re$  don't converge like that with TH.

6. The coherent structure in the plane jet also shows the dependency of the exit  $Re$  and mean velocity profile. The increase of exit  $Re$  advances the occurrence and merging of the coherent structure, and induces more small-scale coherent structure in the downstream region, meanwhile, in the cases with small exit  $Re$ , the coherent structure in a larger scale can be detected; meanwhile, the scale of CSs in the cases with the parabola exit mean velocity profile is much larger than the ones with the top hat exit mean velocity profile, especially in the transition process of the plane jet.

7. In the cases with large exit Reynolds number, the evolution of the interface is also accelerated, and the topology of interface is more complicated.

8. Based on the analysis about the invariants of velocity-gradient, rate-of-strain, and rate-of-rotation tensors, the kinematics, dynamics and local structure of the plane jet in the fine-scale are studied. It is revealed that in the jet potential core, the flow possesses a strong predominance of dissipation over enstrophy and the equilibrium between vortex stretching and vortex compression. In the transition process of the plane jet, the evolution of vortex structure is faster than the evolution of the deformation of fluid elements; meanwhile the local straining is gradually enhanced. After the plane jet attains the fully-developed state, irrotational dissipation with small velocity gradient dominates, however, the vortex tubes with solid body rotation and small kinetic energy dissipation still exists with the small probability density; the geometry of the fluid elements with the most frequent occurrence should be the geometry between biaxial stretching and axisymmetric stretching.

9. The transition of the local topology and geometry of the plane jet is dependent on the exit Reynolds number, which achieves the fully-developed turbulent

state faster with the large exit Reynolds number.

## 7.2 Future Prospect

The present findings illustrate the characteristics of the plane jets with different moderate Reynolds number and two kinds of exit mean velocity profiles, in which the information about the features of the velocity and scalar fields such as the decay of mean variables, the turbulent intensity, and momentum and scalar transport will be quite useful in the engineering applications, e.g. combustion, propulsion and environmental; meanwhile the results about the flow structure will help us to understand the physical phenomena related to the plane jet. In the future, based on these findings in present numerical study, the further study needs to be combined with some engineering aims.

Currently it is unpractical to simulate the turbulence with a quite high Reynolds number properly. I think some experimental work will be needed to complete the topic for the future work. In addition, based on both the numerical simulation and the experiments, the effect of the initial intensity and profile of the turbulence at the jet exit on the development of the plane jet deserves careful investigation in the future.